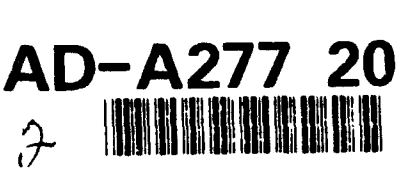

Year 1 Annual Report: 1 January 1993 - 31 December 1993

Correlations Between Micromagnetic, Microstructural and Microchemical Properties in Ultrathin Epitaxial Magnetic Structures

M.R. Scheinfein[a,b], J.S. Drucker[b] and G.G. Hembree[a]
[a]Department of Physics and Astronomy
[b]Center for Solid State Science
Arizona State University
Tempe, AZ 85287-1504

A Proposal Supported By The Office Of Naval Research
(N00014-93-1-0099)
Project Director
Dr. Richard G. Brandt
Physics Division

Technical Representative: Michael R. Scheinfein
(602) 965-9658 Phone
(602) 965-7954 FAX
shine@shine.la.asu.edu e-mail
scheinfein@phyast.la.asu.edu e-mail

Signatures:

Michael R. Scheinfein
Department of Physics and Astronomy
_____ Date: 12-17-93

Teresa Demonte
Sponsored Projects
Teresa Damonte Date: 12 17 93

DISCLAIMER NOTICE

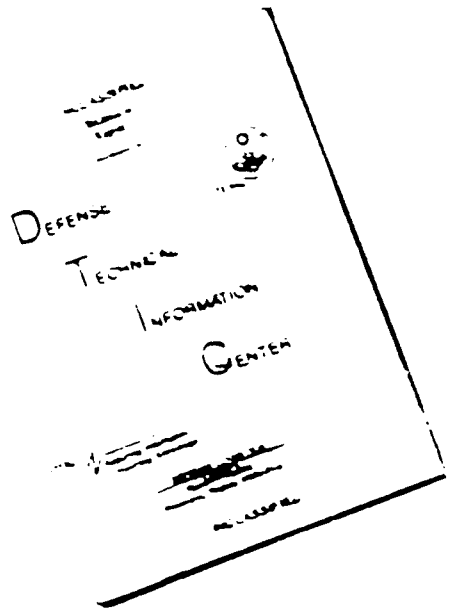

THIS DOCUMENT IS BEST QUALITY AVAILABLE. THE COPY FURNISHED TO DTIC CONTAINED A SIGNIFICANT NUMBER OF PAGES WHICH DO NOT REPRODUCE LEGIBLY.

Contents

0.0	Contents	.....	2
1.0	Introduction	.....	3
2.0	Instrumentation	.....	3
3.0	fcc Fe/Cu(100)	.....	7
4.0	bcc Fe/Ag(100)	.....	23
5.0	$Fe/CaF_2/Si(111)$	.....	23
6.0	Research Plans : Year 2	.....	31
7.0	Appendix A: Associated Staff	.....	31
8.0	Appendix B: Publications	.....	32

1.0 Introduction:

The proposed goal of this project is to obtain quantitative measurements of the microstructural, microchemical and micromagnetic properties of surfaces and interfaces of ultrathin films composed of magnetic materials deposited on non-magnetic, antiferromagnetic (metal) and insulating substrates. Surface microanalytic methods based on a unique ultrahigh-vacuum scanning transmission electron microscope/scanning electron microscope (UHV-STEM/SEM) equipped with in-situ thin film preparation and characterization tools are being used. Magnetic characterization is performed in-situ using the surface magneto-optical Kerr effect (SMOKE). Additional magnetic microstructure measurements are being conducted in a novel STEM based electron holography system where absolutely calibrated nanometer resolution magnetometry is possible. Of the proposed systems for study oulined in the original proposal, work has begun on Fe/Ag, Fe/Cu, Fe/CaF_2 and Fe/CaF_2/Si (half of the proposed systems). The measurements are designed to clarify the relationship between observed real-space micro-structure of interfaces, ultrathin magnetic films and superlattices with magnetic properties, such as surface anisotropy. The dependence of magnetic properties on film morphology, which may be a function of the deposition parameters during the initial stages of growth, and on structural properties such as strain and interface roughness is being studied. We are exploring the electron beam modification of CaF_2, both as an electron beam resist and as a damagable material for preferential nucleation, as a means of defining one and two dimensional nanometer sized epitaxial magnetic devices. Here, we report on our progress in year 1 of this 3 year project.

2.0 Instrumentation

In the first year of this project, we have successfully outfitted our UHV-STEM with the required metal cleaning, characterization and deposition equipment for the preparation and analysis of ultrathin ferromagnetic films [See Correlations Between Ultrathin Film Microstructure and Magnetic Properties for Room Temperature Epitaxial Films of fcc Fe/Cu(100) by K. R. Heim, S. D. Healy, Z. J. Yang, J. S. Drucker, G. G. Hembree, and M. R. Scheinfein in the Appendix]. Shown in Fig. 1 is a schematic of our system. The preparation chamber of the microscope now includes Ar ion beam sputtering, a coaxial cylindrical mirror analyzer, and a Ce^{2+}:YAG scintillator for RHEED. Currently, one Fe electron beam evaporator is resident on the instrument. A second (Co) electron beam evaporator has been constructed and is to be calibrated.

We have developed a unique implementation of the three-axis surface magneto-optic Kerr Effect (SMOKE) for measuring surface magnetization [See Combined Three-Axis Surface Magneto-Optical Kerr Effects in the Study of Surface and Ultrathin-Film Magnetism, by Z.J.

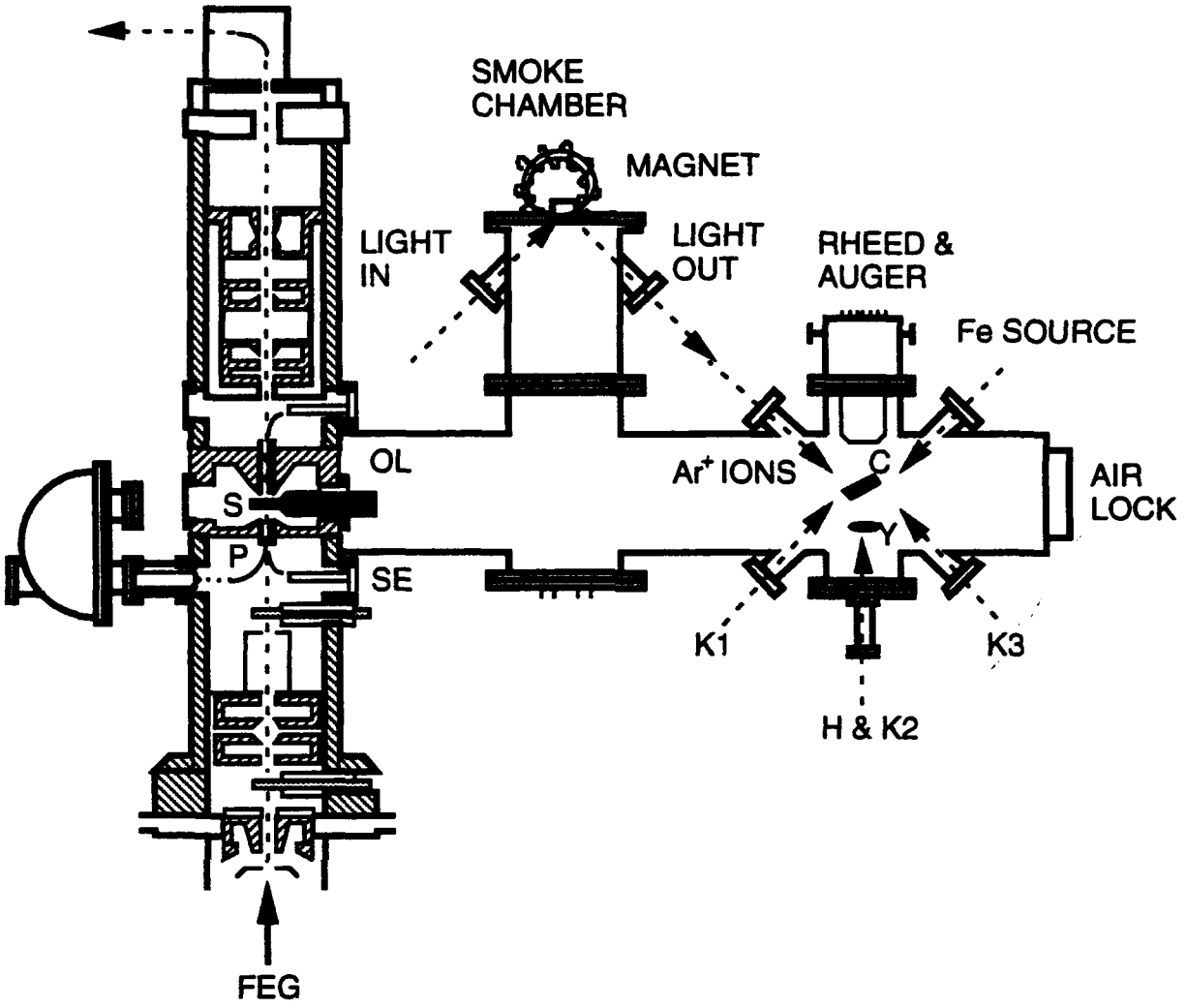

Figure 1: Modified VG HB501-S thin film growth and characterization facility. The salient features of the microscope column include; P, the lower parallelizer, SE the lower secondary electron detector, S-sample, OL-objective lens, and a FEG-field emission gun. The specimen preparation chamber consists of a SMOKE chamber for surface magnetism analysis, a CMA-cylindrical mirror analyzer for AES and RHEED, and sample surface preparation tools such as an Ar^+ ion sputtering gun, an Fe evaporator, annealing stages and Knudsen cell evaporators K1, K2, and K3. Also shown are the Cu crystal, C, the YAG crystal, Y, and the air lock for fast sample entry.

Yang and M.R. Scheinfein in the Appendix]. Our measurement scheme for SMOKE, shown in Fig. 2 is typical in that the system includes a polarized He-Ne intensity-stabilized laser (l=632.8nm, $\Delta I/I_0$=0.1%), two Glan-Thompson polarizers (field of view ~30°, resolution ~0°5'), a fused-silica head photo-elastic modulator (f=50KHz, 170 nm to 2600 nm transmission) with anti-reflective coatings optimized for He-Ne light, and a photodiode detector. In analyzing experiments employing polar, longitudinal and transverse Kerr effects, the direction of the applied magnetic field must be distinguished from the direction of magnetization during the switching process. Since the Kerr effect exists for any arbitrary direction of the

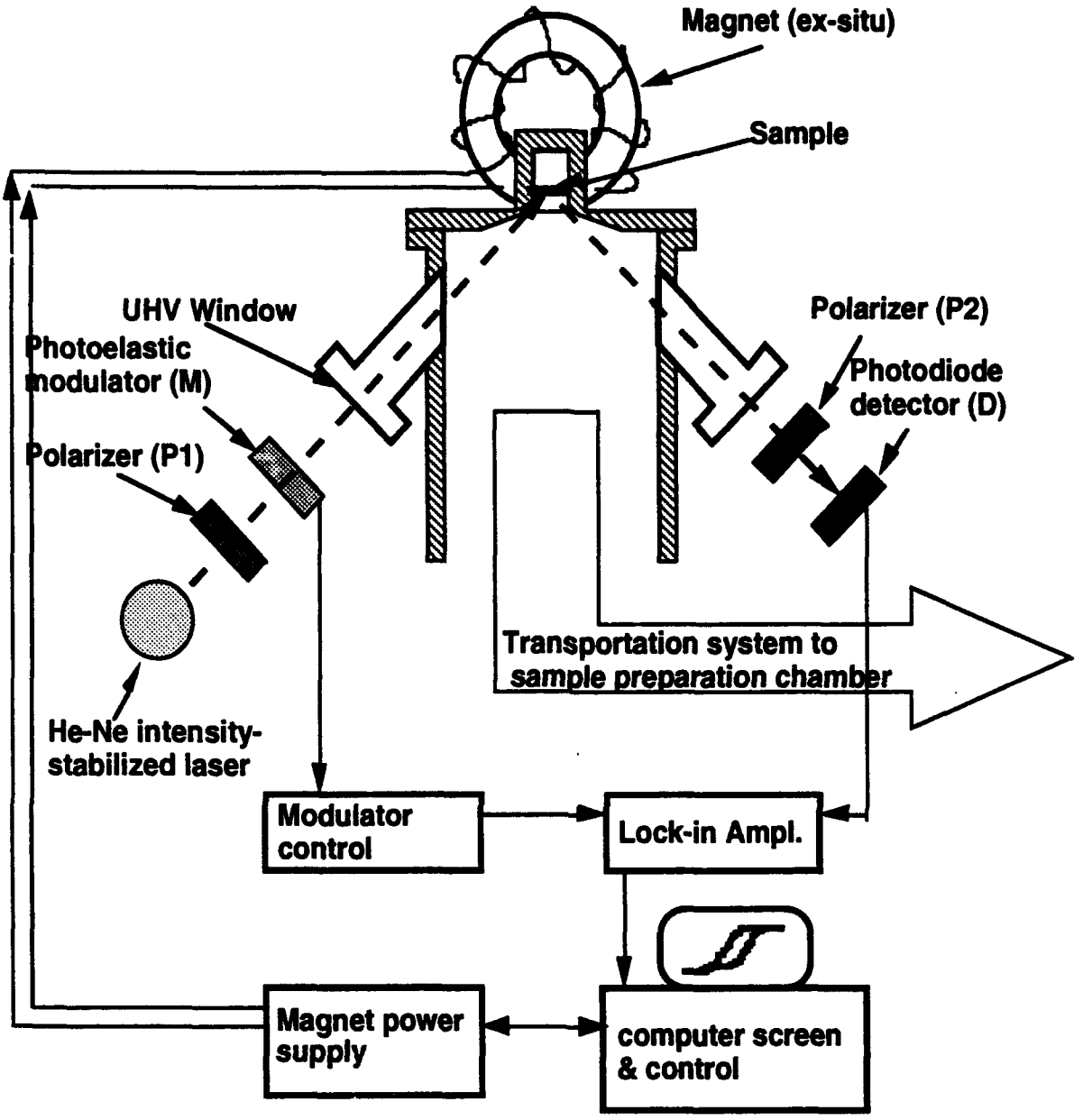

THE SURFACE MAGNETO-OPTIC KERR EFFECT (SMOKE) CHAMBER

Figure 2: A schematic depiction of our implementation of the three-axis surface magneto-optic Kerr effect .

magnetization (relative to the scattering plane), for non-normal incidence, magnetization loops obtained from any of the three Kerr effects may contribute to the detected signal. Here, we distinguish a pure Kerr effect from the general Kerr effect by analyzing the sensitivity of the detected signals to various magnetization components in the sample to be analyzed. A pure Kerr effect experiment may, for example, employ normally incident polarized light, and normally

applied magnetic fields to detect only the perpendicular component of the magnetization; the pure polar Kerr effect. However, at non-normal incidence with different relative orientations of the three basic optical devices (polarizer, modulator, and analyzer) in the SMOKE system, we showed that either all three magnetization components or any one of them can be detected. Thin-film anisotropies and switching modes can be studied by comparing these three combined Kerr-effect magnetization loops. We derived the normalized light intensity sensed by a photodiode detector from the three combined Kerr effects, both in the ultrathin-film limit and from a bulk surface, at general oblique incidence, and with different orientations of the polarizer, modulator, and analyzer These expressions are shown to reduce to the simple case where no longitudinal Kerr effect is detected at normal incidence. In this case, the detectivity of the polar Kerr effect reaches a maximum.

In addition to the instrumentation which was specified in the original proposal, we have implemented an off-axis STEM holography technique [See Absolute Magnetometry at nm Transverse Spatial Resolution: STEM Holography of Thin Cobalt Films by Marian Mankos, M. R. Scheinfein and J. M. Cowley in the Appendix]. We use an electron biprism, a conductive wire about 0.5μm in diameter held at a constant potential, placed in the illuminating system of a STEM (VG Instruments HB 5). The wave emitted from the electron source is split by the biprism into two wave packets resulting in the formation of two identical coherent electron probes at the specimen. If the objective lens is operated at a large defocus, a hologram, the interference between the two coherent waves, appears as a fringe-modulated image in the detector plane. The wave vectors and hence the fringe spacing are determined by the electron beam voltage and the voltage applied to the biprism wire. With a defocused objective lens, a large area of the specimen is illuminated and the beam is held stationary (no scanning). The hologram is recorded on a slow-scan CCD camera and reconstructed in the conventional way . A fast Fourier transform of the hologram yields a diffractogram. The diffractogram has two sidebands whose separation is dependent upon the spacing of the fringes. This side-band separation in off-axis holography allows the removal of the conjugate image present in the hologram. One sideband is isolated and its inverse Fourier transform reveals the amplitude and the phase of the complex image wave. Magnetic thin films are strong phase objects with phase differences of $\geq 10\pi$ rad common, therefore we analyze only the reconstructed phase image. The contrast in a STEM electron hologram can be explained by analyzing the wave paths from the source through the specimen to the detector plane. A single wave emerges from the electron source and is split by the biprism, forming two coherent virtual sources. There are two different modes of STEM holography, an absolute mode and a differential mode. In the absolute mode, one wave packet passes through vacuum and the other passes through the specimen. This mode has analogy with TEM electron holography and the derivative of the phase is recovered. In the differential mode,

both waves traverse the specimen and interfere in the detector plane and the absolute phase is recovered. Since the electron beam energy and biprism potentials are absolutely calibrated, the interference pattern in the electron hologram is absolutely calibrated. We are therefor able to make direct measurements of thickness integrated magnetization with better than 2 nm transverse spatial resolution.

We have inherited a dual source electron beam evaporation system from Prof. Mary Beth Stearns who is retiring. We have made minimal capital investments in this instrument to bring it into reliable operation. Experiments using this evaporation system designed to explore the spatial component in giant magnetoresistance systems will be outlined in section 6.0.

Our surface science group has recently acquired a Low Energy Electron Microscope (LEEM) from the Division of Materials Research at the National Science Foundation. Both M. Scheinfein and G. Hembree are co principal investigators on this grant and hence have access to this instrument. We have experiements planned for early winter for the investigation of the nucleation and growth of fcc Fe/Cu(100).

G. Hembree has designed and constructed a high resolution Auger electron spectroscopy and RHEED chamber which is being used to develop diffraction enhanced Auger electron spectroscopy. By using the surface wave resonance in RHEED, enhanced surface selectivity is possible for the analysis of both chemical and crystallographic surface structure. Initial experiments have been undertaken in the Ge/Si(100) system. We plan on using this method to study the nucleation and growth of fcc Fe/Cu(100) as well. Construction of a new high precision double axis tilt hot stage has been initiated on other funds.

3.0 fcc Fe/Cu(100)

Single crystal Cu(100) substrates were machined into 1 mm thick, 3 mm diameter shouldered disks and commercially electropolished. The Cu specimens were sputtered with 600 eV Ar^+ ions at 45° from the surface normal. Following this, the Cu was annealed at ~600°C for 15 minutes to produce a well-ordered surface, as observed with RHEED. The crystal was allowed to cool for 1.5-2.0 hours after the last anneal such that a temperature below 40°C was obtained prior to Fe deposition.

Following the surface preparation and Fe deposition, surface structural characterization was performed using secondary electron (SE) microscopy. SE microscopy contrast is sensitive to topography and local changes in the work function. Several of the cleaned Cu surfaces observed with SE microscopy revealed small contaminant clusters which we believe to be Cu_2O (based upon the most likely copper oxide formed at these temperatures and pressures) islands nucleated over the entire Cu surface. Analysis of these SE images indicates that oxygen coverages $\leq$0.0011 at.% are well below the sensitivity of the broad-beam AES (typically

sensitive to no better than 1 at.%) used in the preparation chamber. In Figs. 3a-f we display corresponding broad-beam Auger spectra and SE images for two identically prepared Cu surfaces. Figs. 3a and 3b are the respective EN(E) and dN(E)/dE spectra acquired for a clean Cu(100) surface. These spectra clearly exhibit five Cu Auger peaks (58, 105, 776, 840, and 920 eV in the derivative mode) while not detecting the O (503 eV) peak (the sensitivity factors at 3 keV indicate that O is about two times more detectable than the 920 eV Cu signal, from which we conclude that the oxygen coverage is ≤2 at.%). The SE image shown in Fig. 3e represents a typical area of the clean Cu(100) crystal surface with less than 1.4×10^9 oxide particles/cm^2, thus yielding an oxygen coverage of 0.016 at.%. The typical terrace width on these Cu(100) surfaces vary from 25 nm to 75 nm, which, based on the uniform growth, is greater than the Fe atom diffusion length for this system. Thus, the effects of a rough and disordered surface on the magnetic properties have been reduced below a detectable level. Insulators and oxides, in general, have higher secondary electron yields than metals, and hence appear bright in SE micrographs. In contrast, the Auger spectra in Figs. 3c and 3d also imply a clean Cu surface, but the SE image of Fig. 3f shows larger, more numerous (3.6×10^{10} particles/cm^2 of 10 nm average radius and 3.75 at.%) oxide particles populating the entire Cu surface. In situ electron microscopy, with its high sensitivity for the detection of surface contamination, was used to guarantee the real space chemical and structural integrity of all Cu(100) substrates prior to Fe deposition. In particular, our cleanest Cu(100) surfaces had 1×10^9 particles/cm^2 of 3 nm average radius oxide clusters, implying an oxygen coverage of order ≤0.01 at.%, which is well below the detectivity of standard surface science techniques.

The thickness dependence of SMOKE hysteresis loops of as-grown fcc Fe/Cu(100) films are shown in Fig. 4. Initial magnetic response is observed as a zero-remanence, linear hysteresis loop in the polar direction, Figs. 4a and 4b. At intermediate thicknesses, 3.5 ML, remanent polar, Fig. 4c, and longitudinal, Fig. 4d, SMOKE loops are observed. While the in-plane loop is square, the tilted polar loop displays the effects of shape anisotropy indicating a canted out-of-plane easy-axis. SMOKE loops from thicker films, 4.7 ML, Figs. 4e and 4f, lose polar remanence, but have square in-plane loops characteristic of an in-plane easy-axis. The as-grown in-plane remanence increases nearly linearly for thickness above 2 ML and below 5 ML. Thicker films (t -> 10 ML) become non-magnetic at room temperature. Films thinner than 10 ML had fcc structure with the transverse lattice constant of the substrate.

One of the unexpected research highlights achieved in Year 1 of this porject was the identification of a field induced, reversible, metastable transition for magnetization measured perpendicular (polar) to the film plane [See Field Induced Metastable States in Ultrathin Films of fcc Fe/Cu(100) by G.G. Hembree, Jeff Drucker, S.D. Healy, K.R. Heim, Z.J. Yang, M.R. Scheinfein in the Appendix]. Room-temperature grown, fcc Fe/Cu(100) films in the 2.5-3.5 ML

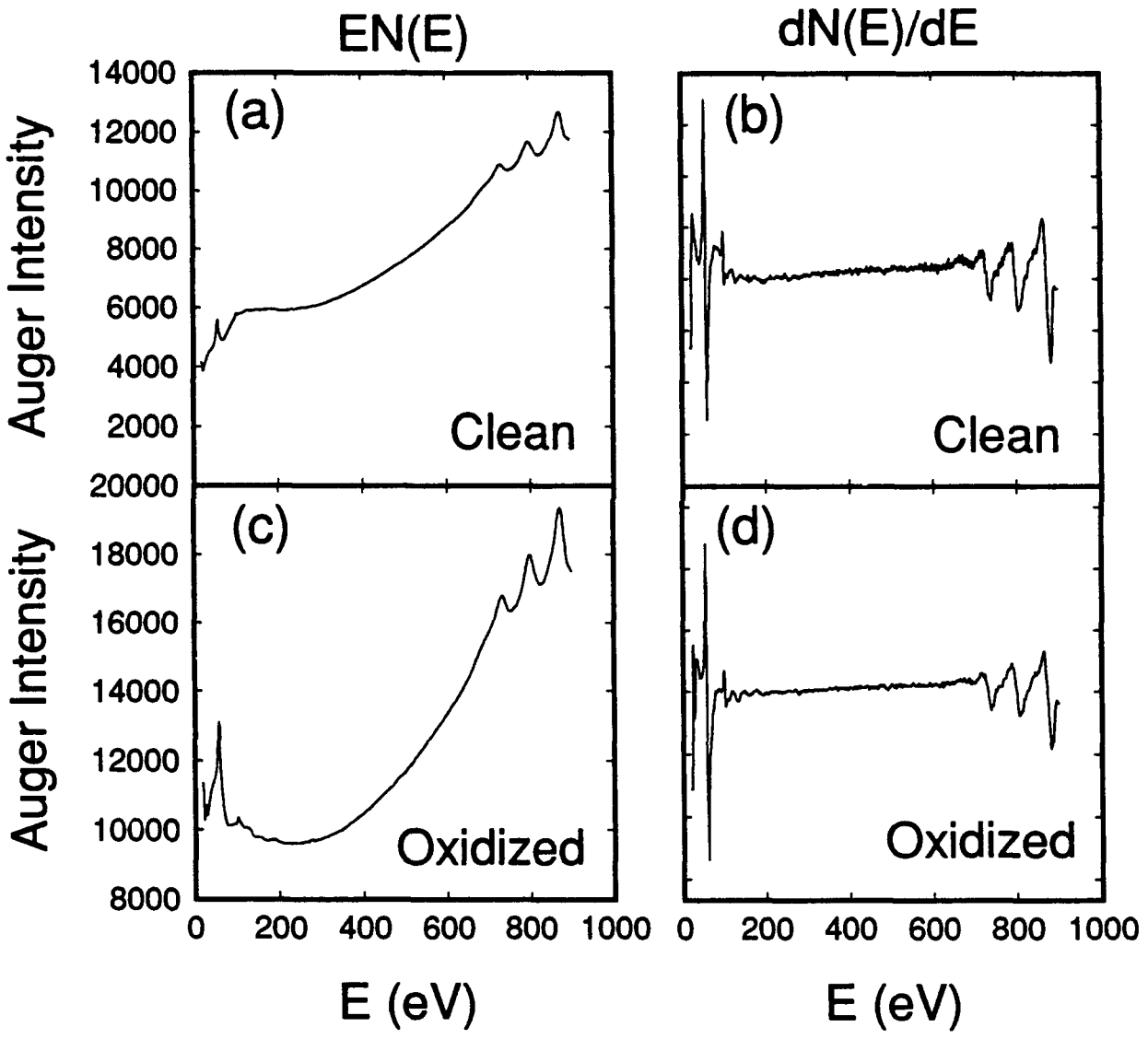

Figure 3: Auger electron spectroscopy (AES) scans of clean copper in the (a) EN(E) and (b) dN(E)/dE mode. AES scans of oxidized copper in (c) EN(E).and (d) dN(E)/dE mode.

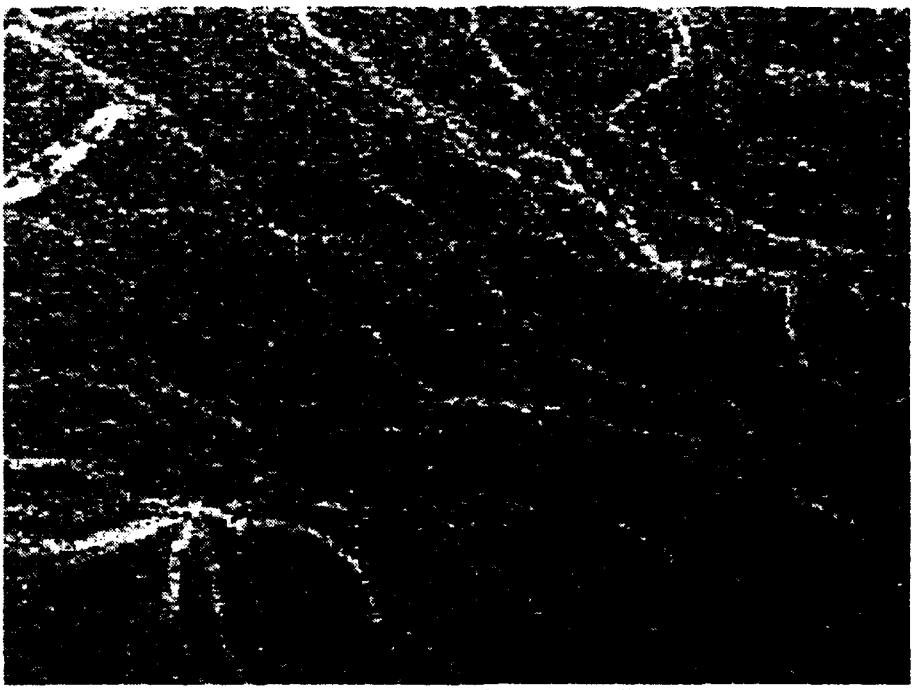

Figure 3e: Secondary electron image of the surface of Cu(100) corresponding to Auger spectra in 3(a) and 3(b). Full scale (horizontal) is 1.2μm.

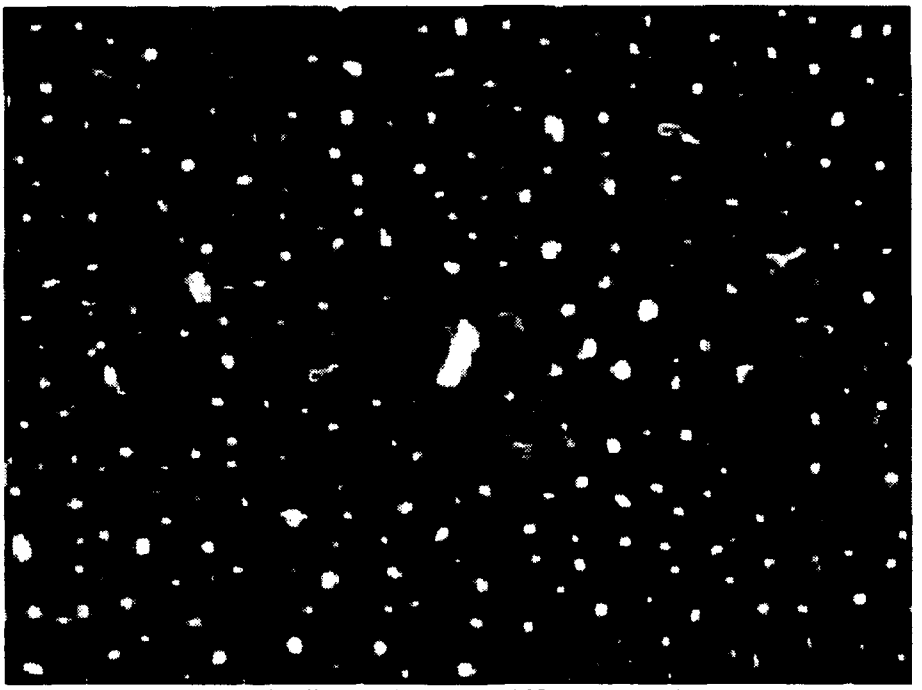

Figure 3f: Secondary electron image of the dirty surface of Cu(100) corresponding to Auger spectra in 3(c) and 3(d). Full scale (horizontal) is 1.2μm.

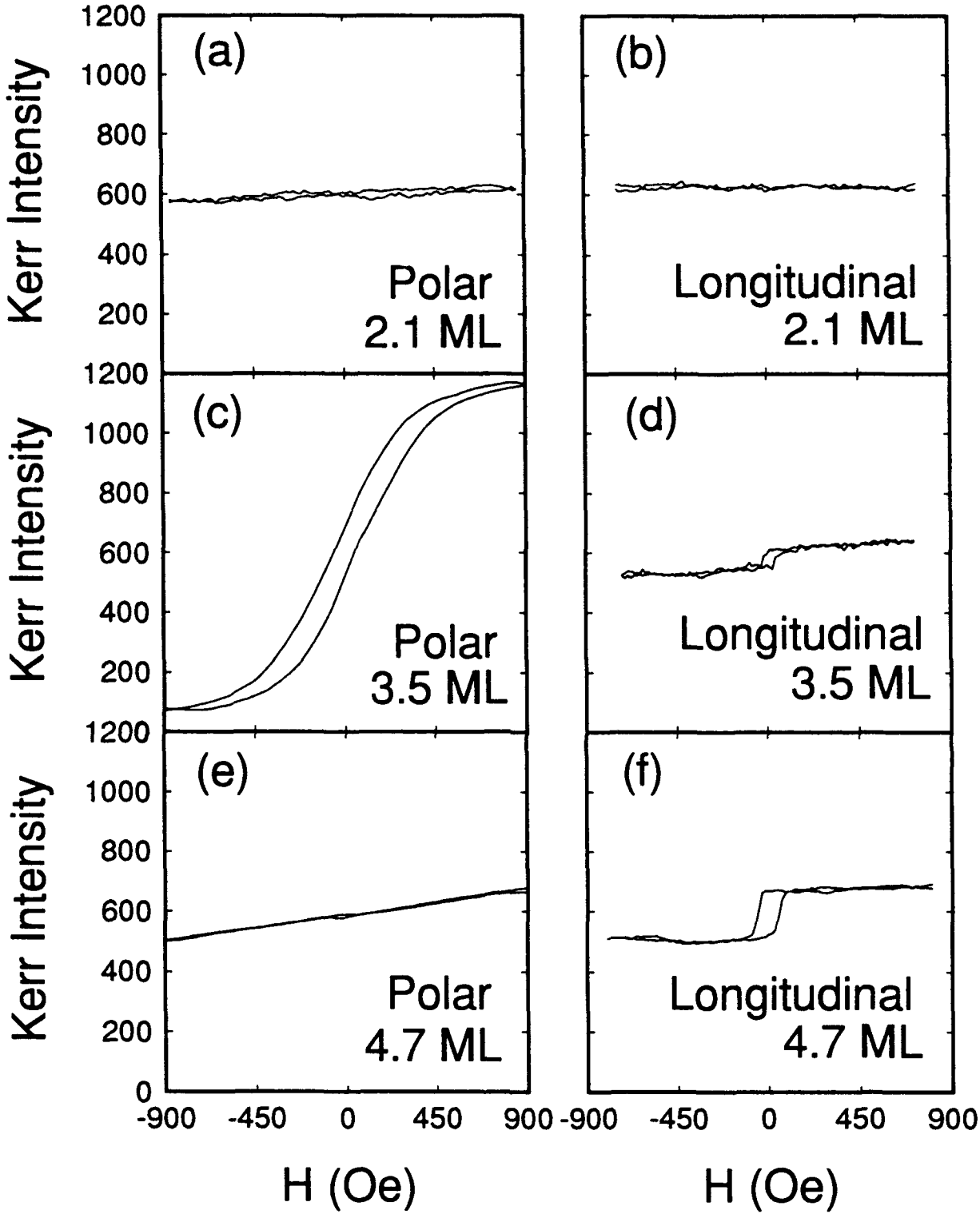

Figure 4: Room temperature grown fcc Fe/Cu(100) polar and longitudinal surface magneto-optical Kerr effect (SMOKE) hysteresis loops. The incident angle is 45^{o} for both longitudinal and polar SMOKE measurements which were made at room temperature.

regime possess both in-plane and perpendicular remanence. After application of a 9.0 kOe polar field, the out-of-plane remanence is lost. This magnetic state is stable until the film is either heated or subjected to a large in-plane magnetic field. In Figs. 5a-d, longitudinal and polar SMOKE loops of as-grown films are contrasted with the post-observation (9.0 kOe polar field) polar and longitudinal SMOKE loops. After exposure to the field, there was no polar remanence. The in-plane loop remains square, with a small change in the coercivity, indicating an increase of the in-plane anisotropy constant. This state is stable until heating or application of a 1.5 kOe in-plane magnetic field. The reversibility of the transition is demonstrated in Figs. 5e-f. The metastable magnetic state induced by the 9.0 kOe field evolves after a small temperature increase ($T = 40^{o}C$) as shown in Fig. 5e. After the application of an in-plane magnetic field (H=1.5 kOe), Fig. 5f, the initial state is nearly restored. It is difficult to explain our field-induced transformation in the context of two-dimensional fluctuations since large out-of-plane fields should enhance the in-plane to out-of-plane transition at temperatures below the critical transition temperature and large in-plane fields should stabilize the in-plane component of the magnetization. Total energy calculations indicate that a small decrease in the lattice constant can stabilize a lower energy non-magnetic fcc Fe phase. While a field induced change in the anisotropy can explain the observed transition, the lack of perpendicular remanence in the metastable state could result from a local magnetic disordering of the film in the direction perpendicular to the surface as a result of magneto-elastic strains (compression) induced by the 9.0 kOe magnetic field, stabilized by the presence of a lower energy, non-magnetic state. In this state, in-plane ferromagnetism may be preserved. Heating slightly expands the lattice, and locally reactivates the film. The application of large in-plane magnetic fields may compress the Fe film in-plane, with subsequent out-of-plane expansion, restoring the original state; a hypothesis which could be tested by performing in-field EXAFS measurements. The in-plane lattice in Fe is stabilized by the Cu(100) template, and the original response is recovered.

We analyzied film growth at low film coverages and found that supersurface island formation can be observed locally by correlating the SE images with the Cu and Fe AE images [See The Initial Phases of Epitaxy of fcc Fe/Cu(100): Supersurface and Subsurface Island Formation by S.D. Healy, K.R. Heim, Z.J. Yang, G.G. Hembree,J. S. Drucker, M. R. Scheinfein and Structural And Magnetic Properties Of Epitaxially Grown fcc Fe/Cu(100) and Fe/CaF_2/Si(111) by M.R. Scheinfein, S.D. Healy, K.R. Heim, Z.J. Yang, J.S. Drucker, G.G. Hembree in the Appendix]. One such set of spatially correlated images is displayed in Fig. 6 for a 0.33 ML thick Fe film. The SE image in Fig. 6a illustrates supersurface Fe islands with the corresponding contour plot shown in Fig. 6b. The large island (~45 nm in diameter) has intensity contours near its upper left quadrant indicating that this island is composed of more than one monolayer of Fe within the bulk of the island. The contrast of the smaller islands is

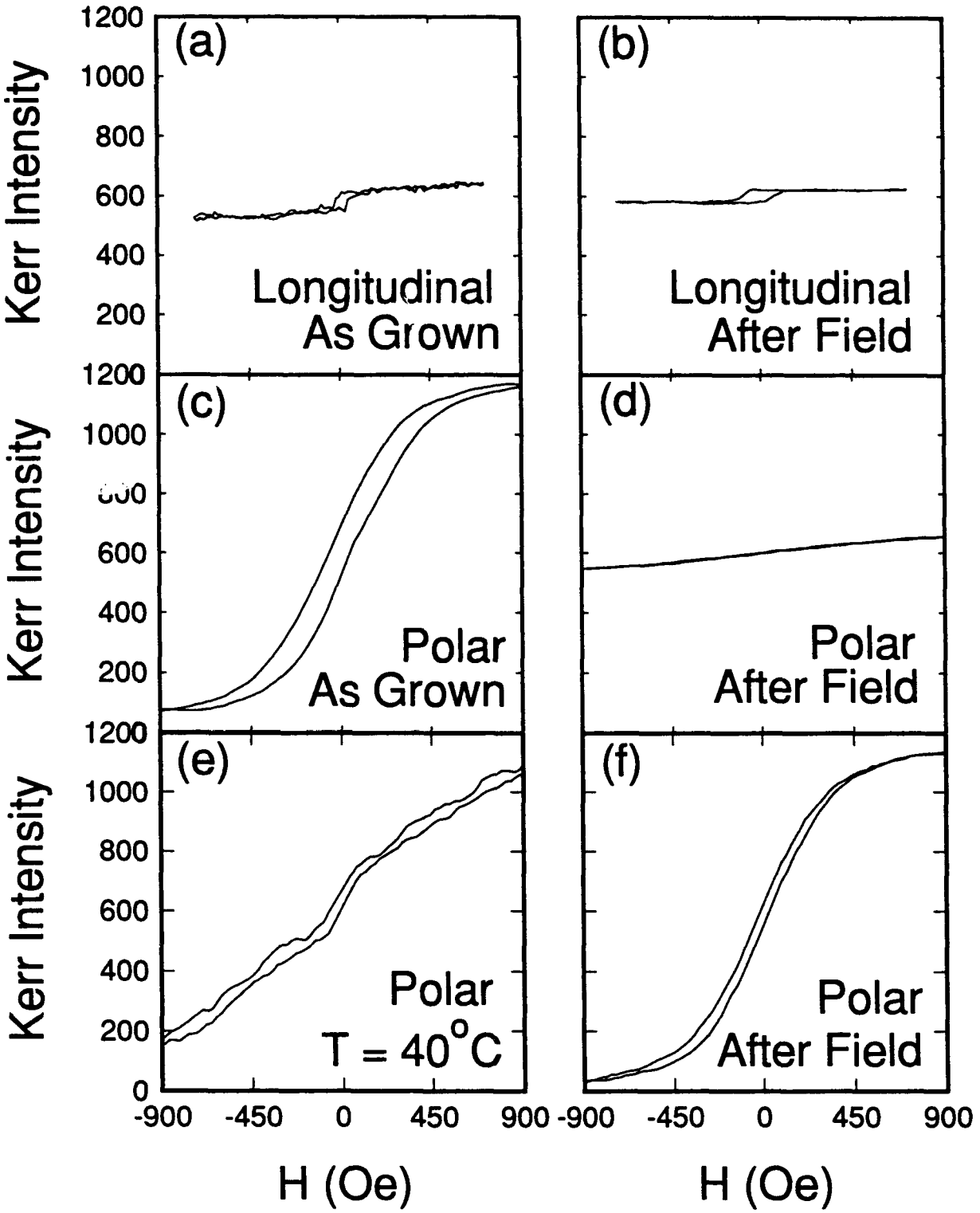

Figure 5: Room temperature grown 3.5 ML fcc Fe/Cu(100) polar and longitudinal SMOKE hysteresis loops. As grown, (a) longitudinal and (c) polar loops. After applying 9.0 kOe polar field, (b) longitudinal and (d) polar loops. (e) Polar loop after heating to 40 C, and (f) after applying a 1.5 kOe longitudinal field. All loops are on the same calibrated scale.

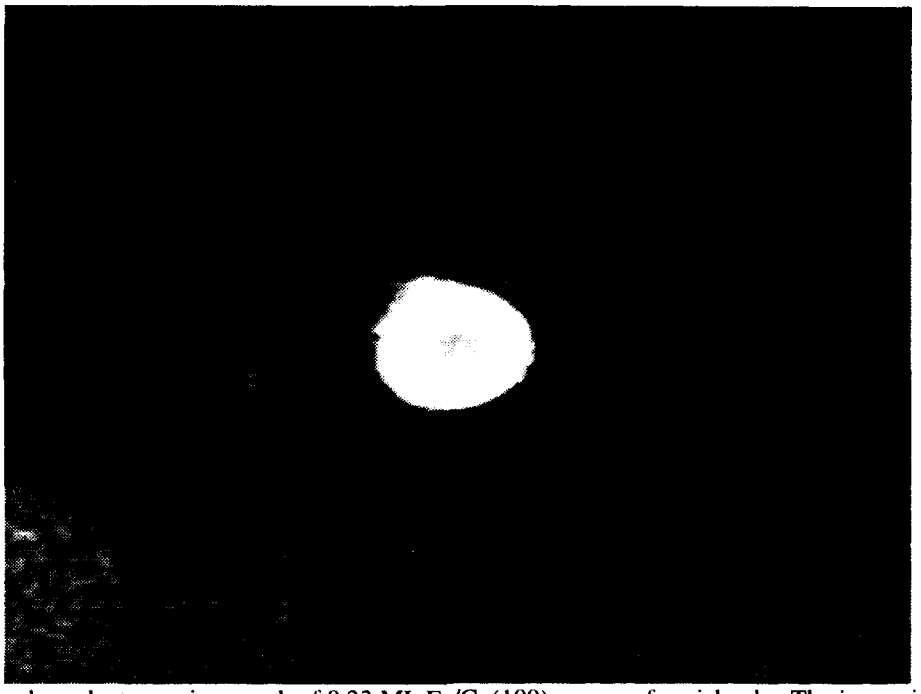

Figure 6a : Secondary electron micrograph of 0.33 ML Fe/Cu(100) supersurface islands. The image is 150 nm full scale (horizontal).

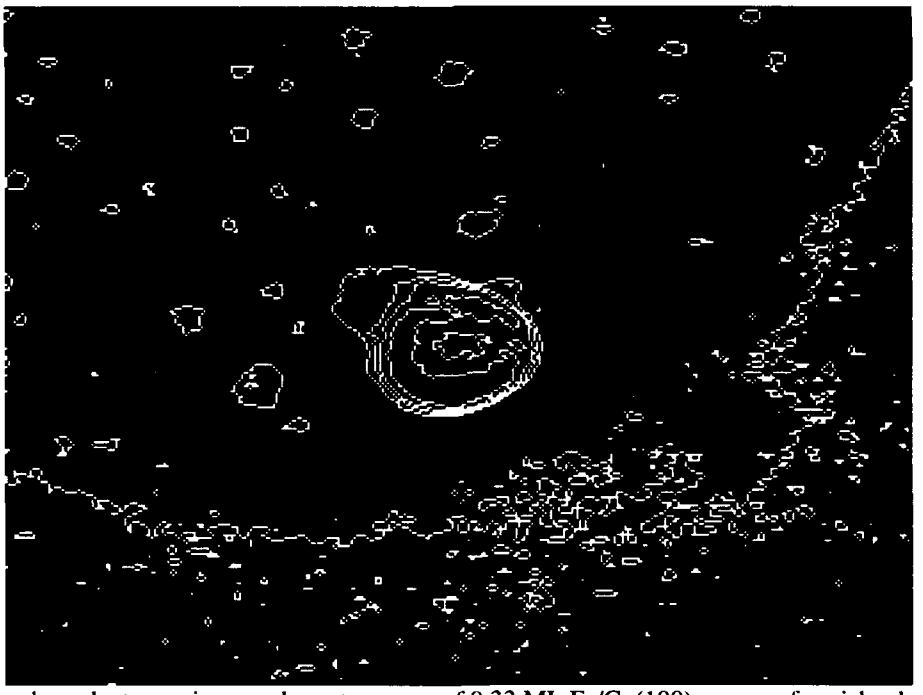

Figure 6b : Secondary electron micrograph contour map of 0.33 ML Fe/Cu(100) supersurface islands. The image is 150 nm full scale (horizontal) and is extracted from 6a..

Figure 6c : Cu Auger electron micrograph of 0.33 ML Fe/Cu(100) supersurface islands. The image is 150 nm full scale (horizontal) and is from the identical region as 6a..

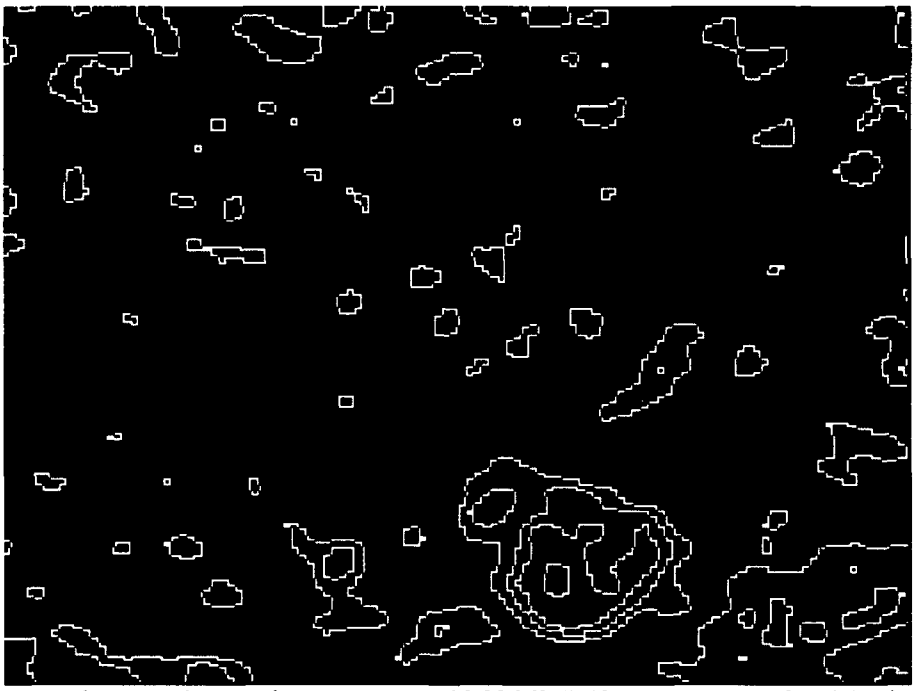

Figure 6d : Cu Auger electron micrograph contour map of 0.33 ML Fe/Cu(100) supersurface islands. The image is 150 nm full scale (horizontal) and is from the image in 6c..

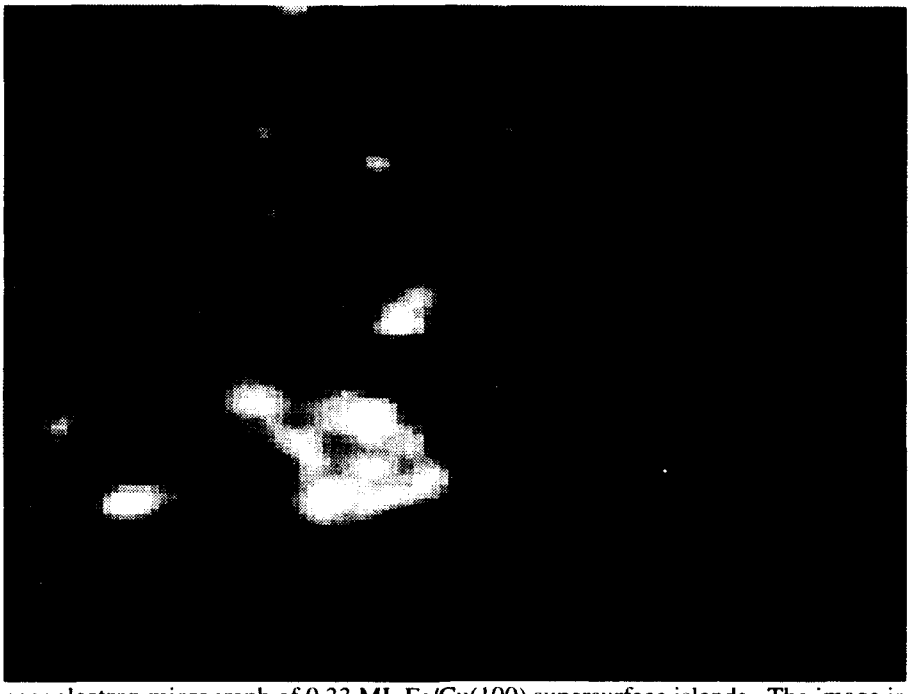

Figure 6e: Fe Auger electron micrograph of 0.33 ML Fe/Cu(100) supersurface islands. The image is 150 nm full scale (horizontal) and is from the identical region as 6a..

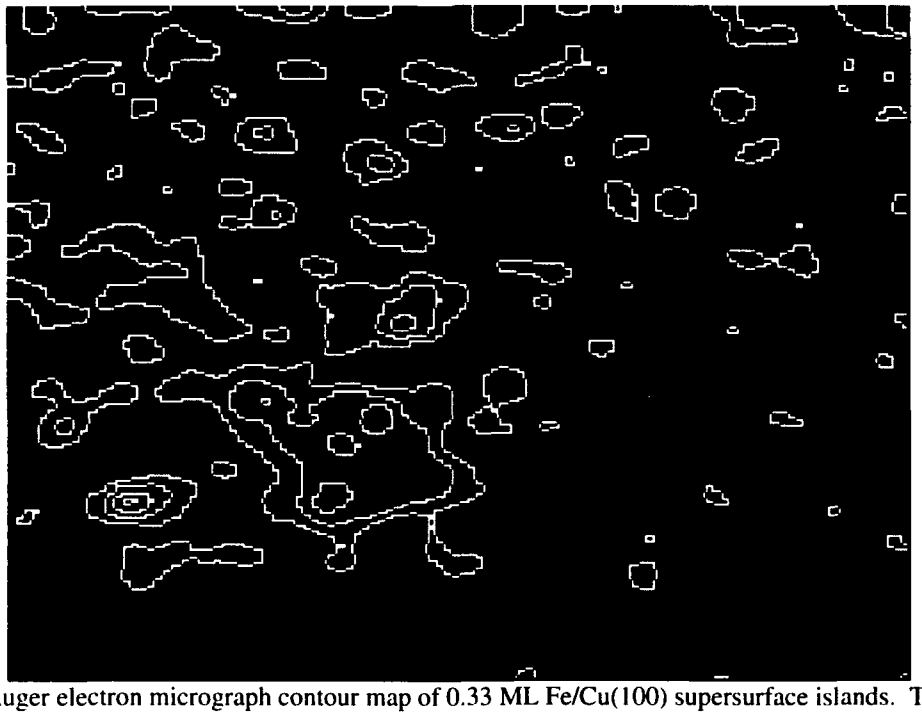

Figure 6f: Fe Auger electron micrograph contour map of 0.33 ML Fe/Cu(100) supersurface islands. The image is 150 nm full scale (horizontal) and is from the image in 6e.

identical to the contrast of the tip of the larger island (within the signal-to-noise limits of these measurements) indicating identical Fe island thicknesses. AE images and contour maps derived from the Cu (Figs. 6c and 6d) and Fe (Figs. 6e and 6f) Auger electron signals can be directly correlated with the SE image of the Fe islands. The black areas in Fig. 6c indicate the lack of a Cu signal, while the white areas in Fig. 6e indicate the presence of Fe. It is evident by correlating the contrast in the images and contour maps that the large island and several smaller islands are composed of Fe. Since the signal-to-noise ratio is much better in the SE image, the island density pictured in Fig. 6a likely characterizes the surface.

Fig. 7a-c displays SE, Cu AE and Fe AE images respectively, all in registry for a Cu substrate with 1.7 ML of Fe deposited at room temperature. The bright regions in the SE image are not correlated with any structure in the Cu (Fig. 7b) or Fe (Fig. 7c) AE images. However, these same Cu and Fe AE images indicate that the regions depleted of Cu are rich in Fe. Since there is no contrast in the SE image, and the SE yield for fcc Fe and Cu are practically identical, we conclude that there is no topographic structure on the surface in this region, indicating that the contrast observed in the AE images is a result of two-dimensional subsurface island formation. We have also observed both types of island growth as well as layer-by-layer growth in the same film at different positions along the film. This indicates that these phenomena are controlled by locally varying template surface conditions. Our observations suggest that in the regions where subsurface islands occur, a vertical Fe-Cu atomic site exchange occurs. This process continues until the driving force causing the exchange diminishes. We observed this Fe coverage to be thicker than 2 ML, beyond which continuous Fe films grew. The lack of ferromagnetic ordering observed in this sub-2 ML regime is not inconsistent with the observed growth process.

We explored the role of contamination on the nucleation, growth and magnetic properties of a 3.1 ML Fe film grown on a Cu(100) crystal. The mean contaminant cluster separation was approximately 54 nm (2.2×10^{10} particles/cm^2 of 4 nm average radius and 1.1% total areal coverage). This contamination did not appear to affect the Fe film morphology at locations away from the contaminants. This observed morphology invariance is a result of the diffusion lengths of metals on metals being much less than the mean contaminant cluster separation. The associated Kerr loops show polar remanence and the lack of longitudinal remanence just as for uncontaminated films in the regime near the onset of ferromagnetism ($2.3<\Theta<3.5$ ML). Although we did not observe any differences in magnetic properties between clean or slightly contaminated Cu substrates with a ~3 ML Fe deposition, the results are expected to be dramatic for other contaminants of different concentrations. Compound formation between oxygen or copper oxide and Fe comprises many phases. Compounds with non-magnetic, antiferromagnetic, or ferromagnetic phases would undoubtedly alter the observed magnetic

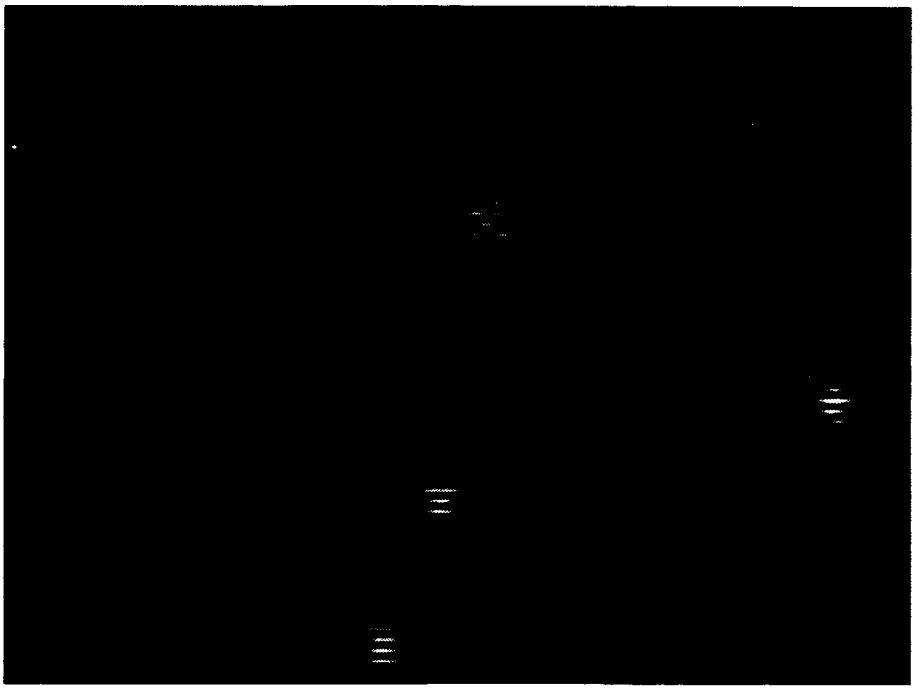

Figure 7a: Secondary electron micrograph of 1.7 ML Fe/Cu(100) subsurface islands. The image is 150 nm full scale (horizontal).

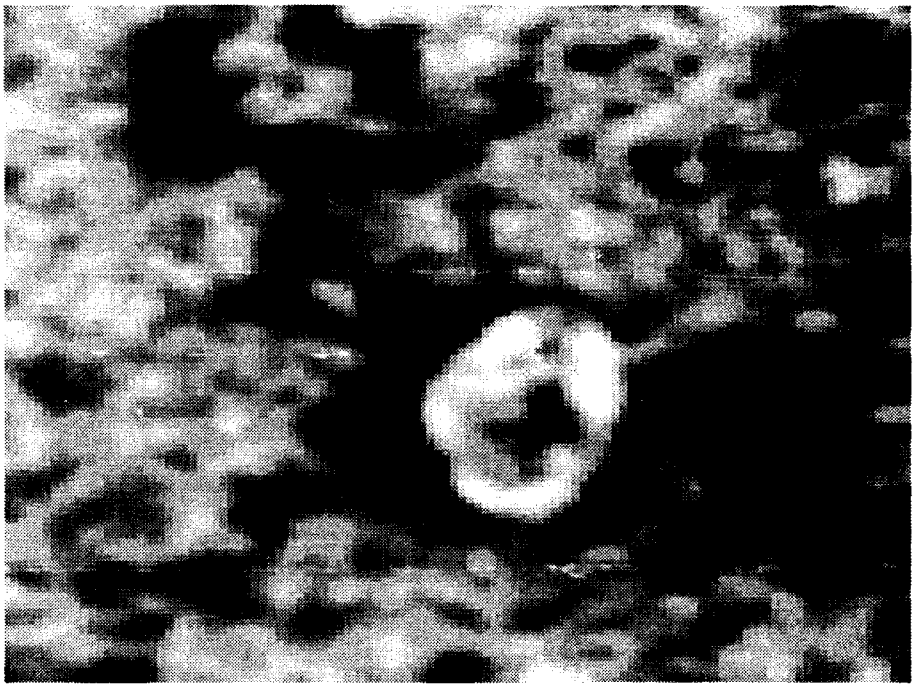

Figure 7b: Cu Auger electron micrograph of 1.7 ML Fe/Cu(100) subsurface islands. The image is 150 nm full scale (horizontal) and is from the identical area as Fig. 7a.

Figure 7c: Fe Auger electron micrograph of 1.7 ML Fe/Cu(100) subsurface islands. The image is 150 nm full scale (horizontal) and is from the identical area as Figs. 7a and 7b.

behavior while also allowing for the modification of the growth mode due to differences in surface free energy. In addition, since the magnetic surface anisotropy is very sensitive to the chemical state of the surface , one is led to suspect that the surface segregated oxygen will drastically alter the magnetic behavior of ultrathin films of Fe on Cu(100).

We examined the details of the magnetization switching process for as-deposited 4.7 ML thick Fe where the perpendicular anisotropy just cants into plane.[See Surface Magnetization Processes Investigated by The Combined Surface Magneto-Optical Kerr Effects in Fe/Cu(100) Thin Films by Z.J. Yang, S.D.Healy, K.R.Heim, J.S.Drucker, G.G.Hembree, and M.R. Scheinfein in the Appendix]. In Fig. 8a-d, SMOKE loops are shown for applied fields along the longitudinal (on plane), 45^{o} from longitudinal (in plane), transverse (in plane), and normal to the film surface (polar) directions respectively. A coherent rotation model was employed to interpret these results. The normalized energy functional is given in eqn. 1, where K_{in} and K_{out} are the in-plane and out-of-plane anisotropies, M_S is the saturation magnetization, H_l, H_t, and H_p are the longitudinal, transverse and polar applied magnetic fields, θ is the polar angle (from the polar direction), ϕ is the azimuthal angle (from the longitudinal direction), α defines the out-of-plane easy axis angle, β defines the direction of the easy axis in the film plane, and c is a constant whose value is 1 (2) for uniaxial (cubic) in-plane anisotropy. External fields include the ramping field and any residual external stray fields. This expression was minimized using a conjugate

gradient method. The results of this minimization are shown in Fig. 9a-f. The computed loops are meant to indicate gross structure as a means of interpreting the SMOKE results, and discrepancies between the computed loops and the measurements are due to the crudeness of the model (i.e. no domain walls or domain wall motion).

$$E = \frac{1}{2}\sin^2(\theta-\alpha) + \frac{1}{2c}\frac{K_{in}}{K_{out}}\sin^2\{c(\phi-\beta)\}\sin^2\theta + \frac{2\pi M_s}{\left[\frac{2K_{out}}{M_s}\right]}\cos^2\theta - \left\{\frac{H_l}{\left[\frac{2K_{out}}{M_s}\right]}\sin\theta\cos\varphi + \frac{H_t}{\left[\frac{2K_{out}}{M_s}\right]}\sin\theta\sin\varphi + \frac{H_p}{\left[\frac{2K_{out}}{M_s}\right]}\cos\theta\right\} \quad (1)$$

The in-plane anisotropy is cubic, and oriented at 45° from the longitudinal direction. The perpendicular anisotropy is uniaxial and oriented 10° out of the film surface. The out-of-plane anisotropy was twice as large as the in-plane component, and equal to $2\pi M_s$. Figs. 9a-d show SMOKE hysteresis loops computed for the identical conditions described for Figs. 8a-d. Since the polar Kerr signal contains both longitudinal and polar components, Fig. 9e and f show the polar and longitudinal components respectively. The polar signal is 5 times as large and of opposite sign than the longitudinal signal. The general features are the asymmetrical structure on the corners of the loops in Figs. 8b and 9b, the twin peak structures in Figs. 8c and 9c, and the canted/inverted loops in Figs. 8d and 9d. When the field is applied in the transverse direction, a small stray field forces the loops to close in the same direction, thus not completing a 360° rotation in-plane. This is strong evidence for in-plane biaxial anisotropy. When the field is applied along the polar direction, the magnetization rotates from a direction perpendicular to the plane into the plane as the field is reduced. As the field changes sign, the magnetization rotates in the plane of the surface first, aligning itself with the projection of the easy magnetization direction in the plane of the film. As the field is further increased, the linear magnetization curve is once again observed. Upon return, the magnetization rotates within the film plane thus completing at least a 180° rotation within the film plane during the switching process. These observations provide direct evidence for a canted induced uniaxial anisotropy.

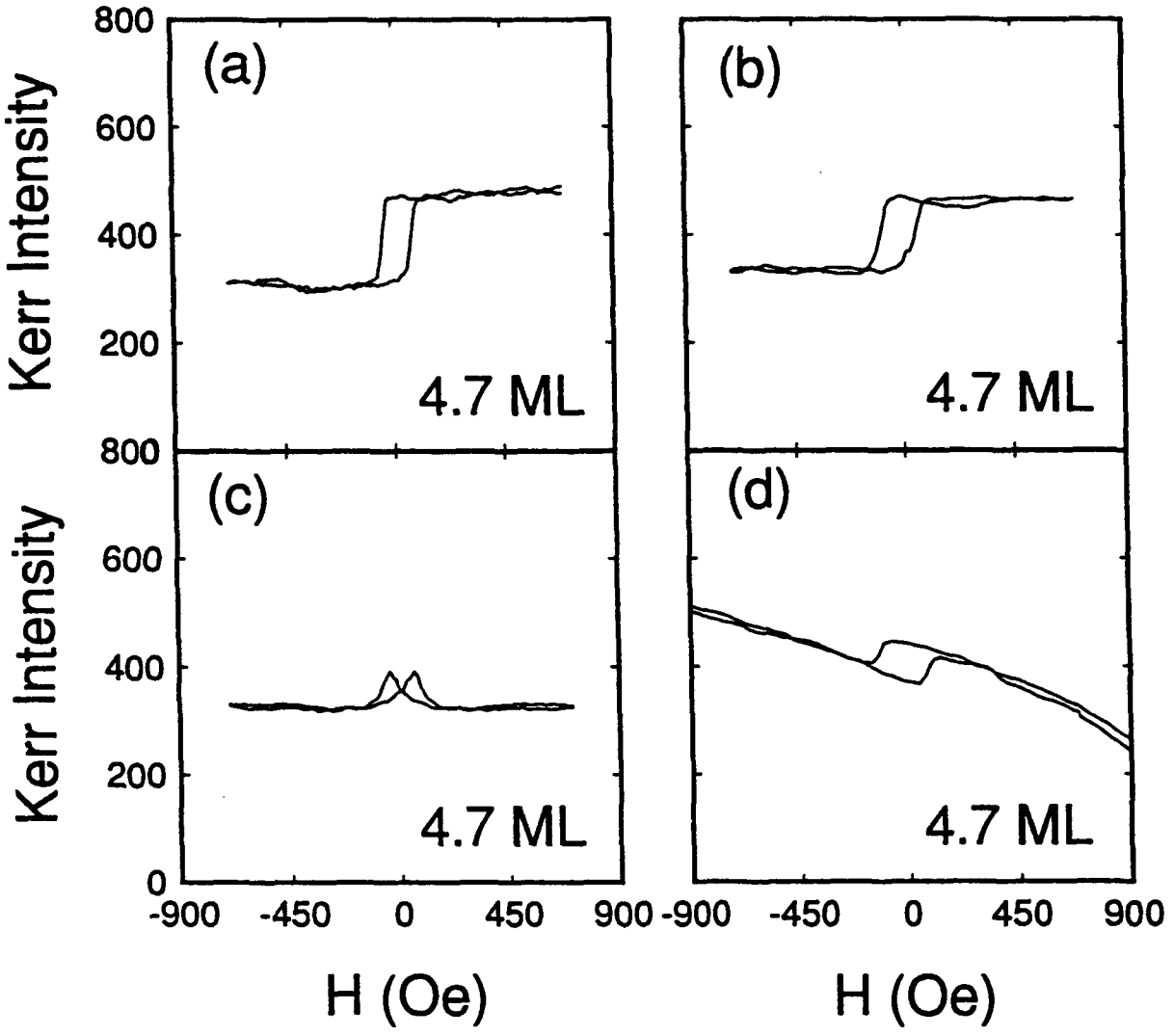

Figure 8: SMOKE loops are shown for applied fields along the (a) longitudinal, (b) 45^{o} from longitudinal, (c) transverse, and (d) normal to the film surface (polar) directions respectively. Applied fields in a-c are in the film plane.

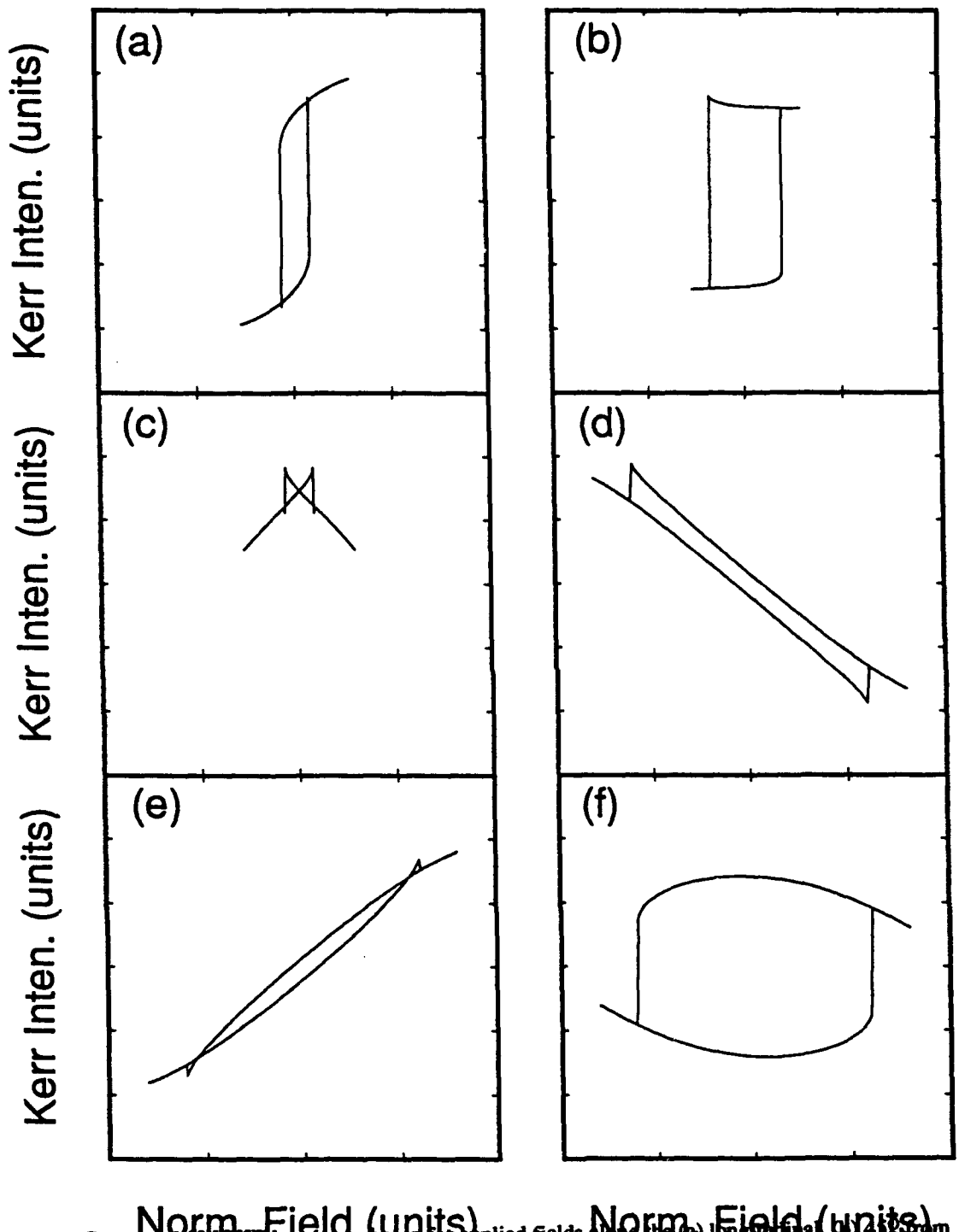

Figure 9: Computed SMOKE loops are shown for applied fields along the (a) longitudinal, (b) 45° from longitudinal, (c) transverse, and (d) normal to the film surface (polar) directions respectively. Since the polar Kerr signal contains both longitudinal and polar components e and f show the polar and longitudinal components (to 3d) respectively.

4.0 bcc Fe/Ag(100)

In preparation for the magnetic and growth studies to be performed on the Fe/Ag(100) system, we attempted to establish a technique for obtaining a clean, well-ordered Ag(100) surface. Although we were able to clean the silver sample, it was difficult to obtain a well-ordered, single crystal surface. Fig. 10a shows a secondary electron (SE) image of the Ag(100) polycrystalline surface. The reason the surface is polycrystalline is because the top layers of the surface (down to a few microns) were damaged as a result of the mechanical polishing procedure. This damage was not removed electrochemically.

Although the most common type of electropolishing solution used for silver contains potassium cyanide, Heinrich et al (Appl. Phys. A **49**,473 (1989)) have developed an alternative technique which is based on the work of Lyles et al (Metallography **11**,361 (1978)). The technique uses a solution consistsing of glacial acetic acid (CH_3COOH), sulfuric acid (H_2SO_4),methanol (CH_3OH), and thiourea (NH_2CSNH_2). The results of this electropolish procedure are shown in Fig. 10b. The contrast in this SE image arises from asperities on the surface and from step edges. The large terraces, which have a width of ~130nm, are devoid of any channeling contrast indicating that this procedure eliminated the damage caused by mechanical polishing and left behind a single crystal surface. We are in the process of growing bcc Fe on these crystals, and given the high Auger sensitivity of this system, we are confident that we will be able to explore in some detail the initial phases of epitaxy while we explore the onset of ferromagnetism.

5.0 Fe/CaF_2/Si(111)

For very slow growth rates the adsorbate topology is expected to approximate structures produced under equilibrium conditions. In this regime, the growth mode is controlled by surface energy imbalances where a system in equilibrium can be characterized in terms of the surface energy of the adsorbate (γ_a), substrate (γ_s), and the interface between them (γ_i). When $\gamma_a + \gamma_i > \gamma_s$ the deposited material is not expected to spread evenly over the substrate's surface. Fe and CaF_2(111) are known to possess surface energies of 2475 erg/cm^2 and 450-550 erg/cm^2 hence, Fe island formation on CaF_2 is expected. We are interested in the formation of monodisperse transition metal island size distributions because ferromagnetic or paramagnetic granules embedded in a three-dimensional noble metal matrix have been shown to exhibit giant magnetoresistive behavior if the granules are properly spaced and smaller than some critical radius. This leads to the natural extension whereby a two-dimensional array of isolated ferromagnetic particles, such as Fe islands on an insulating CaF_2 substrate, covered by a noble metal is expected to yield two-dimensional giant magnetoresistance (GMR) effects. In addition, since CaF_2 can be chemically altered by electron beam exposure, growth modes may be

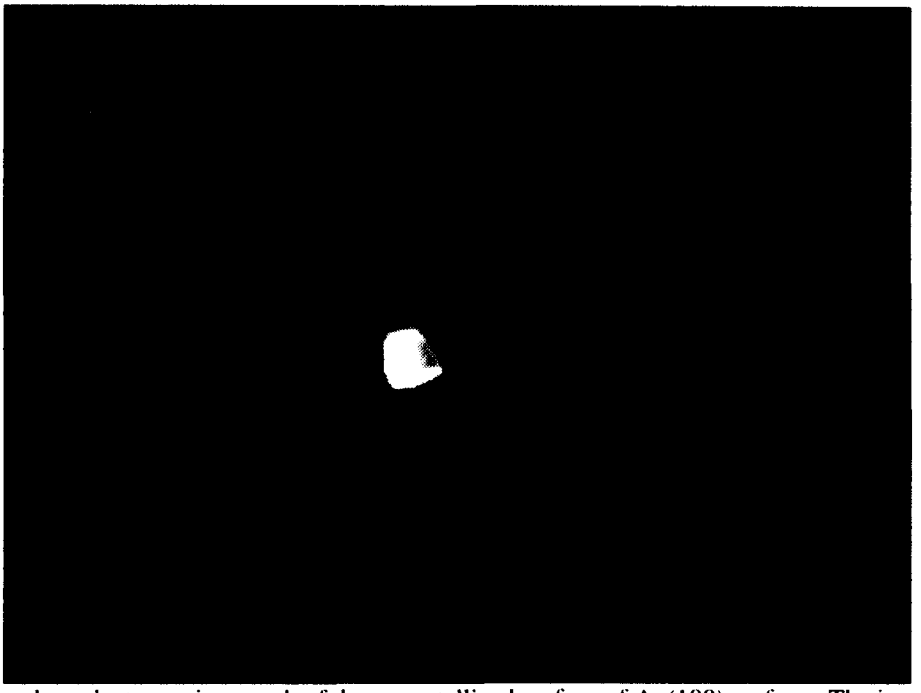

Figure 10a: Secondary electron micrograph of the recrystallized surface of Ag(100) surface. The image is 1.2μm full scale (horizontal).

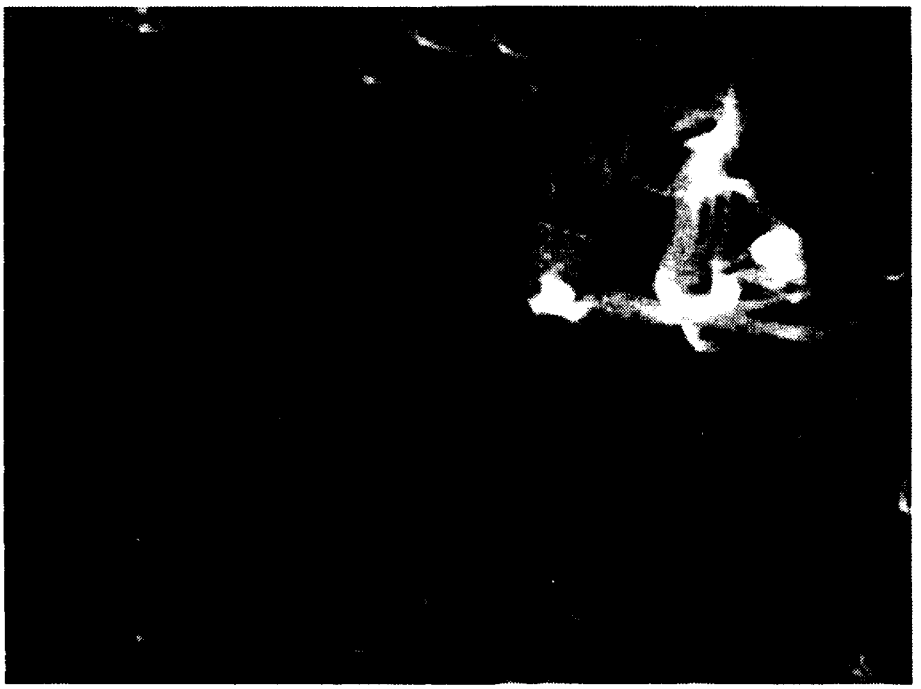

Figure 10b: Secondary electron micrograph of the single crystalsurface of Ag(100) surface. The image is 1.2μm full scale (horizontal).

controlled for selected regions of the surface prior to metal deposition by modifying the surface composition with an electron beam. A further increase in electron irradiation and exposure to residual oxygen allows the CaF_2 to be used as an electron beam resist, thereby expediting the fabrication of nm-size and low dimensional magnetic devices.

SE microscopy was performed before and after (radiatively) annealing the CaF_2/Si(111) substrates at 300 °C for 60 minutes, revealed that areas of obvious surface contamination were not reduced by heating. Broad-beam Auger electron spectroscopy (AES) displayed no statistically significant changes in the chemical composition of the CaF_2 surface after annealing for 60 minutes at temperatures up to 400 °C. Higher annealing temperatures do, however, produce significant changes in the surface morphology. An unannealed CaF_2/Si(111) specimen is shown in Fig. 11a. The saw-toothed step edge visible in Fig. 11a is a typical surface feature of the many samples observed. Fig. 11b indicates that, after a 60 minute, 400 °C anneal, numerous, almost triangularly arranged pits are formed. These morphological changes may have resulted from the relief of stresses present during the growth of the CaF_2. In order to prevent severe surface modifications (pitting) during cleaning, the substrates were either annealed for 60 minutes at 300 °C or for 24 hours at 170 °C prior to the Fe deposition. Obvious contamination occupied small, localized regions of the total CaF_2 surface area (10-30%), such that Fe island size distributions could be determined from regions between the contaminated areas.

The initial stage of Fe/CaF_2 growth proceeds by three dimensional islanding. Fig. 11c is an example of a 60 minute Fe deposition at a rate of 0.11 Å/min on a room temperature substrate. The relatively even distribution of 2.0 nm diameter Fe islands on a 100 Å thick CaF_2(111) surface is clearly displayed. Particle size analysis of the SE images revealed no statistical difference between the diameters and spatial distribution of Fe islands grown on 140 °C and room temperature CaF_2/Si(111) substrates. A post-growth anneal of 140 °C on room temperature grown films did not produce a noticeable change in the Fe island size distribution. Statistical analysis performed on a large variety of images yielded the following information for a 60 minute deposition of Fe (0.11 Å/min) on room temperature or 140 °C CaF_2/Si(111) substrates: (1) An average Fe island diameter of 2.0 ± 0.3 nm; (2) A range of Fe island diameters where 85% of the population will lie within 2.0 ± 1.0 nm; (3) An average Fe island separation of 2.0 ± 0.4 nm; (4) A 23% coverage of CaF_2(111) with Fe islands; (5) The number of Fe islands per unit area is 7.4×10^{12} islands/cm^2; (6) The mean distance between Fe island centers is approximately 3.7 ± 0.6 nm; (7) No geometric ordering of the islands was observed based on fast Fourier transform image analysis.

Fig. 11d displays a SE image of Fe islands on a 100 Å thick CaF_2/Si(111) surface and an oxidized Si(111) surface. The oxidized Si region is visible because the CaF_2 had locally lifted off of the Si crystal, perhaps during 3 mm disc preparations. The existence of Fe islands on the

Figure 11a: SE image of an unannealed CaF_2/Si(111) surface. The contrast is due to a saw-tooth step edge which commonly appeared on these surfaces The image is 250 nm full scale (horizontal).

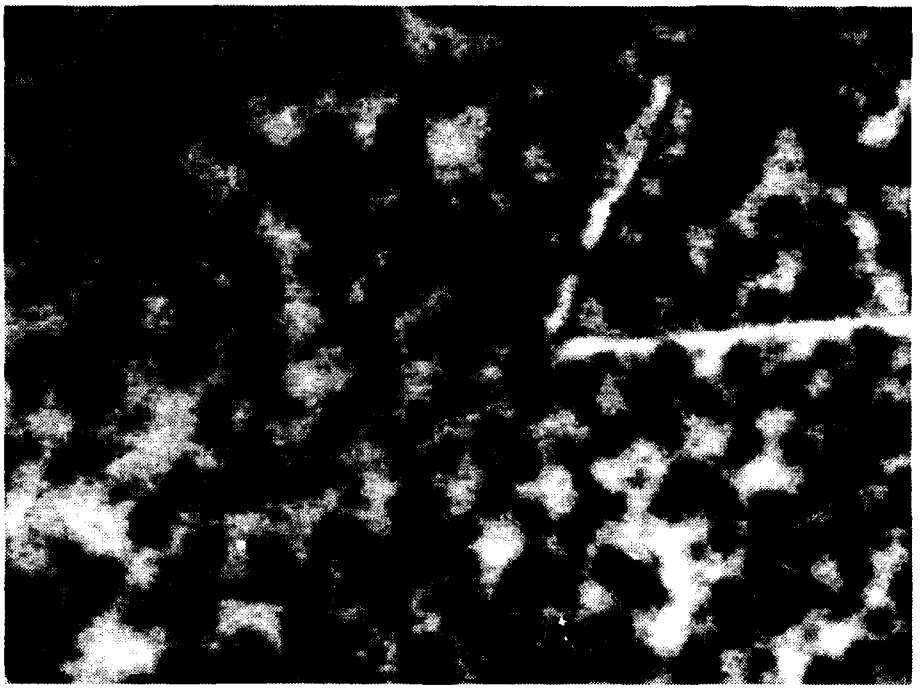

Figure 11b: SE image of a CaF_2/Si(111) sample that was annealed for 60 minutes at 400 °C. Morphological changes are apparent by the many triangularly oriented pits now covering the entire CaF_2 surface. The image is 250 nm full scale (horizontal)..

Fig. 11c: A 60 minute, room temperature Fe deposition at a rate of 0.11 Å/min on CaF_2/Si(111) produces a monodisperse Fe island distribution. Full scale is 240 nm (horizontal).

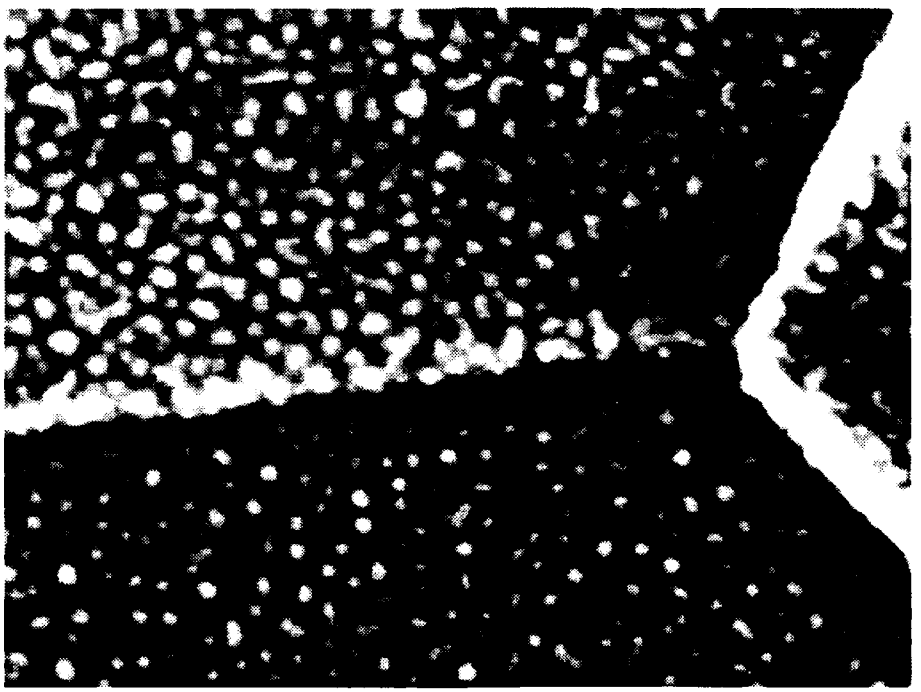

Fig. 11d: A SE image formed under the same conditions as Fig. 1c but in a region where some CaF_2 has locally lifted off the Si(111) substrate. Fe islands are visible on the CaF_2/Si(111) surface (top), the oxidized Si(111) surface (bottom), and the inverted CaF_2 surface (right). A difference in Fe mobility can be observed by comparing the mean inter-island separation between the top and bottom regions. Full scale is 120 nm (horizontal).

Si region, while also possessing a similar diameter as those on the CaF_2 region, suggests that the thermodynamically favorable reaction of silicide formation did not occur. It appears that the Si had been chemically changed into an insulating, lower surface energy, and less reactive SiO_2 surface. The difference of Fe mobility in the two distinct regions is made apparent by the difference in mean inter-island separation. In addition, the (position) stability of the Fe islands shown in Fig. 11d was monitored as a function of electron beam exposure. A SE image formed by subtracting two images of the same area taken after a total electron dose of 6000 C/cm^2 revealed that the Fe islands remained fixed in position on both the CaF_2 and the SiO_2 regions.

A simple energy calculation indicates that a hemispherically shaped, unstressed, and magnetically ordered Fe particle must contain a single magnetic domain for diameters on the order of a few tens of nanometers. This transition is a result of domain formation becoming energetically unfavorable as the magnetic particle becomes smaller due to the domain boundary energy becoming a large percentage of the total energy. The islands observed in Fig. 11c are smaller than the critical single domain size and separated by less than the mean free path of conduction electrons in metals (near 30 nm at room temperature for Cu). These properties make this system of nm-size Fe islands on an insulator, when covered by a noble metal, an excellent candidate for room temperature GMR studies which are now in progress.

Initial experiments have been performed with the aim of patterning the Fe structures in one and two dimensions. These studies have been undertaken on unrelaxed CaF_2/Si(111) surfaces such as the one shown in Fig. 12a. Deposition at room temperature of 0.7 and 1.7 nm of Fe, as shown in Fig. 12b and 12c respectively indicate the initiation of a simply connected percollative network suitable for two dimensional conductivity studies (which are underway currently). Surfaces such as these have also been coated with Ag in an attempt to passivate the surface and form continuous conduction paths for non-simply connected regions. In this way we can isolate contributions of individual conduction paths as being between non-connected ferro or paramagnetic Fe regions, as in Fig. 12b, or through simply connected regions, Fig. 12c. In Fig. 12d, a 0.7 nm thick Fe film was irradiated with an electron dose of 4.6 C/cm^2. Coalescence of the Fe islands into a continuous film has been initiated. We are exploring writing patterns in the Fe both before and after Fe evaporation. After Fe deposition, the islands coalesce. By damaging the CaF_2 surface and thereby raising the relative surface energy prior to deposition, nucleation may occur preferentially.

Figure 12a: The surface of unrelaxed CaF_2/Si(111) has no step edge kinks. The full scale is 1.2μm (horizontal).

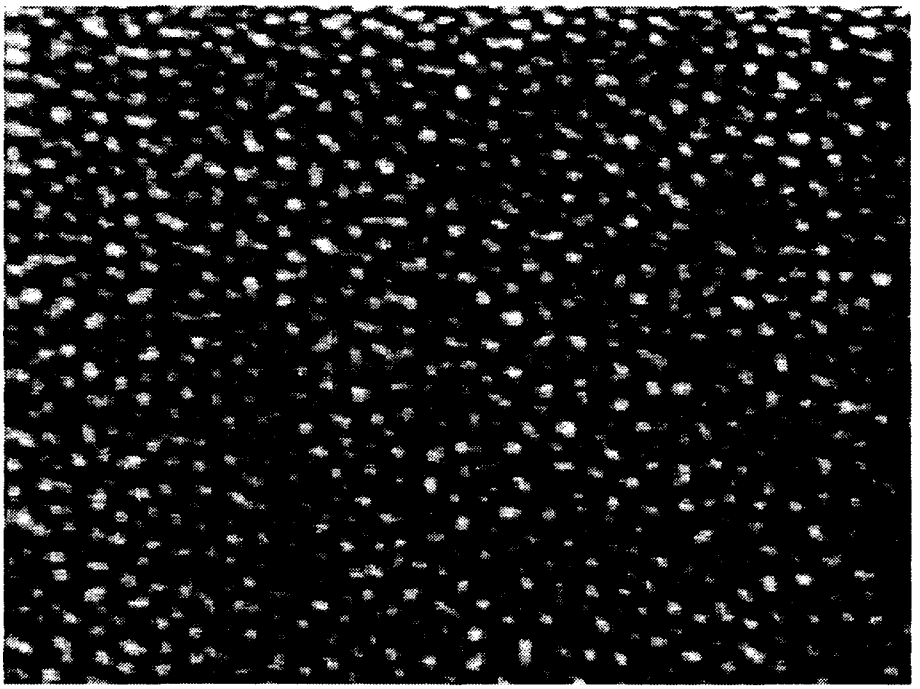

Figure 12b: The surface of unrelaxed CaF_2/Si(111) with 0.7 nm of Fe deposited at room temperature. The full scale is 120 nm (horizontal).

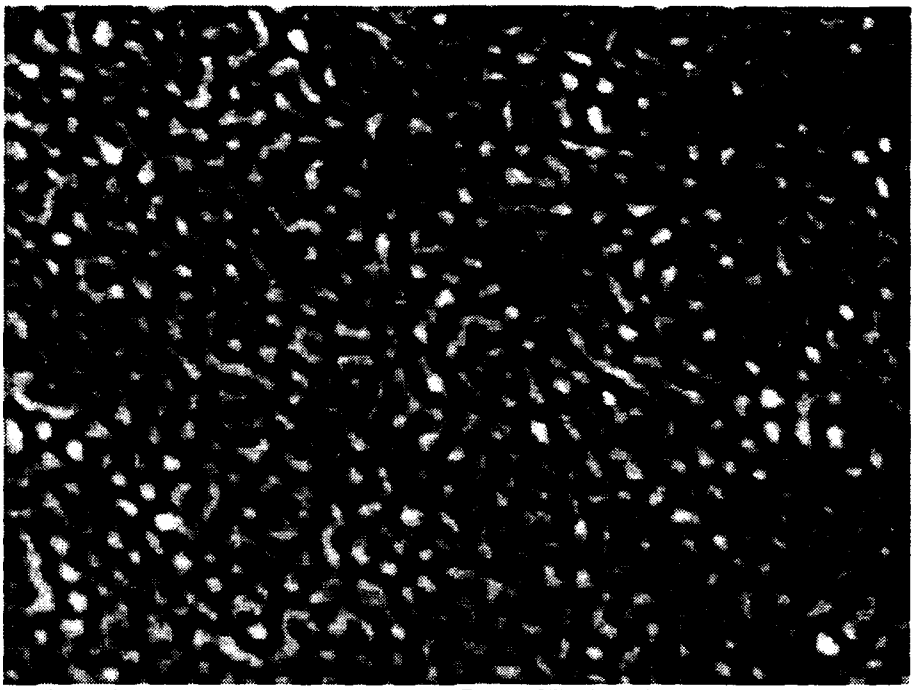

Figure 12c: The surface of unrelaxed CaF_2/Si(111) with 1.7 nm of Fe deposited at room temperature. The full scale is 120 nm (horizontal).

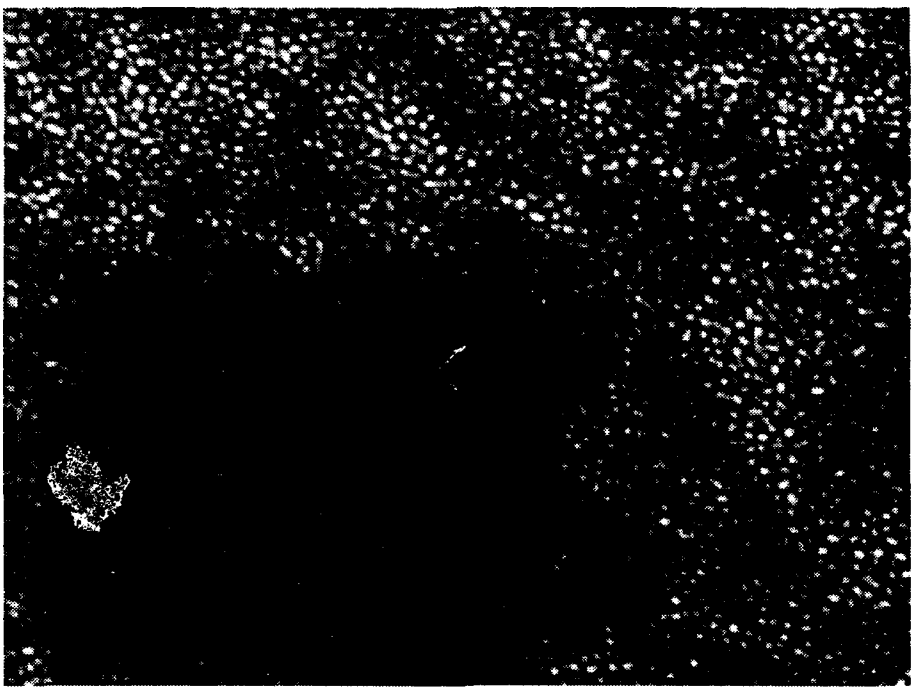

Figure 12d: The surface of unrelaxed CaF_2/Si(111) with 0.7 nm of Fe deposited at room temperature, after irradiation with 4.6 C/sm^2 . The full scale is 240 nm (horizontal).

6.0 Research Plans : Year 2

Year two will continue with the metal/metal interface characterization in both the fcc Fe/Cu(100) and bcc Fe/Ag(100) systems. We will explore the growth of fcc Fe/Cu(100) at elevated temperatures to test for metastable states. The Fe/CaF_2/Si(111) effort is taking off now. We have very recently begun measurements of giant magnetoresistance in these well characterized two dimensional films. We have been moderately successful at micropatterning 10 nm square Fe regions on the CaF_2 surface, and we are exploring methods to measure the magnetic properties of these regions microscopically using both scanned probe and scanned electron beam methods. We have begun a study of the Co/Cu(100) system which has had the highest reported thin-film magnetoresistances to date. We will grow films both in-situ in our UHV STEM, and characterize the interfaces and magnetic properties with SMOKE, while growing other films in our newly acquired dual source electron beam evaporation system. We are systematically exploring the role of in-plane magnetic order and domain formation with the giant magnetoresistance properties of these films. Specifically, we will grow identical films to be used for conductivity measurements, Kerr measurements, and STEM electron holography measurements. By correlating the SMOKE with GMR for in-situ and ex-situ grown films, and analyzing the resultant domain structures in STEM, we will be able to ascertain whether the domains span the spacer boundaries, and whether or not the main contribution to the GMR effect in intra or inter plane scattering. Now that we have got the system up and running, in year two, we will also begin our quantitative growth studies, where measurements will be compared with specific growth models.

7.0 Appendix A: Associated Staff

We currently have 7 people associated with this project. M. Scheinfein, an Associate Professor in the Department of Physics and Astronomy receives 2 months of summer salary from the grant. G. Hembree, an Associate Research Scientist in the Department of Physics and Astronomy is on a 12 month University salary and receives no salary from the grant. J. Drucker, a Research Scientist in the Center for Solid State Science receives 37.5% ($15,000) of his salary from the grant. Sean Healy, Kevin Heim, Marian Mankos and Zhijun Yang are graduate research associates in the Department of Physics and Astronomy. Sean Healy was supported 100% time for the 1993 year. He will be a department teaching assistant in the spring of 1994 while still performing research on this project. Kevin Heim was supported (100%) in the fall of 1993 and will continue in 1994. He will graduate between January and June 1995. Zhijun Yang was supported (100%) in 1993 and will continue in 1994. He will graduate between January and June 1995. While Marian Mankos is a team member on this project, he is supported on a Department of Energy grant with John Cowley and thus extracts no stipend.

8.0 Appendix B: Publications

Revised 10-9-93 Murray

Correlations between ultrathin film microstructure and magnetic properties for room temperature epitaxial films of fcc Fe/Cu(100)

K. R. Heim, S. D. Healy, Z. J. Yang, J. S. Drucker,[a] G. G. Hembree, and M. R. Scheinfein
Department of Physics and Astronomy, Arizona State University, Tempe, Arizona 85287-1504

(Received 15 July 1993; accepted for publication 30 August 1993)

Correlation studies between thin film nanostructure and macroscopic magnetic properties in ultrathin fcc Fe films grown epitaxially on room temperature Cu(100) substrates were performed *in situ* using an ultrahigh vacuum scanning transmission electron microscope and the surface magneto-optic Kerr effect. Nanometer lateral spatial resolution secondary electron microscopy revealed no gross morphological changes in the 2–10 monolayer thickness range. The use of broad-beam Auger electron spectroscopy as an indicator of Cu surface cleanliness is shown to have insufficient sensitivity to detect surface contamination as evidenced by corresponding secondary electron micrographs. Cu(100) surfaces with both (nearly) perfect and imperfect surface structure, and identical Fe coverages, possess nearly identical polar and longitudinal Kerr hysteresis loops. Analysis of reflection high-energy electron diffraction patterns confirms that Fe films grown on room temperature Cu(100) remain fcc with the same in-plane lattice constant as the Cu template, for thicknesses up to 10 ML.

I. INTRODUCTION

The translational symmetry of a perfect crystal is lost by the formation of a surface. Electronic and magnetic properties at the surface are modified due to this change in atomic coordination. One of the spectacular manifestations of symmetry breaking at the surface is the presence of surface anisotropy in ultrathin ferromagnetic films. Commonly exhibited as a perpendicular magnetic anisotropy, the surface anisotropy, its direction, and its strength have been the subject of intense study. In accordance with Mermin and Wagner's theorem,[1] the absence of anisotropy dictates that there can be no long-range magnetic order in a two-dimensional Heisenberg system. Hence, the presence of (surface) anisotropy stabilizes the magnetization in two-dimensional ferromagnetic ultrathin film systems. The surface anisotropy, when directed perpendicular to the surface, is often strong enough to overcome the shape anisotropy resulting in perpendicular magnetization and polar remanence. This behavior is observed in the fcc Fe/Cu(100) system where the strength and direction of the magnetization is a strong function of the growth temperature, growth conditions, film thickness, and measurement temperature. It is the complexity of both the structural and magnetic properties of fcc Fe/Cu(100) which results in this system being perhaps the most extensively studied ultrathin film ferromagnetic-metal system. Since growth conditions directly affect thin film growth, extreme efforts were taken to ensure that these measurements represent the growth of Fe on clean, room temperature Cu(100). In addition, the contamination level ascribed to each cleaned surface establishes a quantitative, rather than qualitative, value such that any effect on the magnetic behavior of the sample remains negligible.

The epitaxial growth of ultrathin, metastable Fe films on single-crystal Cu(100) substrates has produced a wide variety of disparate experimental results correlating the growth mode with magnetic behavior.[2–14] Unusual magnetic properties are associated with the fcc Fe/Cu(100) system. These include reversible magnetic anisotropies due to temperature changes[3–5] and large applied magnetic fields,[4,5] live surface layers,[6] and thickness dependent anisotropy.[6,7,10] These observations are inextricably linked to film morphology established during the initial stages of growth, variously characterized as layer-by-layer (Frank–van der Merwe),[12,14–17] simultaneous multilayer,[18] agglomeration,[6,8,15,19,20] segregation,[8,20–22] bilayer-by-bilayer,[20,22–24] as well as combinations of these growth modes. Inconsistencies in characterizing the growth and resulting film structure may well be explained, for example, by surface oxide contamination,[18,20,25] thus affecting the overall growth mode for this system. In this article we report on our combined magnetic and high spatial resolution structural characterization of the Fe/Cu(100) system.

The bulk phase of face-centered cubic (fcc) Fe does not exist at room temperature.[26] Metastable, ultrathin films of fcc Fe, however, have been grown epitaxially on Cu(100) substrates.[2–17,19–24,27–34] These films possess complex two-dimensional magnetic properties which may result from physical attributes such as strain in the epitaxial film due to lattice mismatch and film morphology induced during initial stages of growth by such parameters as surface and interface free energy differences, diffusion lengths, substrate temperature, and deposition rates. At room temperature, bulk, crystalline Fe is body-centered cubic (bcc, $a = 2.86$ Å) and ferromagnetically ordered below $T_c = 770$ °C.[26] The fcc ($a = 3.6468$ Å at 916 °C) γ-Fe phase at 910 °C is not ferromagnetic. The extrapolated room temperature lattice constant of 3.59 Å at 20 °C is obtained (using the thermal expansion coefficient) for γ-Fe, which yields a 0.68% lattice mismatch with the fcc Cu(100) substrate. A tetragonally distorted, ferromagnetic fcc struc-

[a] Also with center for Solid State Science.

 0021-8979/93/74(12)/1/9/$6.00

ture has also been reported[6,27,28] for the room temperature grown Fe/Cu(100) system.

The various structural properties of ultrathin films of Fe on Cu have been studied using methods such as medium-energy electron diffraction (MEED),[19,28] low-energy electron diffraction (LEED),[2,3,6,7,10–14,16,17,19–23,27–30] reflection high-energy electron diffraction (RHEED),[8,15,20] electron-energy-loss spectroscopy (EELS),[17] Auger electron spectroscopy (AES),[3–5,10–14,16,17,19,21,23,27–29] Auger electron diffraction (AED),[22] surface extended x-ray-absorption fine-structure spectroscopy (EXAFS),[29] x-ray photoelectron spectroscopy (XPS),[8,20] scanning tunneling microscopy (STM),[24] secondary electron microscopy with polarization analysis (SEMPA),[12] secondary electron (SE) imaging,[4,5,31,32] and Auger electron (AE) imaging.[4,5,31,32] Magnetic measurements have been performed using techniques such as magnon light scattering (MLS),[11] surface magneto-optic Kerr effect (SMOKE),[2–4–7,10,11,31,32] SEMPA,[34] spin-polarized electron spectroscopy,[3,12,14] ferromagnetic resonance,[8] Brillouin light scattering,[8] and conversion-electron Mössbauer spectroscopy.[13]

Our *in situ* growth and characterization experiments were performed using an ultrahigh vacuum scanning transmission electron microscope (UHV-STEM) with an attached analysis and preparation chamber. This combined surface analysis system includes AES, RHEED, SMOKE, and high-resolution SE and AE imaging. The capabilities of this microscope, including a description of the high resolution SE and AE imaging, have been reported elsewhere.[35,36] This microscope has been employed in similar nanostructural film growth studies.[37,38] All surface preparation, growth, and analysis was performed under continuous ultrahigh vacuum (UHV) conditions.

We conclude that for room temperature growth all films thinner than 10 ML (ML denotes monolayer) remain fcc and matched to the Cu(100) template, the onset of ferromagnetism occurs around 2 ML, growth does not initially proceed in a layer-by-layer mode (possibly simultaneous bilayer-by-bilayer), films within the range of 2.5 and 3.5 ML are capable of reversible, metastable magnetic anisotropy transitions,[3–5] films between approximately 2 and 5 ML in coverage are ferromagnetic at room temperature, and films thicker than 5 ML but less than 10 ML are nonmagnetic at room temperature. All Cu(100) surfaces were ion sputtered and annealed so that the effects of contamination and surface roughness were minimized. As a result, an oxide impurity coverage of 1.1% was not sufficient to alter the magnetic behavior of the Fe films relative to those possessing more pristine surfaces. In addition, no gross morphological changes were observed for coverages within 2 and 10 ML using nanometer lateral spatial resolution SE microscopy. Therefore, gross structural variations are not responsible for changes in the magnetic anisotropy within the 2–10 ML regime.

II. EXPERIMENTAL PROCEDURE

Our magnetic thin film growth and characterization facility is schematically depicted in Fig. 1. The foundation of this system, shown on the far left-hand side of Fig. 1, is a modified Vacuum Generators HB501-S, field-emission scanning transmission electron microscope (STEM).[39,40] A magnetic parallelizer (P)[41] guarantees nearly 100% collection efficiency at SE energies, and nearly 50% collection efficiencies at intermediate Auger energies (300–500 eV).[42] This high collection efficiency and the ability to form subnanometer 100 keV focused electron probes allows for the acquisition of nanometer transverse spatial resolution secondary and Auger electron images.[35,36] A secondary electron (SE) detector located below the sample facilitates in the study of bulk specimens (S). This electron microscope and the attached preparation chamber enables growth and characterization under UHV conditions using high resolution imaging and standard surface science techniques. A 24 h, 170 °C bakeout of the entire microscope and preparation chamber produces base pressures below 5×10^{-11} mbar. The specimen preparation chamber is equipped with a sample heater (H), a surface magneto-optic Kerr effect (SMOKE) analysis chamber, a Perkin–Elmer model 10-155 cylindrical mirror analyzer (CMA) broad-beam Auger analysis system, a scanning ion sputtering gun (Ar^+), a residual gas analyzer (RGA), various Knudsen cell evaporation sources ($K1$, $K2$, and $K3$), and an electron-bombardment Fe evaporator. The combination of *in situ* SMOKE measurements with nanometer-resolution microstructural characterization techniques makes this observation system ideal for correlating thin film surface microstructure (those structures with features larger than 1 nm) with macroscopic magnetic properties.

Single crystal Cu(100) substrates were machined into 1-mm-thick, 3-mm-diam, shouldered disks and commercially electropolished.[43] Each crystal was rinsed in trichloroethylene (TCE), acetone, and then methanol before insertion into the vacuum chamber. After attaining pressures below 5×10^{-11} mbar the Cu specimens were sputtered with 600 eV Ar^+ ions at 45° from the surface normal. Typical ion currents were between 200 and 250 nA (current densities of ~10 mA/cm^2) with an operational pressure of 6×10^{-7} mbar. Specifically, the Cu crystals were first sputtered at room temperature for 1 h. Next, the Cu was heated to ~330 °C and hot-sputtered for 4 h. Following this, the Cu was annealed at ~600 °C for 15 min to produce a well-ordered surface, as observed with RHEED. Recleaning samples with less than 10 ML (1 ML = 1.805 Å) of Fe on them required a ~330 °C sputter period of 1 h. Any cleaned surface exposed to ambient vacuum conditions for more than several hours or exposed to an electron beam (Auger spectroscopy, RHEED, or electron microscopy) was, prior to Fe deposition, cycled through a ~330 °C, 15 min sputter and a ~600 °C, 15 min anneal. The crystal was allowed to cool for 1.5–2.0 h after the last anneal such that a temperature below 40 °C was obtained prior to Fe deposition.

Following the surface preparation and Fe deposition, surface structural characterization was performed using secondary electron (SE) microscopy. SE microscopy contrast is sensitive to topography[38,44] and local changes in the work function.[45] Several of the cleaned Cu surfaces ob-

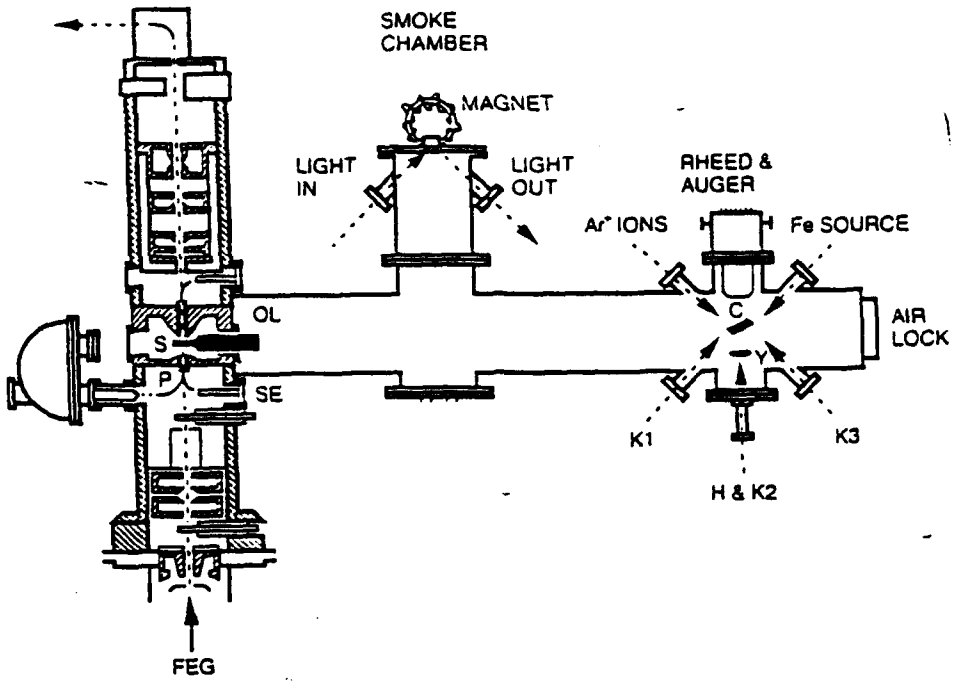

FIG. 1. Modified VG HB501-S thin film growth and characterization facility. The microscope column contains; electron parallelizer (P), secondary electron detector (SE), sample (S), objective lens (OL), and field emission gun (FEG). The specimen preparation chamber consists of a SMOKE chamber for surface magnetism analysis, a cylindrical mirror analyzer (CMA) for AES and RHEED, and sample surface preparation tools such as an Ar^+ ion sputtering gun, and Fe evaporator, a sample heater (H), and Knudsen cell evaporators ($K1$), ($K2$), and ($K3$). Also shown are the Cu crystal (C), the YAG crystal (Y), and the air lock for fast sample entry.

served with SE microscopy revealed small contaminant clusters which we believe to be Cu_2O (based upon the most likely copper oxide formed at these temperatures and pressures[16]) islands nucleated over the entire Cu surface. Analysis of these SE images indicates that oxygen coverages ≤ 0.0011 at.% are well below the sensitivity of the broad-beam AES (typically sensitive to no better than 1 at. %) used in the preparation chamber. In Figs. 2(a)–(f) we display corresponding broad-beam Auger spectra and SE images for two identically prepared Cu surfaces. Figures 2(a) and 2(b) are the respective $EN(E)$ and $dN(E)/dE$ spectra acquired for a clean Cu(100) surface. These spectra clearly exhibit five Cu Auger peaks (58, 105, 776, 840, and 920 eV in the derivative mode) while not detecting the O (503 eV) peak (the sensitivity factors at 3 keV indicate that O is about two times more detectable than the 920 eV Cu signal, from which we conclude that the oxygen coverage is ≤ 2 at. %). The SE image shown in Fig. 2(c) represents a typical area of the clean Cu(100) crystal surface with less than 1.4×10^9 oxide particles/cm^2, thus yielding an oxygen coverage of 0.016 at. %. The typical terrace width on these Cu(100) surfaces varies from 25 to 75 nm, which, based on the uniform growth, is greater than the Fe atom diffusion length for this system. Thus, the effects of a rough and disordered surface on the magnetic properties have been reduced below a detectable level. Insulators and oxides, in general, have higher secondary electron yields than metals,[47] and hence appear bright in SE micrographs. In contrast, the Auger spectra in Figs. 2(d) and 2(e) also imply a clean Cu surface, but the SE image of Fig. 2(f) shows larger, more numerous (3.6×10^{10} particles/cm^2 of 10 nm average radius and 3.75 at. %) oxide particles populating the entire Cu surface. These observations substantiate the assertions of Argile *et al.*[18,25] that an O(520 eV) and Cu(63 eV) peak-to-peak ratio as low as 9×10^{-3} may actually result from a Cu surface capped with a complete monolayer of oxide. The importance of preparing a relatively oxygen free Cu(100) surface prior to Fe deposition is given by Steigerwald *et al.*[20] *In situ* electron microscopy, with its high sensitivity for the detection of surface contamination, was used to guarantee the real space chemical and structural integrity of all Cu(100) substrates prior to Fe deposition. In particular, our cleanest Cu(100) surfaces had 1×10^9 particles/cm^2 of 3 nm average radius oxide clusters, implying an oxygen coverage of order ≤ 0.01 at. %, which is well below the detectivity of standard surface science techniques.

Thin films of fcc Fe(100) were grown only on clean Cu(100) (verified with SE microscopy) with an electron-bombardment evaporator. The evaporation rate was 0.14 ML/min with typical pressures of $1\text{–}2 \times 10^{-9}$ mbar, never exceeding 4×10^{-9} mbar during growth. The growth rate was determined by Auger electron spectroscopy (AES), Rutherford backscattering (RBS), and quartz-crystal microbalance. The Fe source consisted of a 1 mm diameter Fe wire of 99.9985% purity.[48] Thermocouple readings indicated that sample temperatures never exceeded 40 °C during growth. All depositions were made normal to the Cu surface with a source-tip to sample distance of $14.8 \pm .5$ cm. Previous to any experiments, all radiant sources, in-

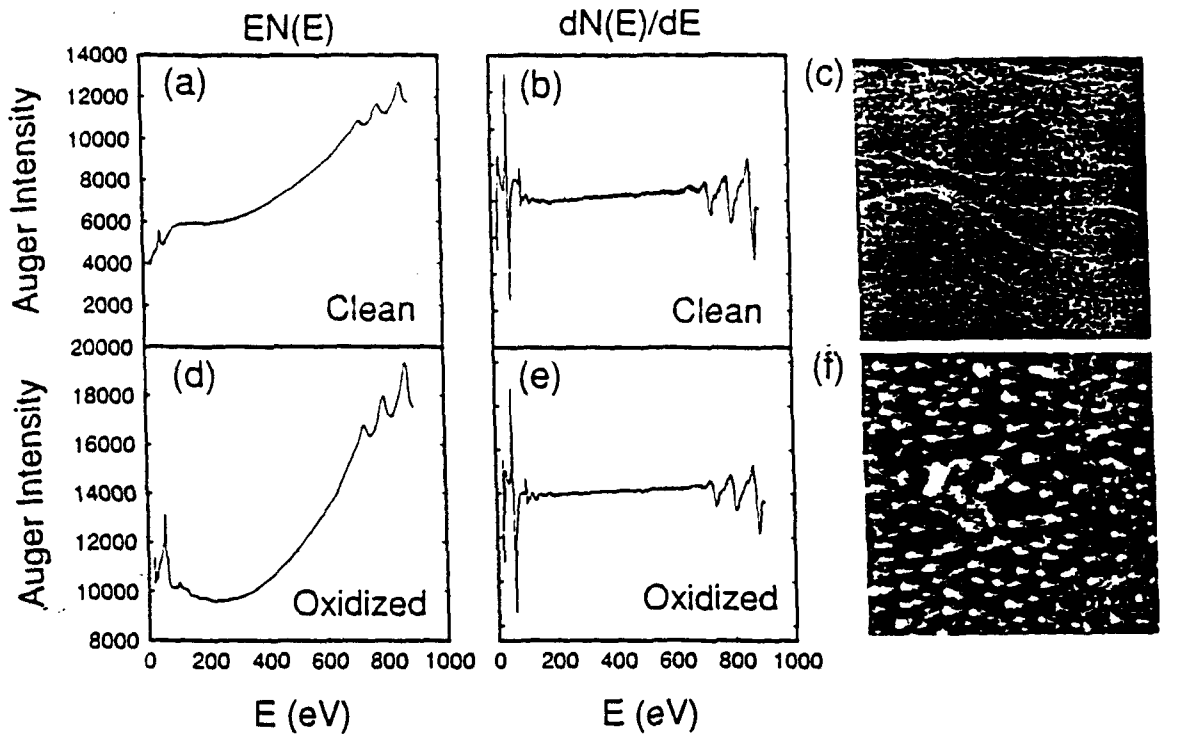

FIG. 2. Auger electron spectroscopy (AES) scans of clean copper in the (a) $EN(E)$ and (b) $dN(E)/dE$ mode with its corresponding (c) secondary electron (SE) image. The white curves are step bands separating terraces. The average terrace width lies within 25 and 75 nm. AES scans of oxidized copper in (d) $EN(E)$ and (e) $dN(E)/dE$ mode indicate no contamination while the (f) SE image reveals many oxide nodules.

cluding the Fe evaporator and annealing (sample) stage, were degassed well above their normal operating temperatures for at least 7 h.

AES is a convenient, efficient, and reliable method of determining *in situ* thin film coverages of Fe on Cu. The combination of AES, quartz-crystal microbalance, and RBS allowed us to relate an AES-derived coverage to methods that are not highly dependent on thin film morphology.[49] Fe thickness calibrations were performed in two ways using the 47 and 58 eV MVV peaks of Fe and Cu, respectively. All scans were obtained in the $EN(E)$ mode but were subsequently converted to the $dN(E)/dE$ mode. Peak to peak heights were measured from the $dN(E)/dE$ spectra. These measurements were then used in two slightly different manners.

The first evaporation rate calibration, shown in Fig. 3, is simply a plot of the natural log of the normalized Cu MVV peak height, times a constant versus time. A constant is necessary to obtain a slope in units of ML/ time. A value of 4.5 Å[50] for the escape depth of 58 eV electrons, 1.805 Å/ ML for fcc Fe in the [100] direction, and including the effect of the $-45°$ acceptance angle of the CMA yields the constant -1.76 ML. Although not shown, within the statistics of our measurements, a plot of the normalized Cu or Fe MVV peak height versus time displays no line breaks thus providing further evidence for a simultaneous multilayered growth mode as Argile *et al.*[18] have suggested. The second method assumes an exponential increase in the Fe MVV peak height, an exponential decrease in the Cu MVV peak height, and an escape depth of 4.5 Å for both Fe and Cu MVV electrons. After adjusting for the different intrinsic sensitivities between Fe and Cu MVV electrons, the two expressions are equated, allowing the thickness of Fe deposited as a function of time to be extracted. This method also assumes a simultaneous multilayered growth mode.[18] The SE images recorded following the Fe growth substantiate this assumption. Both calibration methods yield similar results. An evaporation rate of 0.14 ML/ min was calculated from Fig. 3 using the first calibration method. Figure 3 also displays the consistency in which AES lends itself as a useful tool in quantifying thin film coverages. Although very little scatter (correlation coefficient $R = 0.986$) is observed over multiple-day runs, the inset of Fig. 3 depicts even less scatter ($R = 0.999$) for an experiment on a single day.

The sample was then transferred *in situ* to the SMOKE chamber for the analysis of magnetic properties after the Fe deposition. Polar, longitudinal, and transverse[33,51] hysteresis loops were recorded by scattering modulated, polarized light from a 632.8 nm intensity-stabilized He-Ne laser at a 45° angle of incidence. Electromagnets located *ex situ* (the longitudinal Kerr configuration is shown in Fig. 1) were used to apply continuous fields of 1.2 and 1.5 kOe in the polar and in-plane directions, respectively. After SMOKE analysis, the specimen was then transferred *in situ* to the electron microscope for 100 keV high spatial resolution AES, SE imaging, or AE imaging. Once the electron microscopy and SMOKE analysis were completed, the sample was returned to the growth area for RHEED and broad-beam Auger analysis. The CMA was

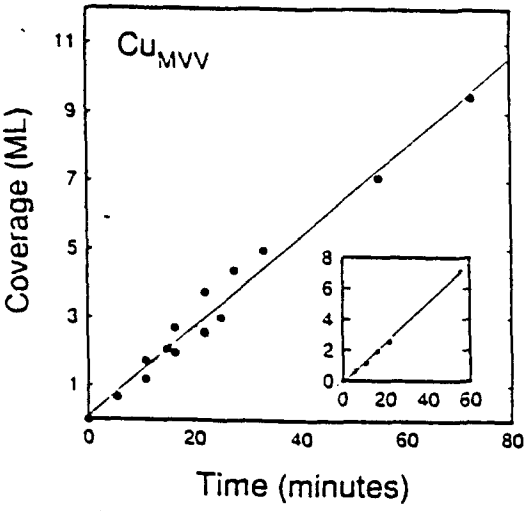

FIG. 3. Evaporation rate calibration using the Cu MVV electrons at 58 eV. The inset portrays the consistent linear results obtained during a single day as opposed to data acquired over many days. The abscissa and the ordinate of the inset are identical to those of the large graph.

used as a 3–5 keV electron source for RHEED. Our viewing abilities were limited to only one Laue zone where a 1.8-cm-diam yttrium-aluminum-garnet (YAG) screen was used to detect the diffraction pattern at a distance of 8.0 cm from the sample.

RHEED patterns were observed and recorded on 35 mm T-MAX 400 ISO black and white film. The diffraction patterns from Fe films of various coverages were used (0, 0.26, 0.70, 0.88, 3.50, 4.20, ~9, and ~10 ML) in calculations for determining the corresponding Fe crystalline phase (either fcc or bcc). Since only one Laue zone was visible per diffraction pattern we were limited to in-plane lattice parameter information. No determination of the Fe film's lattice constant in the out-of-plane direction could be made. Each sample was rotated about its surface normal so that repeated viewing was possible for the low index directions: ⟨100⟩ and ⟨110⟩. These multiple data sets resulted in better confidence intervals computed for the in-plane lattice constants. The lattice constant for clean fcc Cu(100) was used to compute the camera length for our CMA/YAG diffraction apparatus. By measuring the lateral spacing between individual RHEED spots we have concluded, to within ±4% standard deviation (variability in accurate positioning of the sample surface relative to the electron source and YAG screen is responsible for the relatively large standard deviation in our lattice parameter measurements), that films less than 10 ML in thickness remain in the fcc structure. These observations are consistent with those of Thomassen *et al.*[6] who observed that Fe films grown on room temperature Cu(100) substrates are fcc for coverages less than 11 ML. If the Fe had converted to its bcc bulk-like phase, the change in the in-plane lattice constant would be greater than 12%, which is well within our detectability limits.[52]

III. RESULTS AND DISCUSSION

SMOKE data were obtained by measuring the change in intensity of reflected polarized light as a function of applied field[33,51] at room temperature. Our results indicate that room temperature grown films thinner than 2.1 ML exhibit no magnetic behavior. The lack of ferromagnetic ordering for sub-2 ML films is consistent with the Fe-Cu atomic site exchange observed[32] for these low coverages. A minimum Fe island size is necessary so that the magnetic moment is stable against thermal fluctuations. Assuming a Boltzmann-type probability distribution, it can be shown that a majority of Fe islands (which average ~4 nm in diameter for sub-ML Fe films[32]) are below the size threshold for the magnetic moments to be unaffected by thermal energy. Films between 2.3 and 3.5 ML display ferromagnetic properties with a disposition towards out-of-plane remanence rather than in-plane remanence. Measurements at room temperature indicate a linear increase in SMOKE intensity as a function of film coverage in the ferromagnetic regime, a result in agreement with Thomassen *et al.*[6] whose measurements were made below room temperature (170 K) and extrapolated to 0 K. This magnetic signature is significantly altered by the subsequent exposure to the large polar fields required for high spatial resolution analysis in the electron microscope, as discussed in detail below. A simultaneous increase in the in-plane remanence and decrease in the out-of-plane remanence occurs for film coverages from 3.5 to 4.7 ML. However, films thicker than 5 ML but less than 10 ML appeared nonmagnetic at room temperature. Although many Fe coverages were investigated throughout the course of these experiments, only characteristic examples from the three main regions of interest (nonmagnetic, out-of-plane, transition to in-plane) were selected for discussion in this article. Polar (external field applied normal to surface) and longitudinal (external field applied both planar to the sample surface and in the scattering plane) Kerr hysteresis loops are shown for representative thicknesses of thin Fe films in Fig. 4, together with the corresponding Auger $[dN(E)/dE]$ spectra and high resolution SE micrographs.

We have observed a field-induced, reversible magnetic phase transition,[4,5] adding yet another unusual property observed for the fcc Fe/Cu(100) system. While this magnetic phase transition occurred for Fe film thicknesses within 2.5 and 3.5 ML, films of other coverages did not exhibit a similar phenomena. The objective lens (OL in Fig. 1) of the STEM subjects the specimen to a 9.0 kOe polar magnetic field during microstructural analysis. Subsequent SMOKE analysis revealed that the polar Kerr signal converts from a remanent polar hysteresis loop to that characterizing either a hard-axis ferromagnetic loop or a superparamagnetic response, while the in-plane hysteresis loop is unaltered except for a small increase in coercivity. A 1.5 kOe in-plane magnetic field was sufficient to return the film to its original polar ferromagnetic hysteresis loop. Also, but less effectively, a 25 °C temperature increase measured *ex situ* (the external stainless steel area surrounding the sample) returns the sample to the initial state, where the polar ferromagnetic loop becomes a superposition of

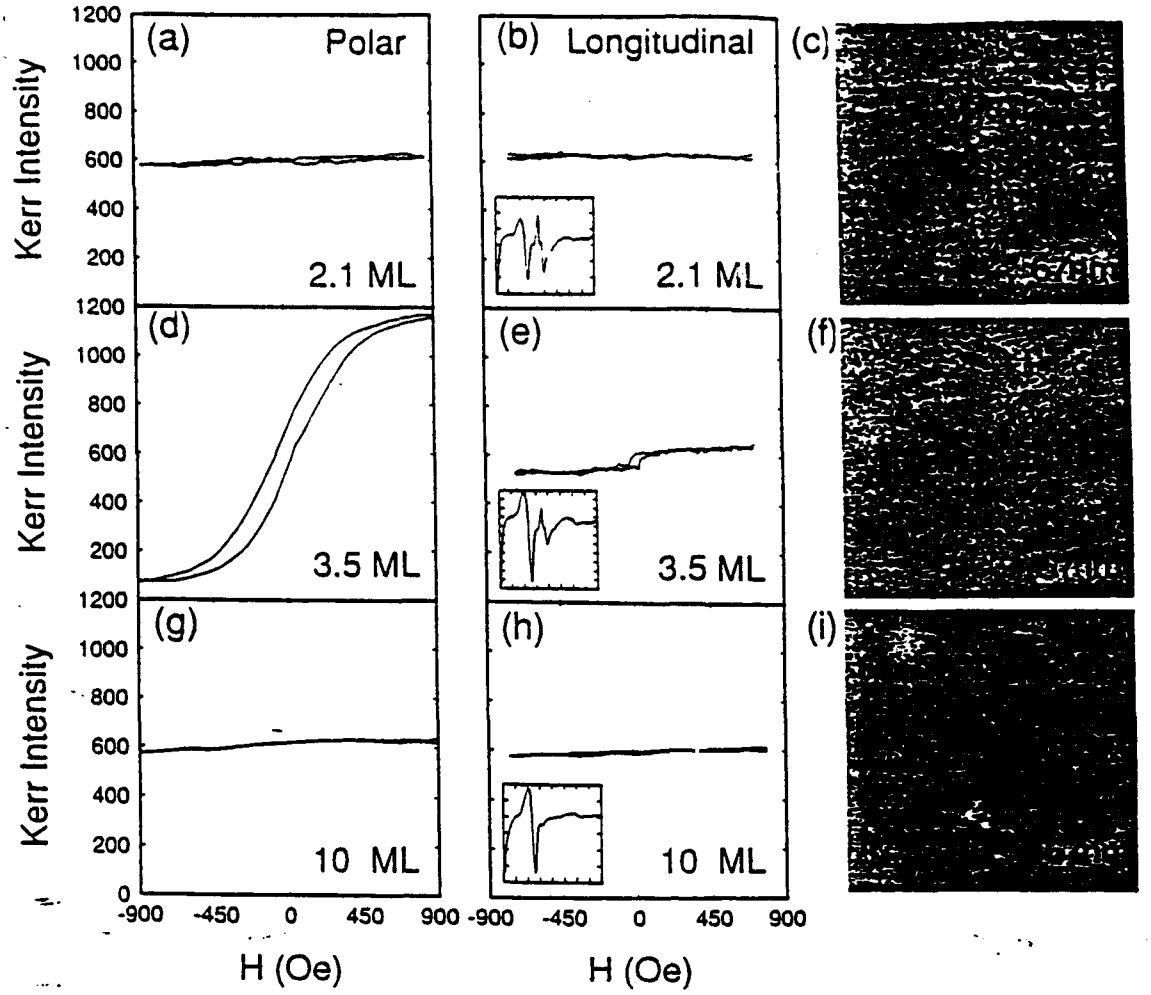

FIG. 4. Associated (a), (d), (g) polar Kerr, (b), (e), (h) longitudinal Kerr, and (c), (f), (i) secondary electron images for 2.1, 3.5, and 10 ML Fe films grown on room temperature Cu(100), respectively. The 10 ML film was grown in five stages over three days time. The insets located within the longitudinal Kerr plot are the respective $dN(E)/dE$ AES scans. The abscissa is a linear scale from 20 eV to 100 eV. The left-most peak and the right-most peak are those of the 47 eV Fe and 58 eV Cu MVV peaks, respectively.

both remanent polar and hard-axis (superparamagnetic) loops.

Theoretical calculations[53,54] of fcc Fe magnetic properties as a function of lattice constant predict that a lower energy, nonmagnetic phase of fcc Fe can be stabilized by a small decrease in the lattice constant. Therefore, small interatomic spacing changes normal to the surface could be responsible for the metastability (in the magnetic state and/or the magnetocrystalline anisotropy) in these films within 2.5 and 3.5 ML.[3,6,11] Although we could not measure the planar separation of the growth-direction Fe atomic layers, a small decrease in the lattice constant along the growth direction may result from the application of a large magnetic field (magneto-elastic compression) in that same direction. The effect of heating may serve to re expand the lattice dimension thereby reproducing the original ferromagnetic behavior. Measurements obtained with a typical RHEED apparatus do not allow for an extremely sensitive growth-direction lattice constant determination. As Thomassen *et al.*[6] conclude from their LEED experiments, growth-direction lattice spacing measurements with 0.02 Å resolution are necessary to quantify any lattice dimension changes on traversing the out-of-plane to in-plane magnetic anisotropy transition. Since a unified system possessing highly sensitive growth-direction lattice spacing measurements combined with an *in situ* SE microscope (for adequate surface characterization) does not exist, we must rely on separate experiments for our analysis.

SE images, such as those shown in Figs. 4(c), 4(f), and 4(i), indicate that there are no gross morphological changes (i.e., three dimensional island formation) between ferromagnetic ($2.3 < \Theta < 5$ ML) and nonmagnetic ($5 < \Theta < 10$ ML) Fe films. This conclusion has been reached independently using reciprocal space characterization techniques. Changes in lattice parameter and surface reconstructions have been observed using LEED,[6,11] while EXAFS[29] indicates that room temperature grown Fe/Cu(100) has similar in-plane and perpendicular nearest neighbor distances (interlayer spacings could not be measured individually with EXAFS). Although the disappearance of ferromagnetism through the reduction in the Curie temperature could be associated with small changes in the

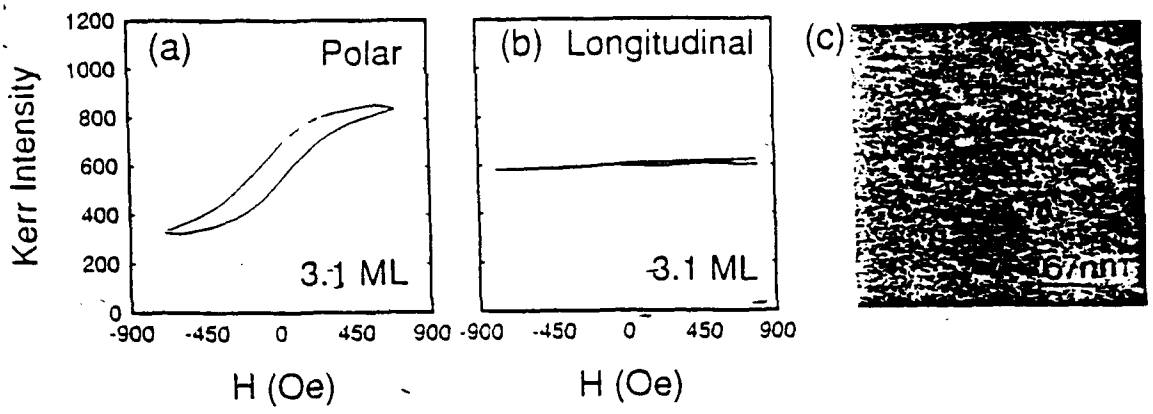

FIG. 5. A 3.1 ML Fe film grown on room temperature Cu(100) depicting a (a) polar Kerr hysteresis loop, (b) no in-plane magnetism, and a (c) partially contaminated Cu(100) surface. A mean distance of ~50 nm separates these contamination particles.

Fe film's lattice constant due to lattice-mismatch strain relief (formation of dislocations) and atomic reordering from energy-minimizing surface reconstructions,[6,11] there have been no direct correlations (repeated in different laboratories) made between such physical and magnetic properties. Our SE and AE imaging studies reveal that film coverages less than 2 ML are partially composed of local in-surface islands where Cu atoms vertically site-exchange with Fe atoms.[31] The lack of long-range order could thereby eliminate ferromagnetism. Simultaneous multilayered growth was observed for 2 ML films resulting in islands of 22 nm radius, typically separated by 13 nm. Again, this lack of long-range order may be responsible for the reported[4,5,7] absence of magnetic behavior for $\Theta < 2$ ML, room temperature-grown films of Fe on Cu(100).

Figure 4 portrays a representative sample of numerous Fe thin film depositions on room temperature Cu(100). The Kerr hysteresis loops denote the three regions of magnetic behavior for room temperature grown fcc Fe/Cu(100): Coverages less than about 2 ML are nonmagnetic, coverages between 2 and 3.5 ML are ferromagnetic with the easy axis canted at an oblique angle from the film normal,[33] and films thicker than 5 ML but thinner than 10 ML are no longer ferromagnetic. The SE images show no large-scale structural changes, thus indicating using real space techniques, that structural changes greater than 1 nm are not responsible for the anisotropy transition occurring near coverages of 4.7 ML. The growth mode appears not to have changed dramatically in that no three dimensional island formation was observed. The vertical site exchange process appears to be limited to films thinner than 2 ML. No crystallographic contrast changes were observed, consistent with the RHEED observations. A physical change in the growth direction, or structural changes that manifest themselves in structure below our nanometer lateral spatial resolution limit, or a subtle change in the electronic structure may be responsible for the changes in magnetic behavior with increasing thickness. No direct physical changes were observed in the films to account for the change in magnetic properties at the transition from perpendicular to in-plane anisotropy, and at the transition from above to below the Curie temperature.

In order to explore the effects of growth conditions on the resultant magnetic behavior, we have monitored a Cu specimen at several stages during interrupted growth. The film shown in Fig. 4(f) was composed of five unequal depositions over a period of three days. We have observed that an interrupted growth process, as that for the 10 ML film, produces equally smooth and nearly identical magnetic properties as for those films deposited in a single evaporation cycle. In addition, the four interruptions confirm that the Fe film's magnetic behavior throughout all stages (nearly) matches those of films produced by uninterrupted growth (slight differences in the thickness dependence are observed that are within the limits in the accuracy of the film thickness determination).

A 3.1 ML Fe film grown on a Cu(100) crystal with a mean contaminant cluster separation of 54 nm is displayed in Fig. 5(c). By comparing Fig. 4(f) with Fig. 5(c) we conclude that this small amount (2.2×10^{10} particles/cm^2 of 4 nm average radius and 1.1% total areal coverage) of contamination does not appear to affect the Fe film morphology at locations away from the contaminants. This observed morphology invariance is a result of the diffusion lengths (of order 10 nm) of metals on metals being much less than the mean contaminant cluster separation. The associated Kerr loops show polar remanence [Fig. 5(a)] and the lack of longitudinal remanence [Fig. 5(b)] just as for uncontaminated films in the regime near the onset of ferromagnetism ($2.3 < \Theta < 3.5$ ML). Although we did not observe any differences in magnetic properties between clean or slightly contaminated Cu substrates with a ~3 ML Fe deposition, the results are expected to be dramatic for other contaminants of different concentrations. For example, the effects of oxygen as a surfactant for the Fe/Cu system are discussed by Steigerwald *et al.*[20] They have found that an atomic layer of oxygen on the Cu surface produces better epitaxial growth of Fe overlayers. As the evaporations proceed the oxygen appears to surface segregate and thereby influences the epitaxial growth of subsequent Fe overlayers.

A consequence of oxygen surface contamination may

be realized in several ways. First, copper oxide particles fixed to the Cu surface, depending on their size and concentration, may act as nucleation sites during deposition thus affecting the overall growth mode of the system. Second, these same copper oxide particles, if large enough, possessing a lower surface free energy than the surrounding uncontaminated regions could affect the growth mode by inhibiting the uniform growth of Fe on the surface of the copper oxide. Finally, compound formation between oxygen or copper oxide and Fe comprises many phases. Compounds with nonmagnetic, antiferromagnetic, or ferromagnetic phases would undoubtedly alter the observed magnetic behavior while also allowing for the modification of the growth mode due to differences in surface free energy. In addition, since the magnetic surface anisotropy is very sensitive to the chemical state of the surface,[54,55] one is led to suspect that the surface segregated oxygen will drastically alter the magnetic behavior of ultrathin films of Fe on Cu(100).[6]

Therefore, the widespread use of broad-beam AES as a technique for determining Cu surface cleanliness, followed by Fe growth, may be responsible for the different growth modes reported for the Fe/Cu(100) system. However, real space imaging with nanometer spatial resolution affords us the ability to characterize surfaces (with chemical specificity) over a wide field of view.

IV. CONCLUSION

In situ magnetic and structural characterization of ultrathin films of Fe on Cu(100) was performed using SMOKE, RHEED, broad-beam AES, SE imaging, and AE imaging. Results indicate that room temperature grown films are nonmagnetic below 2.1 ML, are ferromagnetic between 2.3 and 5 ML, and are no longer ferromagnetic greater than 5 ML but less than 10 ML. SE and AE images reveal localized alloying and simultaneous multilayered growth for films less than 2 ML and no gross structural changes for films of order 10 ML. AES reconfirms a simultaneous multilayered growth mode due to the lack of breaks in the normalized MVV Cu peak-to-peak height curve as a function of evaporation time. Broad-beam AES was determined to be inadequate for determining the oxide contamination of Cu crystal surfaces because of a lack of detection sensitivity, and may account for the variability in some growth/magnetic properties studies in the fcc Fe/Cu(100) system.

ACKNOWLEDGMENTS

This work is supported by the Office of Naval Research under grant No. N00014-93-1-0099 and the National Science Foundation under grant No. DMR 89-14761. The microscopy was performed at the National Science Foundation supported Center for High Resolution Electron Microscopy at Arizona State University, grant No. DMR-91-15680.

[1] N. D. Mermin and H. Wagner, Phys. Rev. Lett. 17, 1133 (1966).
[2] P. Montano, G. W. Fernando, B. R. Cooper, E. R. Moog, H. M. Naik, S. D. Bader, Y. C. Lee, Y. N. Darici, H. Min, and J. Marcano, Phys. Rev. Lett. 59, 1041 (1987).
[3] D. P. Pappas, K. P. Kämper, and H. Hopster, Phys. Rev. Lett. 64, 3179 (1990).
[4] G. G. Hembree, J. S. Drucker, S. D. Healy, K. R. Heim, Z. J. Yang, and M. R. Scheinfein (to be published).
[5] K. R. Heim, S. D. Healy, Z. J. Yang, J. S. Drucker, G. G. Hembree, and M. R. Scheinfein (to be published).
[6] J. Thomassen, F. May, B. Feldmann, M. Wuttig, and H. Ibach, Phys. Rev. Lett. 69, 3831 (1992).
[7] C. Liu, E. R. Moog, and S. D. Bader, Phys. Rev. Lett. 60, 2422 (1988).
[8] B. Heinrich, J. F. Cochran, A. S. Arrott, S. T. Purcell, K. B. Urquhart, J. R. Dutcher, and W. F. Egelhoff, Jr., Appl. Phys. A 49, 473 (1989).
[9] F. J. Himpsel, Phys. Rev. Lett. 67, 2363 (1991).
[10] C. Liu, E. R. Moog, and S. D. Bader, J. Appl. Phys. 64, 5325 (1988).
[11] P. Xhonneux and E. Courtens, Phys. Rev. B 46, 556 (1992).
[12] M. Stampanoni, Appl. Phys. A 49, 449 (1989).
[13] W. A. A. Macedo and W. Keune, Phys. Rev. Lett. 61, 475 (1988).
[14] D. Pescia, M. Stampanoni, G. L. Bona, A. Vaterlaus, R. F. Willis, and F. Meier, Phys. Rev. Lett. 58, 2126 (1987).
[15] D. A. Steigerwald and W. F. Egelhoff, Jr., Surface Science 192, L887 (1987).
[16] M. Onellion, M. A. Thompson, J. L. Erskine, C. B. Duke, and A. Paton, Surface Science 179, 219 (1987).
[17] W. Daum, C. Stuhlmann, and H. Ibach, Phys. Rev. Lett. 60, 2741 (1988).
[18] C. Argile and G. E. Rhead, Surface Science Reports 10, 277 (1989).
[19] J. Thomassen, B. Feldmann, and M. Wuttig, Surface Science 264, 406 (1992).
[20] D. A. Steigerwald, I. Jacob, and W. F. Egelhoff, Jr., Surface Science 202, 472 (1988).
[21] Y. Darici, J. Marcano, H. Min, and P. A. Montano, Surface Science 217, 521 (1989).
[22] S. A. Chambers, T. J. Wagener, and J. H. Weaver, Phys. Rev. B 36, 8992 (1987).
[23] H. Glatzel, T. Fauster, B. M. U. Scherzer, and V. Dose, Surface Science 254, 58 (1991).
[24] A. Brodde and H. Neddermayer, Ultramicroscopy 42–44, 556 (1991).
[25] C. Argile and G. E. Rhead, Surface Science 53, 659 (1975).
[26] T. B. Massalski, *Binary Alloy Phase Diagrams* (ASM International, Metals Part, OH, 1990), Vol. 2.
[27] S. H. Lu, J. Quinn, D. Tian, F. Jona, and P. M. Marcus, Surface Science 209, 364 (1989).
[28] H. Landskron, G. Schmidt, K. Heinz, K. Müller, C. Stuhlmann, U. Beckers, M. Wuttig, and H. Ibach, Surface Science 256, 115 (1991).
[29] H. Magnan, D. Chandesris, B. Villette, O. Heckmann, and J. Lecante, Phys. Rev. Lett. 67, 859 (1991).
[30] A. Clarke, P. J. Rous, M. Arnott, G. Jennings, and R. F. Willis, Surface Science 192, L843 (1987).
[31] M. R. Scheinfein, J. S. Drucker, G. G. Hembree, S. D. Healy, K. R. Heim, and Z. J. Yang (to be published).
[32] S. D. Healy, K. R. Heim, Z. J. Yang, J. S. Drucker, G. G. Hembree, and M. R. Scheinfein (to be published).
[33] Z. J. Yang, S. D. Healy, K. R. Heim, J. S. Drucker, G. G. Hembree, and M. R. Scheinfein (to be published).
[34] M. Stampanoni and R. Allenspach, J. Magn. Magn. Mater. 104–107, 1805 (1992).
[35] G. Hembree, J. Drucker, L. Hong, M. Krishnamurthy, and J. A. Venables, Appl. Phys. Lett. 58, (1991).
[36] G. G. Hembree and J. A. Venables, Ultramicroscopy 47, 109 (1992); J. Liu, G. G. Hembree, G. E. Spinnler, and J. A. Venables, Surface Science Lett. 262, L111 (1992); J. Liu, G. G. Hembree, G. E. Spinnler, and J. A. Venables, Catalysis Lett. 15, 133 (1992).
[37] M. Krishnamurthy, J. Drucker, and J. Venables, J. Appl. Phys. 69, 6461 (1991).
[38] J. Drucker, M. Krishnamurthy, and G. Hembree, Ultramicroscopy 35, 323 (1991).
[39] G. G. Hembree, P. A. Crozier, J. S. Drucker, M. Krishnamurthy, J. A. Venables, and J. M. Cowley, Ultramicroscopy 31, 111 (1989).
[40] J. A. Venables, J. M. Cowley, and H. S. von Harrach, Inst. Phys. Conf. Ser. 90, 85 (1987).
[41] P. Kruit and J. A. Venables, Ultramicroscopy 25, 183 (1988); P. Kruit, Adv. Opt. Electron Microsc. 12, 93 (1991).
[42] M. R. Scheinfein (unpublished).

[43] Crystals were custom fabricated by Virgil Straughn, Monocrystals Inc. Cleveland, OH.
[44] J. Drucker, J. Appl. Phys. 70, 2806 (1991).
[45] J. A. Venables, D. R. Batchelor, M. Hanbücken, C. J. Harland, and G. W. Jones, Philos. Trans. R. Soc. London A 318, 243 (1986).
[46] F. Grønlund and P. E. H. Nielsen, Surface Science 30, 388 (1972).
[47] G. W. Goetze, A. H. Boerio, and M. Green, J. Appl. Phys. 35, 482 (1964); G. W. Goetze, Adv. Electron. Electron Phys. 22, 219 (1968).
[48] Puratronic grade Fe was purchased from AESAR Johnson Matthey.
[49] S. Ossicini, R. Memeo, and F. Ciccacci, J. Vac. Sci. Technol. 3, 387 (1985).
[50] S. Tanuma, C. J. Powell, and D. R. Penn, J. Electron Spectrosc. Rel. Phenomena 52, 285 (1990).
[51] S. D. Bader, J. Magn. Magn. Mater. 100, 440 (1991); M. J. Freiser, IEEE Trans. Magn. 4, 152 (1968); P. Q. J. Nederpel and J. W. D. Martens, Rev. Sci. Instrum. 56, 687 (1985); S. N. Jasperson and S. E. Schnatterly, *ibid.* 40, 761 (1969); 41, 152 (1970) (Erratum).
[52] The lattice constant for bcc Fe is 20% smaller than that of fcc Fe. A 45° rotation resulting during bcc growth would produce an increase greater than 12% for the low index (⟨100⟩ and ⟨110⟩), in-plane lattice parameters.
[53] G. L. Krasko, Solid State Commun. 70, 1099 (1989).
[54] V. L. Moruzzi, P. M. Marcus, and J. Kübler, Phys. Rev. B 39, 6957 (1989).
[55] U. Gradmann, J. Magn. Magn. Mater. 100, 481 (1991).

Combined three-axis surface magneto-optical Kerr effects in the study of surface and ultrathin-film magnetism

Z. J. Yang and M. R. Scheinfein
Department of Physics and Astronomy, Arizona State University, Tempe, Arizona 85287-1504

(Received 21 July 1993; accepted for publication 17 August 1993)

Surface and ultrathin-film magnetocrystalline anisotropy in epitaxial fcc Fe thin films grown on room-temperature Cu(100) single crystals has been investigated, *in situ*, by the combined surface magneto-optical Kerr effects (SMOKE). In polar, longitudinal, and transverse Kerr effects, the direction of the applied magnetic field must be distinguished from the direction of magnetization during the switching process. For arbitrary orientations of the magnetization and field axis relative to the optical scattering plane, any of the three Kerr effects may contribute to the detected signal. A general expression for the normalized light intensity sensed by a photodiode detector, involving all three combined Kerr effects, is obtained both in the ultrathin-film limit and for bulk, at general oblique incidence angles and with different orientations of the polarizer, modulator, and analyzer. This expression is used to interpret the results of fcc/Fe/Cu(100) SMOKE measurements. For films grown at room temperature, polar and longitudinal Kerr-effect magnetization loops show that the easy axis of magnetization rotates from the (canted) out-of-plane direction to the in-plane direction at a thickness of about 4.7 monolayers. Transverse Kerr-effect measurements indicate that the in-plane easy axes are biaxial.

I. INTRODUCTION

The surface magneto-optical Kerr effect (SMOKE), based on the conventional magneto-optical Kerr effect (MOKE), has become an important probe in the study of surface and ultrathin-film magnetism. The main advantage of SMOKE over conventional methods in obtaining thin-film magnetization hysteresis loops is its ease in implementation for *in situ* magnetic property characterization. Although most implementations of SMOKE are limited to qualitative information (absolute magnetization calibration is difficult), SMOKE has been successfully applied to a variety of materials and thin-film systems. For example, the longitudinal and polar Kerr effects have been employed to study the dependence of the magnetic properties on temperature, growth conditions, and film thickness of bcc Fe and fcc Fe single-crystal thin films on Au(100) and Cu(100) (see, e.g., Refs. 1–4). Longitudinal and transverse Kerr effects have been used to detect two in-plane orthogonal magnetization components in single-crystal Fe/GaAs(100) and Fe/GaAs(110) thin films.[5,6] SMOKE has also found widespread application in the study of antiferromagnetic and ferromagnetic coupling in the giant magnetoresistance (GMR) systems (see, e.g., Refs. 7 and 8).

Optical effects which exhibit the influence of a magnetic field on the emission of light by a source, or on the propagation of light in matter placed in the field, are referred to as magneto-optical effects. Two basic magneto-optic phenomena are usually distinguished, the Faraday effect, and the Kerr effect. The Faraday effect is usually understood to consist of the rotation of the plane of polarization and the change in the ellipticity when an initially linearly polarized beam of light is propagated through a magnetized medium. The Kerr effect[9] is characterized by a change in the state of polarization of polarized light reflected from a surface of a magnetized medium. Three magneto-optical Kerr effects (polar, longitudinal, and transverse) are classified according to the plane of the incidence of the scattered light. Experimental studies of magneto-optical effects (both Faraday and Kerr effects) have shown that the rotation of the polarization vector and the ellipticity are proportional, for a given temperature and (light) frequency, to the direction of magnetization of ferromagnetic specimens.[10] A phenomenological theory of the polar, longitudinal, and transverse Kerr magneto-optical effects in ferromagnets was originally developed by Voigt in 1908.[11] A more complete theory including derivations of the Fresnel coefficients were given by Argyres,[12] Robinson,[13] Metzger, Pluvinage, and Torguet,[14] and Hunt.[15] Since the Kerr rotation is proportional to the magnetization[16] (surface magnetization sensitivity is due to the near 10 nm extinction lengths for optical radiation in metals), magneto-optical methods have been used to study the magnetic behavior of magnetic materials. These include imaging ferromagnetic (ferrimagnetic) domains using polar and longitudinal Kerr effects;[17] determining absolute saturation magnetization from optical measurements;[16] and extracting magnetization loops from thin films (MOKE)[18–22] and *in situ* (as-grown) ultrathin films (SMOKE);[1,23–25] as well as exploring new magneto-optical phenomena of magnetic materials.[26] Applications of the Kerr effect include the development of magneto-optical recording, a high-density data storage technology.[27]

In analyzing experiments employing polar, longitudinal, and transverse Kerr effects, the direction of the applied magnetic field must be distinguished from the direction of magnetization during the switching process. Since the Kerr effect exists for any arbitrary direction of the magnetization (relative to the scattering plane), for non-normal in-

 0021-8979/93/74(11)/1/14/$6.00

cidence, magnetization loops obtained from any of the three Kerr effects may contribute to the detected signal. Here, we distinguish a pure Kerr effect from the general Kerr effect by analyzing the sensitivity of the detected signals to various magnetization components in the sample to be analyzed. A pure Kerr effect experiment may, for example, employ normally incident polarized light, and normally applied magnetic fields to detect only the perpendicular component of the magnetization; the pure polar Kerr effect. However, at non-normal incidence with different relative orientations of the three basic optical devices (polarizer, modulator, and analyzer) in the SMOKE system, we show that either all three magnetization components or any one of them can be detected. Thin-film anisotropies and switching modes can be studied by comparing these three combined Kerr-effect magnetization loops. A derivation of the normalized light intensity sensed by a photodiode detector from the three combined Kerr effects, both in the ultrathin-film limit and from a bulk surface, at general oblique incidence, and with different orientations of the polarizer, modulator, and analyzer, is given in Sec. II. These expressions are shown to reduce to the simple case where no longitudinal Kerr effect is detected at normal incidence. In this case, the detectivity of the polar Kerr effect reaches a maximum.[15] In Sec. III we show results from studies of epitaxial fcc Fe thin films grown at room temperature on Cu(100) single crystals in the preparation chamber of a UHV scanning transmission electron microscope (STEM). This preparation chamber is equipped with standard surface characterization and film-growth instrumentation including an ion sputtering gun, a broad-beam Auger electron spectrometer, an electron gun and reflection high-energy electron diffraction (RHEED) screen, an annealing stage ($T \lesssim 800$ °C), and several electron beam and Knudsen cell evaporators, and is described in detail elsewhere.[28] We employ the expressions obtained in Sec. II to interpret the results of our fcc Fe/Cu(100) SMOKE measurements. For films grown at room temperature, our polar and longitudinal Kerr-effect magnetization loops show that the easy axis of magnetization rotates from the (canted) out-of-plane direction to the in-plane direction at a thickness of about 4.7 ML (monolayer). Transverse Kerr-effect measurements indicate that the in-plane easy axes are biaxial and along the ⟨100⟩ directions.

II. THREE-AXIS SMOKE TRANSFER MATRICES

The measurement scheme of SMOKE is typically the same as in conventional MOKE experiments. The distinguishing difference between MOKE and SMOKE is the transfer matrix of the optically active medium.[23,24] In SMOKE, in the ultrathin-film limit, transmission through and reflection from the underlying substrate must be considered. We will derive the optical transfer matrices for the polarized light scattering experiment shown in Fig. 1(a) for arbitrary polarizer, modulator and analyzer orientations. The components of the SMOKE system include a polarized He-Ne intensity-stabilized laser ($\lambda=632.8$ nm, $\Delta I/I_0=0.1\%$), two Glan–Thompson polarizers (field of view $\sim 30°$, resolution $\sim 0°5'$), a fused-silica head photoelastic modulator ($f=50$ kHz, 170–2600 nm transmission) with antireflective coatings optimized for He-Ne light, and a photodiode detector. The plane of incidence, which includes the sample normal, and both the incident and reflected light rays, define the coordinate system for the SMOKE apparatus. Here, the p axis lies in the scattering plane, and the s axis is perpendicular to the scattering plane. As shown in Fig. 1(a), the angles of polarizer, the principle axis of the modulator, and analyzer relative to the scattering plane (p axis) are θ_p, θ_m, and θ_a, respectively.

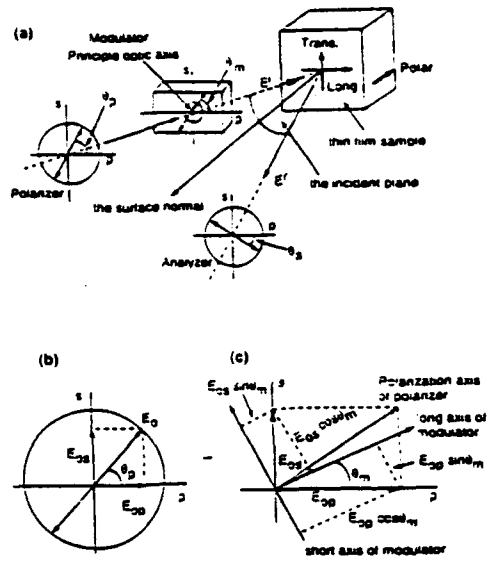

FIG. 1. (a) A schematic diagram showing the Kerr measurement arrangement. The polarizer, modulator,and analyzer angles are θ_p, θ_m, and θ_a, respectively, relative to the scattering plane. The longitudinal, transverse, and polar Kerr effect directions are also shown. (b) The perpendicular and parallel polarization components. (c) The polarization components projected along the modulator axes.

The complex electric field for the linearly polarized light can be expressed in the standard way as $E=E_0\exp[i(\mathbf{k}_0\cdot\mathbf{r}-\omega_0 t)]$ where $k_0=(\omega_0/c)n_0=(\omega_0/c)\sqrt{\epsilon_0\mu_0}$. This beam has two components after transmission through the polarizer, $E_{0s}=E_0\sin\theta_p$, and $E_{0p}=E_0\cos\theta_p$, schematically shown in Fig. 1(b). Following the standard nomenclature, E_{0s} is the component of the electric field perpendicular to the plane of incidence and E_{0p} is the component of the electric field parallel to the plane of incidence. Assume that the retardation angle of the modulator is $\varphi=\varphi_0\exp(i\omega t)$ (we will let $\varphi=\varphi_0\sin\omega t$ later). Figure 1(c) shows the projections of the plane polarized light from the polarizer axis onto the modulator axis. The component of the electric field projected along the principle optic axis (the long axis) of the modulator is

$$(E_{op}\cos\theta_m+E_{os}\sin\theta_m)\exp(-i\varphi),$$

whereas the component along the short modulator axis is $(E_{os}\cos\theta_m-E_{op}\sin\theta_m)$. Since we are interested in the electric field relative to the scattering plane, we express the modulator transfer function for an arbitrary modulator angle θ_m as a 2×2 matrix M_0, as follows:

$$M_0=\begin{pmatrix}\cos\frac{\varphi}{2}-i\sin\frac{\varphi}{2}\cos(2\theta_m) & -i\sin\frac{\varphi}{2}\sin(2\theta_m)\\ -i\sin\frac{\varphi}{2}\sin(2\theta_m) & \cos\frac{\varphi}{2}+i\sin\frac{\varphi}{2}\cos(2\theta_m)\end{pmatrix}, \tag{1}$$

where

$$\begin{pmatrix}E_p\\E_s\end{pmatrix}^i=M_0\begin{pmatrix}E_{op}\\E_{os}\end{pmatrix}. \tag{2}$$

Here the superscript i refers to the incident beam on the sample. For some special values of the modulator angle θ_m, the matrix M_0 can be simplified as follows:

$$M_0(\theta_m=0)=\begin{pmatrix}e^{-i(\varphi/2)} & 0\\ 0 & e^{i(\varphi/2)}\end{pmatrix},$$

$$M_0\left(\theta_m=\frac{\pi}{2}\right)=\begin{pmatrix}e^{i(\varphi/2)} & 0\\ 0 & e^{-i(\varphi/2)}\end{pmatrix} \tag{3}$$

$$M_0\left(\theta_m=\frac{\pi}{4}\right)=\begin{pmatrix}\cos(\varphi/2) & -i\sin(\varphi/2)\\ -i\sin(\varphi/2) & \cos(\varphi/2)\end{pmatrix}.$$

These are three most common cases applied in MOKE and SMOKE.

In terms of the well-known (bulk) Fresnel reflection matrix $\Re$, the amplitude of the reflection from the sample can be expressed in matrix notation

$$\begin{pmatrix}E_p\\E_s\end{pmatrix}^r=\Re\begin{pmatrix}E_p\\E_s\end{pmatrix}^i, \tag{4}$$

where superscripts i and r denote the incident (positive traveling) and the reflected (negative traveling) waves at boundary of media, and the subscripts p and s denote electric field components parallel (p) and perpendicular (s) to the plane of incidence. The reflected electric field received by the detector is then given by $E_T=E_p^r\cos\theta_a+E_s^r\sin\theta_a$, where θ_a is the angle of the analyzer. The normalized intensity detected by the photodiode is $I=|E_T|^2/|E_0|^2$. Expressions for the normalized intensity depend on the orientations of three main optic devices (the angles θ_p, θ_m, and θ_a) and the bulk Fresnel reflection matrix $\Re$. We briefly describe the components of the Fresnel reflection coefficients, derived from a phenomenological model of the bulk Kerr effect,[12–15] for two media separated by a single boundary. We generalize these results in the ultrathin-film limit for three media with two boundaries.

In general, the applied magnetic-field axes and the obliquely incident electric-field components E_s^i and E_p^i may not coincide with the principle magnetization axes in the reference plane of the sample. In order to describe the scattering matrices, we must relate the components of the magnetization axes of the sample with the applied field direction for some arbitrarily oriented scattering plane. Figure 2 shows two coordinate systems, the (xyz) system referenced to the directions of the applied magnetic field H, H_x, H_y, and H_z, and the ($x''y''z''$) system referenced to the principle axes of the magnetic sample. Here we take the applied magnetic-field directions relative to the scattering

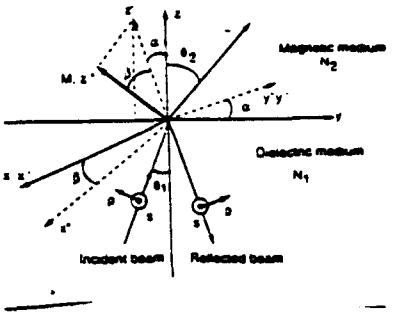

FIG. 2. The coordinate transformation from the ($x''y''z''$) system of the magnetization to the (xyz) system of the scattering geometry is accomplished through two Euler angle rotations, α and β. The intermediate coordinate system rotated about the x axis by α is ($x'y'z'$). The second rotation β is about the new axis y'.

plane such that H_y is in the plane of incidence and in the plane of the film, H_x is perpendicular to the plane of incidence and in the plane of the film, and H_z is in the plane of incidence and perpendicular to the film surface. Assume that the magnetization M and the dielectric permittivity and magnetic permeability tensors are defined in ($x''y''z''$). In our geometry, the y-z plane lies in the plane of incidence, while the x-y plane is parallel to the sample surface. When only linear terms are retained in the complex magneto-optic constant Q, the dielectric permittivity and magnetic permeability tensors in the double-primed coordinate system, ϵ'' and μ'', are given by ($M_z''=M_{\rm sat}$)

$$\epsilon''=\begin{pmatrix}\epsilon_q & -iQ\epsilon_q & 0\\ iQ\epsilon_q & \epsilon_q & 0\\ 0 & 0 & \epsilon_q\end{pmatrix},$$

$$\mu''=\begin{pmatrix}\mu_q & -iP\mu_q & 0\\ iP\mu_q & \mu_q & 0\\ 0 & 0 & \mu_q\end{pmatrix}, \tag{5}$$

where ϵ_q (μ_q) is effectively independent of the direction of the magnetization M, and Q (P), the complex magneto-optical constant, can be written in polar form as $Q=Q_0e^{-iq}$. The magnitude Q_0 is proportional to the magnetization M (odd function of M), and q is the phase. The value for Q, given by Voigt[11] for Fe bulk saturation magnetization M_s, is $Q=0.0215e^{(-i0.073)}$. Since the real part of Q is only on the order of a few thousandths (even smaller for ultrathin films) and the imaginary part is negligible, the assumption of retaining terms to first order in Q is valid. In our treatment of the general Kerr effect, the magneto-optical constant Q will have a specific value for any given magnetic system, while the Kerr effect signal will be proportional to a magnetization component (direction cosines where m_x, m_y, and m_z take values between positive and negative one) along a given direction. This is to be contrasted with the usual derivation for the pure Kerr effect where the magneto-optical constant is a linear funtion of a particular component of the magnetization. Although these two cases are essentially identical, expressions for the pure Kerr effect assume a linear dependence of Q upon M.

The coordinate transformation between the applied field direction and the sample magnetization axes necessary to derive expressions for the general Kerr effect is given by

$$\begin{pmatrix} x \\ y \\ z \end{pmatrix} = A \begin{pmatrix} x'' \\ y'' \\ z'' \end{pmatrix}$$

$$= \begin{pmatrix} \cos\beta & 0 & \sin\beta \\ \sin\alpha\sin\beta & \cos\alpha & -\sin\alpha\cos\beta \\ -\cos\alpha\sin\beta & \sin\alpha & \cos\alpha\cos\beta \end{pmatrix} \begin{pmatrix} x'' \\ y'' \\ z'' \end{pmatrix}. \tag{6}$$

The permittivity tensor, transformed into the (xyz) system from $(x''y''z'')$ for an arbitrary orientation of magnetization M, can be written as follows. Here the direction dependence for each individual Kerr effect is given explicitly:

$$\epsilon = A\epsilon'' A^{-1}$$

$$= m_x^2 \epsilon^x[\epsilon_q, Q/m_x] + m_y^2 \epsilon^y[\epsilon_q, Q/m_y] + m_z^2 \epsilon^z[\epsilon_q, Q/m_z]$$

$$= \begin{bmatrix} \epsilon_q & -i\epsilon_q Q m_z & i\epsilon_q Q m_y \\ i\epsilon_q Q m_z & \epsilon_q & -i\epsilon_q Q m_x \\ -i\epsilon_q Q m_y & i\epsilon_q Q m_x & \epsilon_q \end{bmatrix}. \tag{7}$$

Thus, by factoring out the square of a magnetization component and letting the pure Kerr effect magneto-optical constant be replaced by Q/m, the direction-specific dielectric tensors are

$$\epsilon^x = \epsilon^t = \begin{pmatrix} \epsilon_q & 0 & 0 \\ 0 & \epsilon_q & -Q\epsilon_q \\ 0 & iQ\epsilon_q & \epsilon_q \end{pmatrix}, \tag{8}$$

$$\epsilon^y = \epsilon^l = \begin{pmatrix} \epsilon_q & 0 & iQ\epsilon_q \\ 0 & \epsilon_q & 0 \\ -iQ\epsilon_q & 0 & \epsilon_q \end{pmatrix}, \tag{9}$$

$$\epsilon^z = \epsilon^p = \begin{pmatrix} \epsilon_q & -iQ\epsilon_q & 0 \\ iQ\epsilon_q & \epsilon_q & 0 \\ 0 & 0 & \epsilon_q \end{pmatrix}. \tag{10}$$

$\epsilon^x(\epsilon^t)$, $\epsilon^y(\epsilon^l)$, and $\epsilon^z(\epsilon^p)$ are the permittivity tensors for the transverse, longitudinal, and polar effects, respectively. The direction cosines of the magnetization axes along the applied field direction (projection of M onto H) in Eq. (7) are given explicitly by $m_t = m_x = M_x/M = \sin\beta$; $m_l = m_y = M_y/M = -\sin\alpha\cos\beta$; and $m_p = m_z = M_z/M = \cos\alpha\cos\beta$. M_x, M_y, and M_z are components of magnetization in the (xyz) system which, respectively, cause the transverse, longitudinal, and polar magneto-optical Kerr effects. M is the magnetization of the film at whatever field H is applied. The magnitude of M will equal the spontaneous magnetization M_s for single-domain samples or for multiple-domain samples when the applied field H reaches the saturation field H_s. The surface magnetization (thin surface layer) from which the reflection of light takes place gives rise to the SMOKE signal.

The combined magneto-optical (bulk) Kerr-effect Fresnel reflection matrix $\mathfrak{R}$, to first order in Q, can be expressed in the transformed coordinate system as follows:

$$\mathfrak{R} = m_x^2 r^x[Q/m_x] + m_y^2 r^y[Q/m_y] + m_z^2 r^z[Q/m_z]$$

$$= \begin{pmatrix} \tilde{r}_{pp} & \tilde{r}_{ps} \\ \tilde{r}_{sp} & \tilde{r}_{ss} \end{pmatrix}. \tag{11}$$

The square brackets mean replace Q by Q/m in the expressions for the dielectric tensors. The combined magneto-optical Kerr-effect reflection coefficients[14] can be written in the form (total) given in Eq. (12). We use standard notation in that subscripts denote the scattering plane dependence of the matrix elements (i.e., r_{ps} couples the incident s-polarized electric-field component, upon reflection into a p-polarized electric-field component). Superscripts on the Fresnel coefficients are used to differentiate among the longitudinal l, polar p, and transverse t Kerr effects:

$$\tilde{r}_{pp} = \frac{\mu_1 N_2 \cos\theta_1 - \mu_2 N_1 \cos\theta_2}{\mu_1 N_2 \cos\theta_1 + \mu_2 N_1 \cos\theta_2} + \frac{2i\mu_1\mu_2 N_1 N_2 \cos\theta_1 \sin\theta_2 m_x Q}{\mu_1 N_2 \cos\theta_1 + \mu_2 N_1 \cos\theta_2},$$

$$\tilde{r}_{ps} = -\frac{i\mu_1\mu_2 N_1 N_2 \cos\theta_1 (m_y \sin\theta_2 + m_z \cos\theta_2) Q}{(\mu_1 N_2 \cos\theta_1 + \mu_2 N_1 \cos\theta_2)(\mu_2 N_1 \cos\theta_1 + \mu_1 N_2 \cos\theta_2)\cos\theta_2},$$

$$\tilde{r}_{ss} = \frac{\mu_2 N_1 \cos\theta_1 - \mu_1 N_2 \cos\theta_2}{\mu_2 N_1 \cos\theta_1 + \mu_1 N_2 \cos\theta_2}, \tag{12}$$

$$\tilde{r}_{sp} = \frac{i\mu_1\mu_2 N_1 N_2 \cos\theta_1 (m_y \sin\theta_2 - m_z \cos\theta_2) Q}{(\mu_1 N_2 \cos\theta_1 + \mu_2 N_1 \cos\theta_2)(\mu_2 N_1 \cos\theta_1 + \mu_1 N_2 \cos\theta_2)\cos\theta_2}.$$

μ_1 and μ_2 are the permeabilites of media 1 and 2 (see Fig. 2), N_1 and N_2 are the complex indices of refraction of the media, and θ_1 and θ_2 are the incident and refracted angles, respectively. $r^x(r^t)$, $r^y(r^l)$, and $r^z(r^p)$ are the pure (bulk) Fresnel reflection matrices for transverse, longitudinal, and polar magneto-optical Kerr effects, respectively, which are defined as

$$r^x = r^t = \begin{pmatrix} \tilde{r}_{pp} & \tilde{r}_{ps} \\ \tilde{r}_{sp} & \tilde{r}_{ss} \end{pmatrix} \quad r^y = r^l = \begin{pmatrix} \tilde{r}_{pp} & \tilde{r}_{ps} \\ \tilde{r}_{sp} & \tilde{r}_{ss} \end{pmatrix} \quad r^z = r^p = \begin{pmatrix} \tilde{r}_{pp} & \tilde{r}_{ps} \\ \tilde{r}_{sp} & \tilde{r}_{ss} \end{pmatrix}. \tag{13}$$

The pure (bulk) Fresnel reflection coefficients for each individual Kerr effect can be extracted from Eqs. (11) and (12) are given below for completeness.[13,15] The (bulk) polar magneto-optical Kerr-effect Fresnel coefficients, where variables with overstriked tildes are complex, variables without tildes are real, and the real phase shift δ, are

$$\tilde{r}_{pp}=r^{p}_{pp}\exp(i\delta^{p}_{pp})=\frac{\mu_1 N_2\cos\theta_1-\mu_2 N_1\cos\theta_2}{\mu_1 N_2\cos\theta_1+\mu_2 N_1\cos\theta_2},$$

$$\tilde{r}_{ss}=r^{p}_{ss}\exp(i\delta^{p}_{ss})=\frac{\mu_2 N_1\cos\theta_1-\mu_1 N_2\cos\theta_2}{\mu_2 N_1\cos\theta_1+\mu_1 N_2\cos\theta_2}, \tag{14}$$

$$\tilde{r}_{sp}=\tilde{r}_{ps}=r^{p}_{sp}\exp(i\delta^{p}_{sp})=-\frac{i\mu_1\mu_2 N_1 N_2\cos\theta_1 Q}{(\mu_2 N_1\cos\theta_1+\mu_1 N_2\cos\theta_2)(\mu_1 N_2\cos\theta_1+\mu_2 N_1\cos\theta_2)}.$$

The (bulk) longitudinal Kerr-effect Fresnel coefficients are

$$\tilde{r}^{l}_{pp}=\tilde{r}_{pp}=r^{p}_{pp}\exp(i\delta^{p}_{pp})=\frac{\mu_1 N_2\cos\theta_1-\mu_2 N_1\cos\theta_2}{\mu_1 N_2\cos\theta_1+\mu_2 N_1\cos\theta_2},$$

$$\tilde{r}^{l}_{ss}=\tilde{r}_{ss}=r^{p}_{ss}\exp(i\delta^{p}_{ss})=\frac{\mu_2 N_1\cos\theta_1-\mu_1 N_2\cos\theta_2}{\mu_2 N_1\cos\theta_1+\mu_1 N_2\cos\theta_2}, \tag{15}$$

$$\tilde{r}^{l}_{sp}=-\tilde{r}^{l}_{ps}=r^{l}_{sp}\exp(i\delta^{l}_{sp})=-\frac{i\mu_1\mu_2 N_1 N_2\cos\theta_1\sin\theta_2 Q}{(\mu_2 N_1\cos\theta_1+\mu_1 N_2\cos\theta_2)(\mu_1 N_2\cos\theta_1+\mu_2 N_1\cos\theta_2)\cos\theta_2}.$$

The (bulk) transverse Kerr-effect Fresnel coefficients are similarly expressed,

$$\tilde{r}^{t}_{pp}=r^{t}_{pp}\exp(i\delta^{t}_{pp})$$
$$=\frac{\mu_1 N_2\cos\theta_1-\mu_2 N_1\cos\theta_2}{\mu_1 N_2\cos\theta_1+\mu_2 N_1\cos\theta_2}$$
$$+i\frac{2\mu_1\mu_2 N_1 N_2\cos\theta_1\sin\theta_2 Q}{(\mu_1 N_2\cos\theta_1+\mu_2 N_1\cos\theta_2)^2},$$

$$\tilde{r}^{t}_{ss}=\tilde{r}_{ss}=r^{p}_{ss}\exp(i\delta^{p}_{ss})=\frac{\mu_2 N_1\cos\theta_1-\mu_1 N_2\cos\theta_2}{\mu_2 N_1\cos\theta_1+\mu_1 N_2\cos\theta_2}, \tag{16}$$

$$\tilde{r}^{t}_{sp}=\tilde{r}^{t}_{ps}=0.$$

The (complex) refractive index in the optically active medium is defined as $N=N_r-iN_i$. $\sin\theta_2$ and $\cos\theta_2$ are complex numbers determined by the Snell–Descartes law: $N_1\sin\theta_1=N_2\sin\theta_2$; $\cos^2\theta_2+\sin^2\theta_2=1$; and $\mathrm{Re}(N_2\cos\theta_2)>0$. The conditions in Eq. (12) for single-axis pure polar, longitudinal, and transverse effects are: (i) polar: $m_x=m_y=0$ and $m_z=1$; (ii) longitudinal: $m_x=m_z=0$ and $m_y=1$; and (iii) transverse: $m_z=m_y=0$ and $m_x=1$, and for the pure Kerr effect, Q is proportional to that particular component of m under observation.

The Kerr rotation θ_k and ellipticity η_k (for an individual or combined Kerr effect) are defined from the Fresnel coefficients as follows:

$$\theta_{ks}=-\mathrm{Re}(\tilde{r}_{ps}/\tilde{r}_{ss}),$$

$$\theta_{kp}=\mathrm{Re}(\tilde{r}_{sp}/\tilde{r}_{pp}) \tag{17}$$

$$\eta_{ks}=\mathrm{Im}(\tilde{r}_{ps}/\tilde{r}_{ss})\mathrm{Re}(\tilde{r}_{ps}/\tilde{r}_{ss}),$$

$$\eta_{kp}=\mathrm{Im}(\tilde{r}_{sp}/\tilde{r}_{pp})/\mathrm{Re}(\tilde{r}_{sp}/\tilde{r}_{pp}).$$

If we let $\mu_{(1,2)}=1$ in the expressions for the Fresnel coefficients [Eqs. (11)–(16)], we obtain the standard equations characterizing magneto-optical phenomena in the optical region. In the intermediate frequency region where μ_i may differ from one, Q [Eqs. (11)–(16)] should be replaced by $Q^*=Q+P$ to include gyromagnetic effects.

A thin-film system composed of two dielectric layers and one optically active (magnetic) layer with two boundaries is shown in Fig. 3.[13,15,24] For absorbing films, there can be considerable changes in the relative intensity of the interfering polarized beams. This interference is a function of film thickness as a result of the Faraday effect. A general theory of the dependence of the magneto-optical Kerr effect on the thickness (and the associated dependence of the optical constants Q and P) has been given by Noskov and Sokolov.[28] Explicit expressions of the combined magneto-optical Kerr-effect Fresnel reflection coefficients at oblique incidence for general multiple-film structures are very unwieldy, even to first order in Q. However, when the film thickness exceeds the attenuation length (depth), the ex-

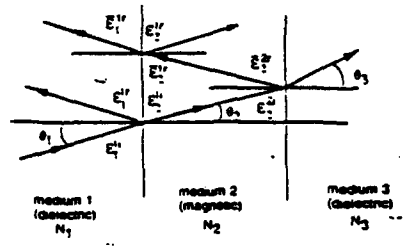

FIG. 3. The scattering geometry for the thin-film surface magneto-optical Kerr effect incorporates the interference between the primary reflected waves and the secondary reflected waves. The electric fields resulting from the secondary boundary are denoted with an overstrike bar. Each individual reflection and transmission matrix is defined in Appendix A.

pressions simplify to those given above (bulk Kerr effect). In the other limit, when the film becomes extremely thin, the Faraday effect for transmitted beams reflected from the substrate, and their interference, may become important. Further complications arise from the right- and left-hand-side-rotating waves, in both the positive and negative propagation directions in the optically active medium, due to the dependence of the refractive index on the direction of the magnetic field relative to the propagation direction.[13] In this case, the refractive index becomes $N_{\pm} \cong N_2[1 \mp \frac{1}{2}(Q+P)m_z]$. Here, in order to illucidate the modification of the bulk Fresnel coefficients in the thin-film limit,[15,24] we confine our attention to the simple case of two interfering beams, and once again we neglect terms second order and higher in Q.

As indicated in Fig. 3, the total reflected field E_1^{lr} at boundary 1 for the two-beam case becomes

$$\begin{aligned} E_1^{lr} &= \epsilon_1^{lr} + \bar{\epsilon}_1^{lr} \\ &= \Re \epsilon_1^{li} + \bar{t}_{21} T \bar{\epsilon}_2^{2r} \\ &= (\Re + \bar{t}_{21} T r_{23} T t_{12}) \epsilon_1^{li} \\ &= (\Re + \Re') \epsilon_1^{li} \\ &= \Re_{tf} \epsilon_1^{li}. \end{aligned} \tag{18}$$

A bar over these electric-field components indicates the interfering beam reflected from the second boundary, and the superscript 1 (2) refers to electric-field components at the first (second) boundary. Explicit definitions and expressions for the reflection matrices r and the transmission matrices t are given in Appendix A. The thin-film transmission matrix T is given[13,15,23] by

$$T = \begin{pmatrix} \cos\psi_2 \exp(i\phi_2) & \sin\psi_2 \exp(i\phi_2) \\ -\sin\psi_2 \exp(i\phi_2) & \cos\psi_2 \exp(i\phi_2) \end{pmatrix}. \tag{19}$$

The phase-retardation parameter ϕ_2, which is same for all three SMOKE effects in the optically active medium (medium 2 shown in Fig. 3), is $\phi_2 = (2\pi N_2 d_2 \cos\theta_2/\lambda_0)$. The Faraday rotation angle ψ_2 is different for each Kerr effect: (i) polar: $\psi_2^p = \pi d_2 N_2 Q/\lambda_0$; (ii) longitudinal: $\psi_2^l = \pi d_2 N_2 \tan\theta_2 Q/\lambda_0$; and (iii) transverse: $\psi_2^t = 0$. d_2 is the thickness of the optically active magnetic medium and λ_0 is the free-space wavelength of the incident beam. Retaining only first-order terms in Q, the reflection matrix due to the thin film (part) of the Kerr signal is given below:

$$\Re' = \exp(i2\phi_2) \times \begin{pmatrix} \bar{t}_{pp}\bar{r}_{2pp}t_{pp} & [\bar{t}_{pp}\bar{r}_{2pp}t_{sp} + \bar{t}_{pp}\bar{r}_{2ps}t_{ss} + \bar{t}_{ps}\bar{r}_{2ss}t_{ss} + (\bar{r}_{2pp} + \bar{r}_{2ss})\bar{t}_{pp}t_{ss}\psi_2] \\ [\bar{t}_{ss}\bar{r}_{2ss}t_{sp} + \bar{t}_{ss}\bar{r}_{2sp}t_{pp} + \bar{t}_{sp}\bar{r}_{2pp}t_{pp} - (\bar{r}_{2pp} + \bar{r}_{2ss})\bar{t}_{ss}t_{pp}\psi_2] & \bar{t}_{ss}\bar{r}_{2ss}t_{ss} \end{pmatrix} \tag{20}$$

The matrix $\Re'$ contains all of the effects of the interfering beam reflected from the second boundary, and hence $\Re'$ is termed the secondary reflection matrix. Since this matrix is complex, we can express Eq. (20) as

$$\Re' = \begin{pmatrix} \bar{r}_{pp} & \bar{r}_{ps} \\ \bar{r}_{sp} & \bar{r}_{ss} \end{pmatrix} = \begin{pmatrix} r'_{pp}\exp(i\varphi_{pp}) & r'_{ps}\exp(i\varphi_{ps}) \\ r'_{sp}\exp(i\varphi_{sp}) & r'_{ss}\exp(i\varphi_{ss}) \end{pmatrix}. \tag{21}$$

Upon substituting Eqs (A6)–(A17) from Appendix A into Eq. (21), we observe that for polar and longitudinal Kerr effects that the diagonal terms in matrix $\Re'$, r'_{pp} and r'_{ss}, are independent of Q, while the off-diagonal terms, r'_{ps} and r'_{sp}, are odd functions of Q. For the transverse Kerr effect, only the diagonal term r'_{pp} is a function of Q. Since

$$\begin{aligned} &r_1 \exp(i\varphi_1) + r_2 \exp(i\varphi_2) = r\exp(i\varphi), \\ &r = \sqrt{r_1^2 + r_2^2 + 2r_1 r_2 \cos(\varphi_1 - \varphi_2)}, \\ &\tan\varphi = \frac{r_1 \sin\varphi_1 + r_2 \sin\varphi_2}{r_1\cos\varphi_1 + r_2\cos\varphi_2}, \end{aligned} \tag{22}$$

we can combine the major reflection matrix $\Re$ and the secondary reflection matrix $\Re'$ into the total thin-film reflection matrix $\Re_{tf}$,

$$\Re_{tf} = \Re + \Re' = \begin{pmatrix} \bar{R}_{pp} & \bar{R}_{ps} \\ \bar{R}_{sp} & \bar{R}_{ss} \end{pmatrix}. \tag{23}$$

Although the expression for the total reflection matrix elements are now a function of the magnetic medium thickness (the magneto-optical constant Q also changes with the film thickness until it reaches its bulk value) and the refractive index of the substrate, the dependence of these matrix elements on the magneto-optical constant Q is similar to the matrix $\Re$, for the bulk Kerr effect. The influence of the secondary reflection matrix on the variation of the light intensity with thickness will cause a periodic increase and decrease in the magneto-optical rotation angle when medium 2 is a dielectric and medium 3 is the optically active magnetic material. The magneto-optical rotation as a function of thickness eventually becomes damped and periodicity is sharply modified;[29] however, this modification in the reflectivity due to multiple interfering beams does not preclude the interpretation of SMOKE magnetization loops acquired as a function of the applied magnetic field.

Explicit expressions for the normalized light intensity sensed by a photodiode detector for different orientations of the polarizer, modulator, and analyzer at oblique incidence can now be generated for our experimental configuration. Referring to Fig. 1(a), let both the analyzer and modulator angles be set to zero ($\theta_a = 0$, $\theta_m = 0$). For this special case, the incident electric field is given in Eq. (24),

where the parallel and perpendicular field components are yet to be defined:

$$\begin{pmatrix} E_p \\ E_s \end{pmatrix}^i = \begin{pmatrix} E_{0p}\exp[-i(\varphi/2)] \\ E_{0s}\exp[+i(\varphi/2)] \end{pmatrix}. \tag{24}$$

First consider the case of the combined longitudinal and transverse Kerr effects in which the magnetization vector lies in the film surface, i.e., $m_x^2+m_y^2=1$, and $m_z=0$. The detected intensity becomes (Appendix B)

$$\begin{aligned} I=&\{[(m_t^2 r_{pp}^l)^2+m_l^4(r_{pp}^l)^2+2m_t^2m_l^2r_{pp}^lr_{pp}^l\cos(\delta_{pp}^l-\delta_{ps}^l)]\cos^2\theta_p+m_l^2(r_{ps}^l)^2\sin^2\theta_p\}+2[m_t^2m_lr_{pp}^lr_{ps}^l\cos(\delta_{pp}^l-\delta_{ps}^l)\\ &+m_l^3r_{pp}^lr_{ps}^l\cos(\delta_{pp}^l-\delta_{ps}^l)]\sin\theta_p\cos\theta_p\cos\varphi+2[m_t^2m_lr_{pp}^lr_{ps}^l\sin(\delta_{pp}^l-\delta_{ps}^l)+m_l^3r_{pp}^lr_{ps}^l\sin(\delta_{pp}^l-\delta_{ps}^l)]\sin\theta_p\cos\theta_p\sin\varphi\\ =&B+2C\sin\theta_p\cos\theta_p\cos\varphi+2D\sin\theta_p\cos\theta_p\sin\varphi. \end{aligned} \tag{25}$$

The explicit functional dependence of the Fresnel reflection matrices are given in Eqs. (14)–(16), and the transverse reflection coefficient has the following form: $r_{pp}^l[Q/m_l]$. We now have to convert to a first order in Q expression. The first term B is independent of the retardation angle φ of the modulator. In order to enhance the signal to background, we want to minimize this dc signal by crossing the analyzer and the polarizer. The magneto-optical information is extracted from Eq. (25) by letting $\varphi=\varphi_0\sin\omega t$, expanding $\sin\varphi$ and $\cos\varphi$ in terms of Bessel functions, and retaining only the two lowest-frequency modes of the modulator:

$$\sin\varphi\cong 2J_1(\varphi_0)\sin\omega t$$

and

$$\cos\varphi\cong J_0(\varphi_0)+2J_2(\varphi_0)\sin(2\omega t).$$

For the crossed analyzer and polarizer configuration, θ_p is set very close to 90° (choose $\theta_p\sim 85°$ such that $\sin\theta_p\cong 0.996$ and $\cos\theta_p=0.087$). For 1ω detection, choose the modulator retardation as $\varphi_0=108°$ such that $J_0(\varphi_0)=0$ and $J_1(\varphi_0)=0.582$. The combined longitudinal-transverse Kerr intensity in Eq. (25) reduces to the following expression, to first order in Q, and independent of the transverse Kerr effect (since to first order $r_{pp}^lQ=r_{pp}^lQ$), regardless of the direction of the applied magnetic field:

$$I\cong m_l^2(r_{ps}^l)^2+0.2m_lr_{pp}^lr_{ps}^l\sin(\delta_{pp}^l-\delta_{ps}^l)\sin\omega t. \tag{26}$$

Recalling that $r_{ps}^l\propto Q$ and Q is very small, the second term is almost 10 times larger than the first dc (signal) term. In Eq. (26), the longitudinal magnetization dependence m_l is given explicitly, and Q is a small number (a constant for a given material of given thickness). The key point is that the modulated signal, which is proportional to the magneto-optical constant is an odd function of m_l. Note that the angle of incidence upon the film is explicitly included in each of the Fresnel coefficients for each Kerr effect.

If the direction of the applied field is perpendicular to the film surface, or the magnetization can be in any of the three Cartesian directions (see Fig. 2), then the polar effect needs be taken into account. Similarly, the normalized light intensity of the combined three-axis SMOKE can be expressed approximately as follows:

$$\begin{aligned} I=&m_p^2(r_{ps}^p)^2+m_l^2(r_{ps}^l)^2+2m_pm_lr_{ps}^pr_{ps}^l\cos(\delta_{ps}^p-\delta_{ps}^l)\\ &+0.2r_{pp}^lm_pr_{ps}^p\sin(\delta_{pp}^l-\delta_{ps}^p)\sin\omega t\\ &+0.2r_{pp}^lm_lr_{ps}^l\sin(\delta_{pp}^l-\delta_{ps}^l)\sin\omega t. \end{aligned} \tag{27}$$

The expression for the intensity in Eq. (27) now includes the contributions from both polar and longitudinal Kerr effects. Additionally, the magnitude of the response from the polar Kerr effect is larger than that of the longitudinal Kerr effect. Comparing Eqs. (14) and (15), and taking $\lambda_0=632$ nm and the incident angle of 45° ($N_2=3.02-i4.14$ for an Fe film[13]), we have

$$\tilde{r}_{ps}^p=-\tilde{r}_{ps}^l(N_2\cos\theta_2/N_1\sin\theta_1)\cong -5\tilde{r}_{ps}^le^{-i\theta}.$$

Equation (27) is the most general expression of the normalized light intensity with three combined magneto-optical Kerr effects specified for our SMOKE experiment.

III. EXPERIMENT

The specimen preparation chamber of an UHV scanning transmission electron microscope (STEM),[25] a Vacuum Generators HB501-S, operating at base pressures of 5×10^{-11} mbar, has been equipped with an *in situ* SMOKE characterization system as shown schematically in Fig. 4. Longitudinal, polar, and transverse hysteresis loops were recorded by scattering modulated (polarized), He-Ne (632.8 nm) laser light from magnetic surfaces at an angle of incidence of 45° as previously described. Electromagnets situated *ex situ* produce maximum continuous fields of 1.2 kOe (1.5 kOe) in the polar (in-plane) direction. Nanometer lateral spatial resolution surface microanalysis, using secondary electron or Auger electron spectroscopy and imaging, allows for epitaxial film microstructure to be correlated with magnetic properties.

Single crystal Cu(100) substrates 1 mm thick and 3 mm in diameter were electropolished and introduced into the microscope, cyclically sputtered at 330 °C with 600 eV Ar ions at 45° incident angles, then annealed at 600 °C. Samples were observed in the electron microscope after the surface oxygen concentration had been depleted below minimum detectable limits. Fe films were grown with an electron-beam Fe source on clean room-temperature Cu(100) surfaces with average terrace widths between 25

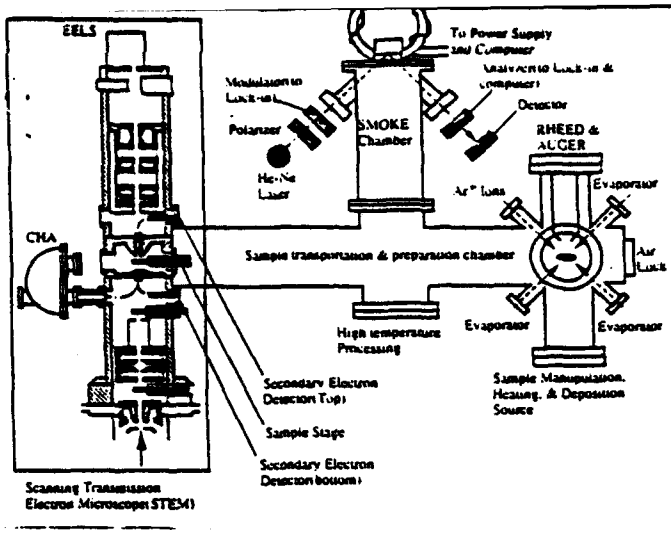

FIG. 4. A schematic of the experimental apparatus used for the characterization of thin film microstructure and magnetic properties. The system is based on an ultrahigh-vacuum scanning transmission electron microscope (left-hand side). The associated in-column analysis is accomplished with high-resolution imaging, electron energy-loss spectroscopy (EELS), and nanometer resolution Auger spectroscopy with an electrostatic prism (CHA). The Kerr scattering apparatus and the thin-film deposition and analysis instrumentation are also indicated.

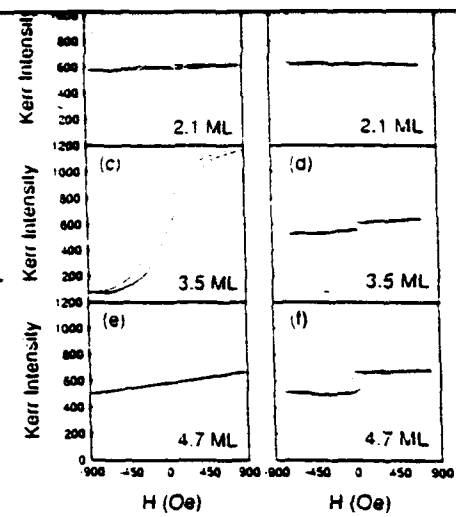

FIG. 5. Room-temperature-grown fcc Fe/Cu(100) polar and longitudinal surface magneto-optical Kerr-effect (SMOKE) hysteresis loops. The incident angle is 45° for both longitudinal and polar SMOKE measurements: (a) Polar, 2.1 ML; (b) longitudinal, 2.1 ML; (c) polar, 3.5 ML; (d) longitudinal, 3.5 ML; (e) polar, 4.7 ML; and (f) longitudinal, 4.7 ML. All measurements made at room temperature.

and 75 nm. Evaporation rates of 0.14 ML/min were calibrated by Auger electron spectroscopy, Rutherford backscattering, and a quartz-crystal microbalance. Detailed growth conditions and microstructural analysis will be published elsewhere.[28,30]

The thickness dependence of SMOKE hysteresis loops of as-grown fcc Fe on room-temperature Cu(100) substrates is shown in Fig. 5. For Fe film thicknesses below 2 ML, no magnetic response (not shown) was observed. Initial magnetic response is observed as a zero-remanence linear hysteresis loop in the polar direction, with no magnetization in plane, Figs. 5(a) and 5(b). At intermediate thicknesses, 3.5 ML, remanent polar, Fig. 5(c), and longitudinal, Fig. 5(d), SMOKE loops are observed. While the in-plane loop is square, the tilted polar loop displays the effects of shape anisotropy indicating a canted easy axis. SMOKE loops from thicker films, 4.7 ML, shown in Figs. 5(e) and 5(f), lose polar remanence, but have square in-plane loops characteristic of an in-plane easy-axis. As-grown in-plane remanence and saturation magnetization both increase nearly linearly with thickness below 5 ML indicating that most of the film (above 2 ML) is magnetically active. Films thinner than 10 ML had fcc structure with the transverse lattice constant of the substrate. Detailed analysis of the growth process using ultrahigh-resolution secondary electron and Auger electron images indicates that locally, some surface islands of Fe form at submonolayer coverages. In-surface islands (segregation) have been observed in the 1–2 ML regime, while layer-by-layer growth with some local but well-separated islands occurs for thicknesses above 2 ML.

We examined the magnetization switching process for the 4.7-ML-thick Fe films in the longitudinal, transverse, and polar directions. In Figs. 6(a)–6(c), polar, longitudinal and transverse (longitudinal polarization, transverse field) Kerr-effect loops are shown where an easy axis of in-plane magnetization lies along the longitudinal field axis. In Fig. 6(d), a longitudinal loop is shown for the field axis rotated in the plane of the sample away from the easy magnetization axis by 45°. The effects of the rotation away from the easy axis are seen as a rounding and tilting of the hysteresis loop. When the easy axis is aligned with the longitudinal field axis, a symmetric, nearly square closed

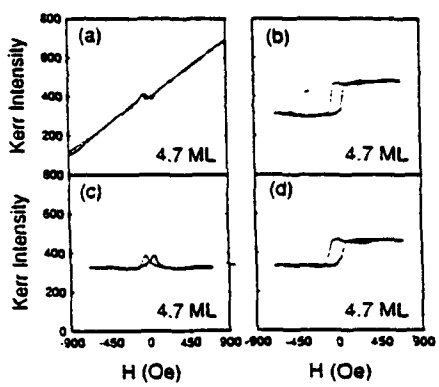

FIG. 6. Room-temperature-grown fcc Fe/Cu(100) polar and longitudinal surface magneto-optical Kerr-effect (SMOKE) hysteresis loops for 4.7-ML-thick films: (a) polar Kerr effect; (b) longitudinal Kerr effect, field along the longitudinal direction; (c) longitudinal Kerr effect with the applied-field direction perpendicular to the longitudinal axis in the plane of the surface; and (d) the longitudinal Kerr effect with the field applied at a 45° angle with respect to the the scattering plane (detection axis) also in the plane of the surface.

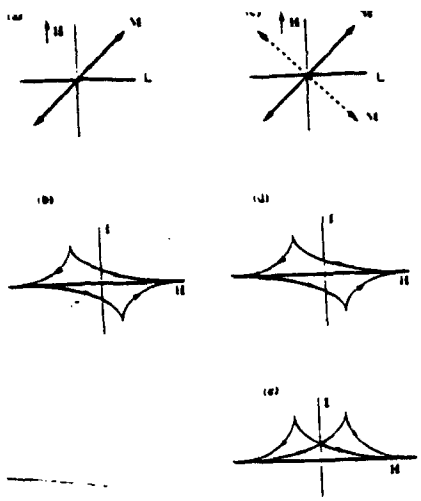

FIG. 7. Simple hysteresis loops derived for in-plane uniaxial and biaxial anisotropies. (a) Field applied transverse to the longitudinal direction, in plane with uniaxial easy axes as indicated and (b) the resulting longitudinal detected signal. (c) Field applied transverse to the longitudinal direction, in plane with biaxial easy axes results in either (d) an irreversible rotation or (e) a reversible rotation, where reversible means that the magnetization does not undergo a full 360° rotation about the sample normal.

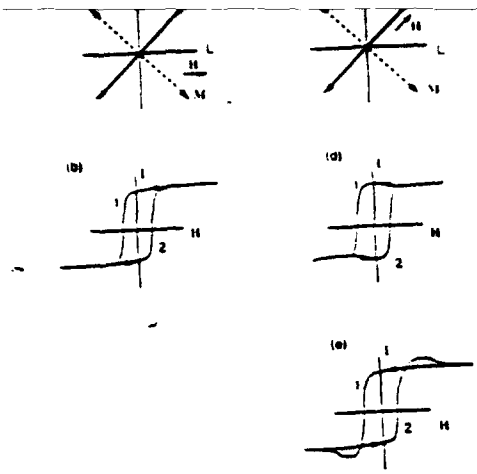

FIG. 8. Simple hysteresis loops derived for in-plane uniaxial and biaxial anisotropies. (a) Field applied along the longitudinal direction, in plane with uniaxial easy axes as indicated and (b) the resulting longitudinal detected signal. (c) Field applied at 45° with respect to the longitudinal direction, in plane with biaxial easy axes results in either (d) a clockwise rotation or (e) a counterclockwise rotation about the sample normal.

loop will be observed whether the anisotropy is uniaxial or biaxial (cubic) in the plane of the surface, Fig. 6(b). The magnetization can rotate in plane completely around the sample normal, in other words, a 360° in-plane rotation, as the longitudinal field is cycled. Alternatively, the magnetization can return in the same direction, never fully cycling about the sample normal. We distinguish between these two cases by terming the first switching process as irreversible, and the second switching process as reversible. If the anisotropy is uniaxial or cubic in plane, the curves will be (nearly) identical independent of the in-plane rotation mode.

The application of a transverse field only produces a longitudinal Kerr effect for our experimental arrangement, as given in Eq. (26). If the film is saturated in the transverse field direction, then the Kerr signal will be zero, Fig. 6(c). The structure of the transverse applied-field, longitudinal Kerr-effect signal can be explained by analyzing the simplified diagramatic representation in Fig. 7. A detailed micromagnetic analysis of these hysteresis loops will be given elsewhere. For simplicity, assume that the magnetization in a single domain in a uniaxial medium (distribution of uniaxial anisotropies) is oriented at 45° with respect to the field axis T and detection axis L, as shown in Fig. 7(a). When the field is cycled in the transverse direction, only one symmetry of hysteresis loop is allowed, Fig. 7(b). The exact shape of the loop and the position of the maxima (minima) will be a function of the angle between the applied field direction and the easy axis (distribution of easy axes), and in general will depend upon the exact mode of switching, e.g., coherent rotation or domain-wall motion. For the biaxial in plane anisotropy case, depicted in Fig. 7(c), two possible rotation modes in plane may be observed. As in the unaxial case, an irreversible hysteresis loop as shown in Fig. 7(d) may result. If the easy axes are oriented at nearly 45°, then a reversible hysteresis loop may result, as schematically depicted in Fig. 7(e). The reversible loop is stabilized by any longitudinal external stray field or any internal effective L-directed field. The experimental transverse-field axis hysterisis loop in Fig. 6(c) indicates that the in-plane anisotropy must be biaxial to provide the observed symmetry. Biaxial structural symmetry is present in the in-plane [100] directions in the fcc Fe film. The peaks in the hard field-axis loop coincide with the transition edges of the longitudinal field-axis loop in Fig. 6(b) (as required), and with the complex structure in the hard polar-axis loop in Fig. 6(a), which we discuss below.

When the applied field axis is rotated 45° with respect to the detection axis, Fig. 6(d), additional structure appears in the hysteresis loops. Once again, a schematic depiction of the switching process is shown in Fig. 8 for uniaxial and biaxial anistropies. For the uniaxial or biaxial case, when the applied field is along the detection axis, L in Fig. 8(a), the hysteresis loop will possess the characteristic form shown in Fig. 8(b). Once again, the coercivity and the rounding of the loop transitions will depend on the details of the switching process and the exact orientation of the easy axes with respect to the applied-field direction. When the field is applied at an acute angle with respect to the detection axis, shown in Fig. 8(c), two rotation modes are possible. We illustrate only the irreversible loops in Figs. 8(d) and 8(e) with the understanding that the reversible loop will be the combination of branch 1 from one hysteresis loop and branch 2 of the other loop. In Fig. 8(d) the detected hystersis loop for clockwise rotation can be contrasted with that of counterclockwise (in-plane) rotation in Fig. 8(e). The characteristic overshoot indicates which direction in the plane of the film that the magneti-

wise rotation is indicated. With this particular experimental arrangement, we cannot detect the difference between uniaxial and biaxial in-plane symmetry without resorting to analyzing the details of the hysteresis loops and performing micromagnetic simulations. However, we can define the handedness of the rotation process. Thus, given the four sets of data shown in Fig. 6, we can ascertain that the easy axis is in plane (in the sense that the demagnetization field is much larger than the perpendicular anisotropy) and biaxial, and that the magnetization rotation sense is well defined.

The out-of-plane hysteresis loops are more complex. Should the incident beam have been directed normal to the sample surface, then the hysteresis loop in Fig. 6(a) would have been a straight line. However, we see that according to Eq. (27) that the longitudinal signal is superimposed on the polar signal, with an intensity ratio of roughly five to one. This allows a simultaneous investigation of the out-of-plane and in-plane rotation modes. It is clear that the polar curve is a hard axis (demagnetization field forcing the loop into plane even though there may be an out-of-plane anisotropy) loop away from the origin. In order to observe loops such as shown in Fig. 6(a), a canted out-of-plane uniaxial anisotropy must be present in the film. This requirement can be examined explicitly by minimizing the micromagnetic energy during the switching process, but that analysis is out of the scope of the present article and will be presented elsewhere. A schematic analysis of the switching process is shown in Fig. 9. Assume that an out-of-plane canted easy axis is oriented at an angle θ with respect to the polar [100] axis as shown in Fig. 9(a). For the ensuing analysis, assume that this canted easy axis is defined for a particular in-plane direction, as shown by the projection of the easy axis onto [010], which itself may be arbitrarily oriented with respect to the longitudinal axis, angle ϕ. The anisotropy is uniaxial, but canted, hence it is connected by projection to an in-plane anisotropy as well. (This projected in-plane uniaxial anisotropy is independent of the fourfold symmetric in-plane anisotropy discussed above.) The contributions to the polar (r_{sp}^{p}) Kerr loop are connected to the rotation of the magnetization depicted in Fig. 9(b) in the (110) plane (projection). The pure polar contribution to the detected signal is shown in Fig. 9(c). Here the magnetization is saturated by the applied polar field (1). As the field is decreased to zero, the magnetization will equilibrate in the remanent state (3). If the demagnetization field is much larger than the perpendicular anisotropy, there will be no remanence. If, however, the demagnetization field balances the anistropy at some out-of-plane angle, as shown in Fig. 9(c), then a finite polar remanence will be observed. As the field is increased in the negative direction, the film once again saturates (4), and returns to a negative remanent state (6) as the loop is closed. The contributions to the longitudinal (r_{sp}^{l}) Kerr loop are connected to the rotation of the magnetization in plane and are depicted in Fig. 9(d) for an irreversible loop (note that a reversible loop will be just one-half of the loop

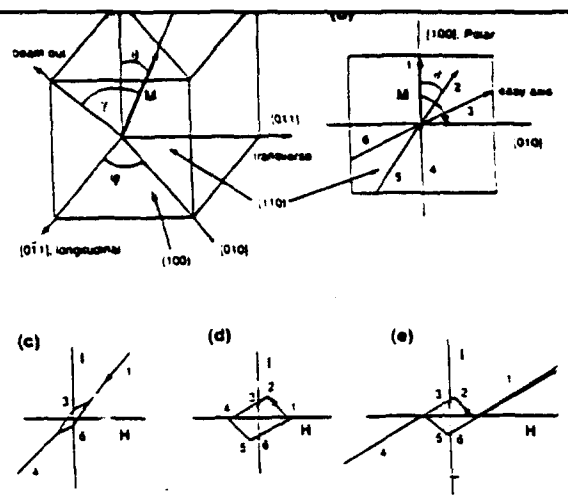

FIG. 9. Polar hysteresis loops for canted out-of-plane uniaxial anisotropy. (a) The sample normal is [100] and the easy axis lies at angle θ with respect to the sample normal. The projected in-plane anisotropy direction makes an angle ϕ with the scattering plane, which we have (arbitrarily) oriented along [010]. The (110) plane projected magnetization is shown in (b) during the rotation process with the application of a polar applied field. Individual positions of the magnetization during the rotation process correspond to locations along the hysterisis loops due to the (c) pure polar Kerr effect and (d) pure longitudinal Kerr effect. SMOKE at 45° incidence angle detects both the longitudinal and polar components simultaneously, the resulting Kerr loop is as shown in (e). Note that these diagrams are for a 360° rotation in plane about the sample normal (irreversible).

with return along the same path). When the film is saturated (1), no longitudinal signal is detected. At some angle γ the projection of the magnetization along the detection axis will be a maximum (2). This angle will in general depend in detail upon the out-of-plane easy axis orientation θ, the in-plane rotation projection of the easy axis with respect to the scattering plane ϕ, and the angle of incidence of the polarized beam. As the polar field is further reduced to zero (3), in-plane remanence results from the in-plane projection of the easy axis along the detection axis. As the field is increased in the negative direction, the magnetization rotates into the saturated hard-axis direction (4). For a reversible transition (in plane), upon reversal of the field direction, the magnetization will repeat its path. For an irreversible in-plane rotation, the loop is completed through positions (5) and (6) in the hysteresis loop. When the two components are added in the proper proportion, a compound loop such as that shown in Fig. 9(e) (irreversible loop) results. The experimental loop in Fig. 6(a) is a compound loop with a reversible in-plane rotation. For completeness, in Figs. 10(a) and 10(b) [after heating the film and slightly modifying the anisotropy as indicated by a change in the in-plane coercive field in Fig. 10(b)], the reversible and irreversible (in-plane rotation) polar Kerr-effect loops are shown. Although the loops seem more complex, it is apparant that the interpretation is direct, and the the information gleaned about the rotation process is more complete with a three-axis Kerr arrangement. Thus, in-plane anisotropy in room-temperature-grown fcc Fe/

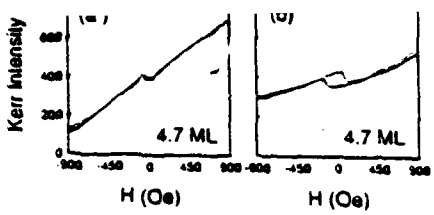

FIG. 10. (a) Reversible and (b) irreversible polar Kerr hysteresis loops for a 4.7-ML-thick room-temperature-grown fcc Fe/Cu(100) thin film.

Cu(100) has biaxial symmetry, likely along the four [100] directions in plane. The out-of-plane anisotropy is characterized by a canted uniaxial component which is weaker than the demagnetization field but only becomes apparant in the coupling of the in-plane and out-of-plane magnetization as detected by the three-axis Kerr arrangement.

IV. CONCLUSION

We have shown, for arbitrary angles of incidence, that all three magneto-optical Kerr effects (classified relative to the scattering plane) can be detected. The general expression of the normalized intensity for three-axis combined Kerr effect can be simplified by setting the orientations of the three main optical devices in the SMOKE system. The transverse Kerr effect can be eliminated from the combined Kerr effect by setting the appropriate configuration of three main optic devices. The longitudinal Kerr effect can be minimized at nearly normal incidence where the polar Kerr effect signal is maximized. The total reflection matrix, including the effect of interfering beams reflected from secondary boundaries, can be generalized to arbitrary multilayer structures. Modifying the matrix elements to include multiple interfering beams does not influence the dependence of the magnetization loops on the applied magnetic field for a film of a given thickness. This conclusion is essential in analyzing the steplike magnetization loops in multilayer thin films. Based on the simplified expressions for the intensity at the photodiode, the interpretation of SMOKE magnetization loops can provide valuable information about the magnetization state and magnetization switching process in thin films, such as in the fcc Fe/Cu epitaxial system.

We would like to acknowledge Dr. Gary Hembree and Dr. Jeff Drucker, and Sean Healy and Kevin Heim for collaboration. This work was supported by the Office of Naval Research under Grant No. N00014-93-1-0099.

APPENDIX A: BASIC FRESNEL SCATTERING MATRICES

According to Fig. 3, all reflection and transmission matrices at boundaries 1 and 2 (between media 1 and 2, and media 2 and 3, respectively) can be expressed in terms of the forward (backward)-going waves. Backward propagating waves are distinguished from forward propagating waves by the superscript bar. Superscripts on the electric fields indicate those boundaries at which the fields are evaluated. Additional superscripts on the field vectors i and r are used to emphase the incident and reflected directions of propagation. The subscripts 1 and 2 on the field vectors indicate in which medium the fields are evaluated. Finally, two subscripts on the reflection r and transmission t matrices indicate the two media bounding the interface, the first subscript being the incident side, and the second being the opposite side for the given propagation direction:

$$\begin{pmatrix} \epsilon_{p1}^{1r} \\ \epsilon_{s1}^{1r} \end{pmatrix} = \Re \begin{pmatrix} \epsilon_{p1}^{1i} \\ \epsilon_{s1}^{1i} \end{pmatrix} = \begin{pmatrix} \bar{r}_{pp} & \bar{r}_{ps} \\ \bar{r}_{sp} & \bar{r}_{ss} \end{pmatrix} \begin{pmatrix} \epsilon_{p1}^{1i} \\ \epsilon_{s1}^{1i} \end{pmatrix}, \tag{A1}$$

$$\begin{pmatrix} \epsilon_{p2}^{1i} \\ \epsilon_{s2}^{1i} \end{pmatrix} = t_{12} \begin{pmatrix} \epsilon_{p1}^{1i} \\ \epsilon_{s1}^{1i} \end{pmatrix} = \begin{pmatrix} \tilde{t}_{pp} & \tilde{t}_{ps} \\ t_{sp} & t_{ss} \end{pmatrix} \begin{pmatrix} \epsilon_{p1}^{1i} \\ \epsilon_{s1}^{1i} \end{pmatrix}, \tag{A2}$$

$$\begin{pmatrix} \bar{\epsilon}_{p2}^{2r} \\ \bar{\epsilon}_{s2}^{2r} \end{pmatrix} = r_{23} \begin{pmatrix} \epsilon_{p2}^{2i} \\ \epsilon_{s2}^{2i} \end{pmatrix} = \begin{pmatrix} \bar{\bar{r}}_{2pp} & \bar{\bar{r}}_{2ps} \\ \bar{\bar{r}}_{2sp} & \bar{\bar{r}}_{2ss} \end{pmatrix} \begin{pmatrix} \epsilon_{p2}^{2i} \\ \epsilon_{s2}^{2i} \end{pmatrix}, \tag{A3}$$

$$\begin{pmatrix} \bar{\epsilon}_{p1}^{1r} \\ \bar{\epsilon}_{s1}^{1r} \end{pmatrix} = \bar{t}_{21} \begin{pmatrix} \bar{\epsilon}_{p2}^{1r} \\ \bar{\epsilon}_{s2}^{1r} \end{pmatrix} = \begin{pmatrix} \bar{\bar{t}}_{pp} & \bar{\bar{t}}_{ps} \\ \bar{\bar{t}}_{sp} & \bar{\bar{t}}_{ss} \end{pmatrix} \begin{pmatrix} \bar{\epsilon}_{p2}^{1r} \\ \bar{\epsilon}_{s2}^{1r} \end{pmatrix}, \tag{A4}$$

$$\begin{pmatrix} \epsilon_{p2}^{1r} \\ \epsilon_{s2}^{1r} \end{pmatrix} = \bar{r}_{21} \begin{pmatrix} \bar{\epsilon}_{p2}^{1r} \\ \bar{\epsilon}_{s2}^{1r} \end{pmatrix} = \begin{pmatrix} \bar{\bar{r}}_{pp} & \bar{\bar{r}}_{ps} \\ \bar{\bar{r}}_{sp} & \bar{\bar{r}}_{ss} \end{pmatrix} \begin{pmatrix} \bar{\epsilon}_{p2}^{1r} \\ \bar{\epsilon}_{s2}^{1r} \end{pmatrix}. \tag{A5}$$

The coefficients of the bulk Fresnel reflection matrix $\Re$ are given by Eqs. (12), (14), (15), and (16) in the main text. The remaining coefficients are given explicitly as follows.[15] The Fresnel coefficients for the polar magneto-optical effect are

$$\tilde{r}_{pp} = \frac{2\mu_2 N_1 \cos\theta_1}{\mu_1 N_2 \cos\theta_1 + \mu_2 N_1 \cos\theta_2}, \quad \tilde{r}_{ss} = \frac{2\mu_2 N_1 \cos\theta_1}{\mu_2 N_1 \cos\theta_1 + \mu_1 N_2 \cos\theta_2},$$

$$\tilde{r}_{sp} = \bar{r}_{sp}, \quad \tilde{r}_{ps} = -i \frac{\mu_2 N_1 \cos\theta_1 (\mu_2 N_1^3 \cos^2\theta_1 - \mu_1 N_2^3 \cos\theta_1 \cos\theta_2) Q}{N_2^2 (\mu_1 N_2 \cos\theta_1 + \mu_2 N_1 \cos\theta_2)(\mu_2 N_1 \cos\theta_1 + \mu_1 N_2 \cos\theta_2)}, \tag{A6}$$

$$\bar{\bar{r}}_{pp} = \frac{2\mu_1 N_2 \cos\theta_2}{\mu_1 N_2 \cos\theta_1 + \mu_2 N_1 \cos\theta_2}, \quad \bar{\bar{r}}_{ss} = \frac{2\mu_1 N_2 \cos\theta_2}{\mu_2 N_1 \cos\theta_1 + \mu_1 N_2 \cos\theta_2},$$

$$\bar{\bar{r}}_{sp} = i \frac{\mu_1 N_2 (\mu_1 N_2 \cos\theta_1 - \mu_2 N_1 \cos\theta_2) Q}{2(\mu_1 N_2 \cos\theta_1 + \mu_2 N_1 \cos\theta_2)(\mu_2 N_1 \cos\theta_1 + \mu_1 N_2 \cos\theta_2)}, \tag{A7}$$

$$\bar{r}_{ps}=i\frac{\mu_1N_2(\mu_2N_1\cos\theta_1-\mu_1N_2\cos\theta_2)Q}{2(\mu_1N_2\cos\theta_1+\mu_2N_1\cos\theta_2)(\mu_2N_1\cos\theta_1+\mu_1N_2\cos\theta_2)},$$

$$\bar{r}_{pp}=\frac{\mu_2N_1\cos\theta_2-\mu_1N_2\cos\theta_1}{\mu_2N_1\cos\theta_2+\mu_1N_2\cos\theta_1},\quad \bar{r}_{ss}=\frac{\mu_1N_2\cos\theta_2-\mu_2N_1\cos\theta_1}{\mu_1N_2\cos\theta_2+\mu_2N_1\cos\theta_1},$$

$$\bar{r}_{sp}=i\frac{\mu_1N_2(\mu_1N_2\cos\theta_1-\mu_2N_1\cos\theta_2)Q}{2(\mu_1N_2\cos\theta_1+\mu_2N_1\cos\theta_2)(\mu_2N_1\cos\theta_1+\mu_1N_2\cos\theta_2)},\tag{A8}$$

$$\bar{r}_{ps}=i\frac{\mu_2N_1(\mu_2N_1\cos\theta_1-\mu_1N_2\cos\theta_2)\{1-\cos\theta_2[(\mu_1N_2/\mu_2N_1)\cos\theta_1+\cos\theta_2]\}Q}{2(\mu_1N_2\cos\theta_1+\mu_2N_1\cos\theta_2)(\mu_2N_1\cos\theta_1+\mu_1N_2\cos\theta_2)},$$

$$\bar{r}_{2pp}=\frac{\mu_2N_3\cos\theta_3-\mu_3N_2\cos\theta_3}{\mu_2N_3\cos\theta_2+\mu_3N_2\cos\theta_3},\quad \bar{r}_{2ss}=\frac{\mu_3N_2\cos\theta_2-\mu_2N_3\cos\theta_3}{\mu_3N_2\cos\theta_2+\mu_2N_3\cos\theta_3},\tag{A9}$$

$$\bar{r}_{2sp}=-i\frac{\mu_3N_2(\mu_3N_2\cos\theta_3-\mu_2N_3\cos\theta_2)Q}{2(\mu_3N_2\cos\theta_3+\mu_2N_3\cos\theta_2)(\mu_2N_3\cos\theta_3+\mu_3N_2\cos\theta_2)},$$

$$\bar{r}_{2ps}=-i\frac{\mu_2N_3(\mu_2N_3\cos\theta_3-\mu_3N_2\cos\theta_2)\{1-\cos\theta_2[(\mu_3N_2/\mu_2N_3)\cos\theta_3+\cos\theta_2]\}Q}{2(\mu_3N_2\cos\theta_3+\mu_2N_3\cos\theta_2)(\mu_2N_3\cos\theta_3+\mu_3N_2\cos\theta_2)}.$$

For longitudinal effect, we have

$$\bar{t}_{pp}=\bar{t}'_{pp}=\frac{2\mu_2N_1\cos\theta_1}{\mu_1N_2\cos\theta_1+\mu_2N_1\cos\theta_2},\quad \bar{t}_{ss}=\bar{t}'_{ss}=\frac{2\mu_2N_1\cos\theta_1}{\mu_2N_1\cos\theta_1+\mu_1N_2\cos\theta_2},$$

$$\bar{t}_{sp}=\bar{t}'_{sp},\tag{A10}$$

$$\bar{t}_{ps}=i\frac{\mu_2N_1^2\cos\theta_1\sin\theta_1[\mu_2N_1(1+\cos^2\theta_2)+\mu_1N_2\cos\theta_1\cos\theta_2]Q}{N_2\cos\theta_2(\mu_1N_2\cos\theta_1+\mu_2N_1\cos\theta_2)(\mu_2N_1\cos\theta_1+\mu_1N_2\cos\theta_2)},$$

$$\bar{t}_{pp}=\bar{t}'_{pp}=\frac{2\mu_1N_2\cos\theta_2}{\mu_1N_2\cos\theta_1+\mu_2N_1\cos\theta_2},\quad \bar{t}_{ss}=\bar{t}'_{ss}\frac{2\mu_1N_2\cos\theta_2}{\mu_2N_1\cos\theta_1+\mu_1N_2\cos\theta_2},$$

$$\bar{t}_{sp}=i\frac{\mu_1N_1\sin\theta_1(\mu_1N_2\cos\theta_1-\mu_2N_1\cos\theta_2)Q}{2\cos\theta_2(\mu_1N_2\cos\theta_1+\mu_2N_1\cos\theta_2)(\mu_2N_1\cos\theta_1+\mu_1N_2\cos\theta_2)},\tag{A11}$$

$$\bar{t}_{ps}=-i\frac{\mu_1N_1\sin\theta_1(\mu_2N_1\cos\theta_1-\mu_1N_2\cos\theta_2)Q}{2\cos\theta_2(\mu_1N_2\cos\theta_1+\mu_2N_1\cos\theta_2)(\mu_2N_1\cos\theta_1+\mu_1N_2\cos\theta_2)},$$

$$\bar{r}'_{pp}=\frac{\mu_2N_1\cos\theta_2-\mu_1N_2\cos\theta_1}{\mu_2N_1\cos\theta_2+\mu_1N_2\cos\theta_1},\quad \bar{r}'_{ss}=\frac{\mu_1N_2\cos\theta_2-\mu_2N_1\cos\theta_1}{\mu_1N_2\cos\theta_2+\mu_2N_1\cos\theta_1},$$

$$\bar{r}'_{sp}=i\frac{\mu_1N_1\sin\theta_1(\mu_1N_2\cos\theta_1-\mu_2N_1\cos\theta_2)Q}{2\cos\theta_2(\mu_1N_2\cos\theta_1+\mu_2N_1\cos\theta_2)(\mu_2N_1\cos\theta_1+\mu_1N_2\cos\theta_2)},\tag{A12}$$

$$\bar{r}'_{ps}=-i\frac{N_1\sin\theta_1(\mu_2N_1\cos\theta_1-\mu_1N_2\cos\theta_2)[\mu_2N_1(1+\cos^2\theta_2)+\mu_1N_2\cos\theta_1\cos\theta_2]Q}{2N_2\cos\theta_2(\mu_1N_2\cos\theta_1+\mu_2N_1\cos\theta_2)(\mu_2N_1\cos\theta_1+\mu_1N_2\cos\theta_2)},$$

$$\bar{r}'_{2pp}=\frac{\mu_2N_3\cos\theta_2-\mu_3N_2\cos\theta_3}{\mu_2N_3\cos\theta_2+\mu_3N_2\cos\theta_3},\quad \bar{r}'_{2ss}=\frac{\mu_3N_2\cos\theta_2-\mu_2N_3\cos\theta_3}{\mu_3N_2\cos\theta_2+\mu_2N_3\cos\theta_3},$$

$$\bar{r}'_{2sp}=i\frac{\mu_3N_3\sin\theta_3(\mu_3N_2\cos\theta_3-\mu_2N_3\cos\theta_2)Q}{2\cos\theta_2(\mu_3N_2\cos\theta_3+\mu_2N_3\cos\theta_2)(\mu_2N_3\cos\theta_3+\mu_3N_2\cos\theta_2)},\tag{A13}$$

$$\bar{r}'_{2ps}=-i\frac{N_3\sin\theta_3(\mu_2N_3\cos\theta_3-\mu_3N_2\cos\theta_2)[\mu_2N_3(1+\cos^2\theta_2)+\mu_3N_2\cos\theta_3\cos\theta_2]Q}{2N_2\cos\theta_2(\mu_3N_2\cos\theta_3+\mu_2N_3\cos\theta_2)(\mu_2N_3\cos\theta_3+\mu_3N_2\cos\theta_2)}.$$

Transverse Fresnel reflection and transmission coefficients are

$$\bar{t}_{pp}=\frac{\mu_2N_1}{\mu_1N_2}(1+\bar{r}_{pp}),\quad \bar{t}_{ss}=1+\bar{r}_{ss},\quad \bar{t}_{sp}=\bar{t}_{ps}=0,\tag{A14}$$

$$\bar{t}_{pp}=\frac{\mu_1 N_2}{\mu_2 N_1}(1+\bar{r}_{pp}),\quad \bar{t}_{ss}=1-\bar{r}_{ss},\quad \bar{t}_{sp}=\bar{t}_{ps}=0, \tag{A15}$$

$$\bar{r}_{pp}=-\frac{\mu_1 N_2\cos\theta_1-\mu_2 N_1\cos\theta_2}{\mu_1 N_2\cos\theta_1+\mu_2 N_1\cos\theta_2}-\frac{i(\mu_1 N_2\cos\theta_1-\mu_2 N_1\cos\theta_2)\mu_2 N_1\sin\theta_2 Q}{(\mu_1 N_2\cos\theta_1+\mu_2 N_1\cos\theta_2)^2},$$
$$\bar{r}_{ss}=-\bar{r}_{ss},\quad \bar{r}_{sp}=\bar{r}_{ps}=0, \tag{A16}$$

$$\bar{r}_{2pp}=-\frac{\mu_3 N_2\cos\theta_3-\mu_2 N_3\cos\theta_2}{\mu_3 N_2\cos\theta_3+\mu_2 N_3\cos\theta_2}+\frac{i(\mu_3 N_2\cos\theta_3-\mu_2 N_3\cos\theta_2)\mu_2 N_3\sin\theta_2 Q}{(\mu_3 N_2\cos\theta_3+\mu_2 N_3\cos\theta_2)^2},$$
$$\bar{r}_{2ss}=-\frac{\mu_2 N_3\cos\theta_3-\mu_3 N_2\cos\theta_2}{\mu_2 N_3\cos\theta_3+\mu_3 N_2\cos\theta_2},\quad \bar{r}_{2sp}=\bar{r}_{2ps}=0. \tag{A17}$$

APPENDIX B: NORMALIZED DETECTED INTENSITY

First, consider the combined longitudinal and transverse effects ($m_l=0$) with $\theta_m=0$. From Eqs. (2)–(4) and (11)–(16), we have

$$\begin{aligned}\begin{pmatrix}E_p\\E_s\end{pmatrix}'&=\Re\begin{pmatrix}E_{0p}\exp(-i\varphi/2)\\E_{0s}\exp(i\varphi/2)\end{pmatrix}\\&=\Re\begin{pmatrix}E_0\cos\theta_p\exp(-i\varphi/2)\\E_0\sin\theta_p\exp(i\varphi/2)\end{pmatrix}\\&=\begin{pmatrix}m_t r'_{pp}(Q)E_{0p}e^{i[\delta'_{pp}-(\varphi/2)]}+r'_{pp}E_{0p}e^{i[\delta'_{pp}-(\varphi/2)]}+m_t r'_{ps}E_{0s}e^{i[\delta'_{ps}+(\varphi/2)]}\\ m_t r'_{sp}E_{0p}e^{i[\delta'_{sp}-(\varphi/2)]}+r'_{ss}E_{0s}e^{i[\delta'_{ss}+(\varphi/2)]}\end{pmatrix},\end{aligned} \tag{B1}$$

where $r'_{pp}(Q)$ is the second term of r'_{pp} and is liner to Q. The total electric field of the reflected light received by the detector can be written as

$$\begin{aligned}E_T&=E'_p\cos\theta_a+E'_s\sin\theta_a\\&=E_0\{[m_t r'_{pp}(Q)e^{i(\delta'_{pp}-\varphi/2)}+r'_{pp}e^{i(\delta'_{pp}-\varphi/2)}]\cos\theta_p\cos\theta_a+m_t r'_{ps}e^{i(\delta'_{ps}+\varphi/2)}(\cos\theta_a\sin\theta_p+\sin\theta_a\cos\theta_p e^{-i\varphi})\\&\quad+r'_{ss}e^{i(\delta'_{ss}+\varphi/2)}\sin\theta_p\sin\theta_a\}.\end{aligned} \tag{B2}$$

The normalized light intensity is

$$\begin{aligned}I=&\{[m_t r'_{pp}(Q)\cos(\delta'_{pp}-\varphi/2)+r'_{pp}\cos(\delta'_{pp}-\varphi/2)]\cos\theta_p\cos\theta_a+r'_{ss}\sin\theta_p\sin\theta_a\cos(\delta'_{ss}+\varphi/2)\\&+m_t r'_{ps}\cos\theta_a\sin\theta_p\cos(\delta'_{ps}+\varphi/2)+m_t r'_{ps}\sin\theta_a\cos\theta_p\cos(\delta'_{ps}-\varphi/2)\}^2+\{[m_t r'_{pp}(Q)\sin(\delta'_{pp}-\varphi/2)\\&+r'_{pp}\sin(\delta'_{pp}-\varphi/2)]\cos\theta_p\cos\theta_a+r'_{ss}\sin\theta_p\sin\theta_a\sin(\delta'_{ss}+\varphi/2)+m_t r'_{ps}\cos\theta_a\sin\theta_p\sin(\delta'_{ps}+\varphi/2)\\&+m_t r'_{ps}\sin\theta_a\cos\theta_p\sin(\delta'_{ps}-\varphi/2)\}^2.\end{aligned} \tag{B3}$$

If we set $\theta_a=0$, Eq. (B3) is reduced to Eq. (25). Further simplification can be achieved by choosing appropriate settings on the modulator, which was shown in Sec. II by Eqs. (26) and (27). Another common case is to set $\theta_p=90°$, $\theta_m=45°$, $\theta_a=0$; then the normalized intensity of the three combined Kerr effects can be written as

$$\begin{aligned}I=&[\tfrac{1}{2}(r'_{pp})^2+m_t r'_{pp}(Q)r'_{pp}\cos(\delta'_{pp}-\delta'_{pp})]\\&-[m_p r'_{pp}r''_{sp}\sin(\delta'_{pp}-\delta''_{sp})+m_t r'_{pp}r'_{ps}\sin(\delta'_{pp}-\delta'_{ps})]\\&\times\sin\varphi-[\tfrac{1}{2}(r'_{pp})^2+m_t r'_{pp}(Q)r'_{pp}\cos(\delta'_{pp}-\delta'_{pp})]\cos\varphi.\end{aligned} \tag{B4}$$

By expanding $\sin\varphi$ and $\cos\varphi$ into series expressions of Bessel functions as

$$\sin\varphi\cong 2J_1(\varphi_0)\sin\omega t=1.164\sin\omega t,$$

$$\cos\varphi\cong 2J_2(\varphi_0)\sin(2\omega t),$$

for $\varphi_0=108°$, and taking the 1ω mode on the modulator, we can reduce Eq. (B4) into a simple expression as

$$\begin{aligned}I=&[\tfrac{1}{2}(r'_{pp})^2+m_t r'_{pp}(Q)r'_{pp}\cos(\delta'_{pp}-\delta'_{pp})]\\&-1.164[m_p r'_{pp}r''_{sp}\sin(\delta'_{pp}-\delta''_{sp})+m_t r'_{pp}r'_{ps}\\&\times\sin(\delta'_{pp}-\delta'_{ps})]\sin\omega t.\end{aligned} \tag{B5}$$

[1] S. D. Bader, J. Magn. Magn. Mater. 100, 440 (1991).
[2] C. Liu, E. R. Moog, and S. D. Bader, J. Appl. Phys. 64, 5325 (1988).
[3] C. Liu, E. R. Moog, and S. D. Bader, Phys. Rev. Lett. 60, 2422 (1988).

[4] E. R. Moog and S. D. Bader, J. Appl. Phys. 61, 3729 (1987).
[5] J. M. Florczak and E. Dan Dahlberg, J. Appl. Phys. 67, 7520 (1990).
[6] J. M. Florczak, E. Dan Dahlberg, J. N. Kuznia, A. M. Wowchak, and P. I. Cohen, J. Appl. Phys. 69, 4997 (1991).
[7] F. Saurenbach, U. Waiz, L. Hinchey, P. Grunberg, and W. Zinn, J. Appl. Phys. 63, 3473 (1988); S. T. Purcell, W. Folkerts, M. T. Johnson, N. W. E. McGee, K. Jager, J. aan de Stegge, W. B. Zeper, W. Hoving, and P. Gruberg, Phys. Rev. Lett. 67, 903 (1991); W. Durr, T. Woike, T. Beier, and D. Pescia, J. Phys. (Paris) Colloq. 49, C8-1615 (1988); P. Gruberg, S. Demokritov, A. Fuss, M. Vohl, and J. A. Wolf, J. Appl. Phys. 69, 4789 (1991); Q. Qiu, J. Pearson, A. Berger, and S. D. Bader, Phys. Rev. Lett. 68, 1398 (1992).
[8] J. A. C. Bland, R. D. Bateson, P. C. Riedi, R. G. Graham, H. J. Lauter, J. Penfold, and C. Shackleton, J. Appl. Phys. 69, 4989 (1991); M. T. Kief, G. J. Mankey, and R. F. Willis, *ibid.* 69, 5000 (1991); J. J. De Miguel, A. Cebollada, J. M. Gallego, R. Miranda, C. M. Schneider, P. Schuster, and J. Kirschner, J. Magn. Magn. Mater. 93, 1 (1991); P. Gruberg, J. Barnas, F. Saurenbach, J. A. Fuss, A. Wolf, and M. Vohl, *ibid.* 93, 58 (1991).
[9] J. Kerr, Philos. Mag. 3, 321 (1877).
[10] A. V. Sokolov, *Optical Properties of Metals*, translated by S. Chomet (Elsevier, New York, 1967).
[11] W. Voigt, *Magneto- und Electrooptik* (B. G. Teubner, Leipzig, 1908).
[12] P. N. Argyres, Phys. Rev. 97, 334 (1955).
[13] C. C. Robinson, J. Opt. Soc. Am. 53, 681 (1963); C. C. Robinson, *ibid.* 54, 1220 (1964); C. C. Robinson, J. Appl. Phys. 38, 1482 (1967);
[14] G. Metzger, P. Pluvinage, and R. Torguet, Ann. Phys. (Leipzig) 10, 5 (1965).
[15] R. P. Hunt, J. Appl. Phys. 38, 1652 (1967).
[16] H. DuBois, Wied. Ann. 39, 25 (1890); P. D. Foote, Phys. Rev. 34, 96 (1912); S. G. Barker, Proc. Phys. Soc. 29, 1 (1917); S. Loria, Ann Phys. (Leipzig) 38, 887 (1912); J. H. Jackson and E. W. Lee, B. J. Appl. Phys. 1, 1397 (1968); R. Carey, B. W. J. Thomas, I. V. F. Viney, and G. H. Weaver, *ibid.* 1, 1679 (1968); R. Carey and B. W. J. Thomas, J. Phys. D 7, 2362 (1974); H. Schewe and H. Hoffmann, Physica B 89, 59 (1977).
[17] A. Perrier, Helv. Phys. Acta 9, 330 (1936); H. I. Williams, F. G. Foster, and E. A. Wood, Phys. Rev. 82, 119 (1951); C. A. Fowler and E. M. Fryer, *ibid.* 86, 426 (1952); C. A. Fowler and E. M. Fryer, Phys. Rev. 94, 52 (1954).
[18] T. Miyahara and M. Takahashi, Jpn. J. Appl. Phys. 15, 291 (1976).
[19] K. Sato, Jpn. J. Appl. Phys. 20, 2403 (1981).
[20] P. Q. J. Nederpel and J. W. D. Martens, Rev. Sci. Instrum. 56, 687 (1985).
[21] H. Hornauer, T. M. Atmono, and K. Roll, J. Magn. Magn. Mater. 83, 551 (1990).
[22] H. R. Zhai, Y. B. Xu, M. Lu, Y. Z. Miao, K. L. Hogue, H. M. Naik, M. Ahmad, and G. L. Dunifer, J. Appl. Phys. 70, 5858 (1991); L.-Y. Chen, W. A. McGahan, Z. S. Shan, D. J. Sellmyer, and J. A. Woollam, *ibid.* 67, 7547 (1990).
[23] E. R. Moog and S. D. Bader, Superlattices and Microstructures 1, 543 (1985); E. R. Moog, C. Liu, S. D. Bader, and J. Zak, Phys. Rev. B 39, 6949 (1989); E. R. Moog, J. Zak, M. L. Huberman, and S. D. Bader, Phys. Rev. B 39, 9496 (1989).
[24] J. Zak, E. R. Moog, C. Liu, and S. D. Bader, J. Magn. Magn. Mater. 89, 107 (1990); J. Zak, E. R. Moog, C. Liu, and S. D. Bader, Phys. Rev. B 43, 6423 (1991).
[25] M. Farle, A. Berghaus, Y. Li, and K. Baberschke, J. Magn. Magn. Mater. 93, 215 (1991).
[26] D. H. Martin, K. F. Neal, and T. J. Dean, Proc. Phys. Soc. 86, 605 (1965); B. Donovan and T. Medcalf, Proc. Phys. Soc. 86, 1179 (1965).
[27] A. E. Bell, Proc. SPIE 382, 2 (1983); M. H. Kryder, J. Appl. Phys. 57, 3913 (1985).
[28] G. G. Hembree, J. S. Drucker, S. Healy, K. Heim, Z. Yang, and M. R. Scheinfein (unpublished).
[29] M. M. Noskov, Dok. Akad. Nauk SSSR 31, 2 (1941); 53, 5 (1946); M. M. Noskov and A. V. Sokolov, Zh. Eksp. Teor. Fiz. 17, 969 (1947).
[30] M. R. Scheinfein, J. S. Drucker, G. G. Hembree, S. Healy, K. Heim, and Z. Yang (unpublished).

Field Induced Metastable States in Ultrathin Films of fcc Fe/Cu(100)

G.G. Hembree, Jeff Drucker[a)], S.D. Healy, K.R. Heim, Z.J. Yang, M.R. Scheinfein
Department of Physics and Astronomy
Arizona State University, Tempe, AZ 85287-1504
(Revised 11 December 1993)

Abstract

The thickness dependence of both the perpendicular and in-plane magnetization is observed for pseudomorphic ultrathin, fcc Fe epitaxial films grown on room temperature Cu(100). Ferromagnetically ordered 3.5 ML thick films display both in-plane and perpendicular remanence. Perpendicular remanence, lost after a 9.0 kOe static field is applied perpendicular to the film plane, can be restored by either heating or applying large in-plane fields. These field induced metastable states are interpreted in terms of magneto-elastic effects which modify the exchange and anisotropy constants both perpendicular to and within the film plane.

PACS numbers: 75.70.Ak, 68.55.Jk, 75.30.Gw, 75.30.Pd

In press
(Appl Phys Lett)

Ferromagnetic ultrathin epitaxial films grown on single crystal metal substrates display unusual properties characteristic of two-dimensional ferromagnetism stabilized by magnetic (surface) anisotropy [1]. Ultrathin films, grown epitaxially on templates which distort the bulk lattice are often highly strained enabling metastable film properties to be explored at room temperature. The fcc phase of Fe, stable in bulk above 911^{o} C [2], can be grown epitaxially on Cu(100) with 0.83% lattice mismatch. For fcc (fct) Fe, a non-magnetic, high and low spin, or an antiferromagnetic phase can be stable depending upon the lattice constant [3]. The magnetic properties of fcc Fe/Cu(100) have been investigated using the surface magneto-optical Kerr effect (SMOKE) [4,5], spin-polarized photoemission [6], spin-polarized secondary electron spectroscopy [7,8], conversion-Mössbauer spectroscopy [9], inverse photoemission [10] and spin-polarized scanning electron microscopy (SEMPA) [11]. The energy balance between surface anisotropy and shape anisotropy, both strong functions of film thickness, growth and measurement temperature [4,11-13], determine the easy axis of magnetization. Additionally, rich structural properties are present during various phases of film growth [12-18], including bilayer growth during initial phases of epitaxy [15-18], strain-relief at intermediate thicknesses, weak surface reconstructions [12], and fcc to bcc transitions [e.g. 13]. Correlations of film microstructure with magnetic properties [12,13,19] has emphasized the onset of ferromagnetism at 1-2 ML coverages, the polar-to-longitudinal transition in the easy axis of magnetization at 4-8 ML, and the fcc to bcc transition at high coverages.

In this letter we identify a field induced, reversible, metastable transition for magnetization measured perpendicular (polar) to the film plane. Room-temperature grown, fcc Fe/Cu(100) films in the 2.5-3.5 ML regime possess both in-plane and perpendicular remanence. After application of a 9.0 kOe polar field, the out-of-plane remanence is lost. This magnetic state is stable until the film is either heated or subjected to a large in-plane magnetic field.

The specimen preparation chamber of a UHV scanning transmission electron microscope (STEM) [20], a Vacuum Generators HB501-S operating at base pressures of 5×10^{-11} mbar, has been equipped with surface characterization and film growth instrumentation. Surface magneto-optic Kerr effect (SMOKE) hysteresis loops were recorded by scattering modulated (polarized), He-Ne (632.8 nm) laser light from magnetic surfaces at an angle of incidence of 45°. Electromagnets situated ex-situ, produce maximum continuous fields of 1.2 kOe (1.5 kOe) in the polar (in-plane) direction. Nanometer lateral spatial resolution surface microanalysis, using secondary electron or Auger electron spectroscopy and imaging [20] was performed in the magnetic field of the STEM objective lens. This instrumentation allows for epitaxial film microstructure to be correlated with magnetic properties.

Single crystal electropolished [21] Cu(100) substrates were cyclically sputtered at 330° C with 600 eV Ar ions at 45° incident angles, then annealed at 600° C. Samples were observed in the electron microscope where contamination coverages of less than 0.01% of a monolayer can be detected [22]. Fe films were grown with an electron beam Fe source on room temperature Cu(100) surfaces. Evaporation rates were calibrated by Auger electron spectroscopy, Rutherford backscattering and a quartz-crystal microbalance. The pressure during evaporation was normally below 2×10^{-9} mbar; Auger spectra of prepared films showed detectable C and O peaks.

The thickness dependence of SMOKE hysteresis loops of as-grown fcc Fe/Cu(100) films are shown in Fig. 1. Initial magnetic response is observed as a zero-remanence, linear hysteresis loop in the polar direction, Figs. 1a and 1b. At intermediate thicknesses, 3.5 ML, remanent polar, Fig. 1c, and longitudinal, Fig. 1d, SMOKE loops are observed. While the in-plane loop is square, the tilted polar loop displays the effects of shape anisotropy indicating a canted out-of-plane easy-axis. SMOKE loops from thicker films, 4.7 ML, Figs. 1e and 1f, lose polar remanence, but have square in-plane loops characteristic of an in-plane easy-axis. The as-grown in-plane remanence increases

nearly linearly for thickness above 2 ML and below 5 ML. Thicker films (t -> 10 ML) become non-magnetic at room temperature [13]. Films thinner than 10 ML had fcc structure with the transverse lattice constant of the substrate [22].

Fig. 2 illustrates characteristic film structure observed using nm resolution UHV-SEM obtained in-situ subsequent to growth. The clean Cu(100) surface of Fig. 2a has average terrace widths between 25 and 75 nm, separated by steps (bands) . Nodules are copper-oxide contamination [22]. As Fe is deposited (2.1 ML and 3.5 ML in Fig. 2b and 2c) large regions where layer-by-layer growth has occurred are seen, separated by small three dimensional islands. Locally, some surface islands of Fe form at sub-monolayer coverages. In-surface islands (segregation) have been observed in the 1-2 ML regime, while layer-by-layer growth with some local but well separated islanding occurs for thicknesses above 2 ML.

The immersion objective of the STEM obtains nm spatial resolution with a 9.0 kOe polar magnetic field. After microstructural analysis in-situ in STEM, the magnetic response of the films had been altered. In Figs. 3a-d, longitudinal and polar SMOKE loops of as-grown films are contrasted with the post-observation (9.0 kOe polar field) polar and longitudinal SMOKE loops. After exposure to the field, there was no polar remanence. The in-plane loop remains square, with a small change in the coercivity, indicating an increase of the in-plane anisotropy constant. This state is stable until heating or application of a 1.5 kOe in-plane magnetic field. The reversibility of the transition is demonstrated in Figs. 3e-f. The metastable magnetic state induced by the 9.0 kOe field evolves after a small temperature increase (T =40^{o}C) as shown in Fig. 3e. After the application of an in-plane magnetic field (H=1.5 kOe), Fig. 3f, the initial state is nearly restored.

The out-of-plane to in-plane magnetization transition in ultrathin ferromagnetic films has been attributed to fluctuations in the two-dimensional Heisenberg model [23] at a transition temperature, lower than the Curie temperature. It is difficult to explain our

field-induced transformation in the context of two-dimensional fluctuations since large out-of-plane fields should enhance the in-plane to out-of-plane transition at temperatures below the critical transition temperature and large in-plane fields should stabilize the in-plane component of the magnetization [23].

The easy axis of magnetization and remanence are sensitive functions of the ultrathin film lattice. Thomassen et al. [13], through the deposition of CO on Fe/Cu(100) surfaces, concluded that ferromagnetic response resulted from the expanded surface lattice of the top-most layer while the bulk of the film remained paramagnetic. Covering the Fe film with Cu [24] greatly modifies the magnetic properties. Magnan et al. [19] utilized surface extended x-ray absorption fine structure (EXAFS) measurements to show that room temperature grown Fe/Cu(100) had similar nearest neighbor distances both in-plane and perpendicular to the surface. Total energy calculations [3] indicate that a small decrease in the lattice constant can stabilize a lower energy non-magnetic fcc Fe phase. While a field induced change in the anisotropy can explain the observed transition, the lack of perpendicular remanence in the metastable state could result from a local magnetic disordering of the film in the direction perpendicular to the surface as a result of magneto-elastic strains (compression) [25] induced by the 9.0 kOe magnetic field, stabilized by the presence of a lower energy, non-magnetic state. In this state, in-plane ferromagnetism may be preserved. Heating slightly expands the lattice, and locally reactivates the film. The application of large in-plane magnetic fields may compress the Fe film in-plane, with subsequent out-of-plane expansion, restoring the original state; a hypothesis which could be tested by performing in-field EXAFS measurements. In-plane lattice constants in the Fe film are stabilized by the Cu(100) template, and the magnitude of the original magnetic response is recovered.

We have observed a reversible, field induced metastable transition in the room temperature grown 3.5 ML fcc Fe/Cu(100) system. An interpretation based upon lattice distortions resulting from magneto-elastic effects is not inconsistent with our results. We

would like to acknowledge stimulating discussions with K. Schmidt, S. Bader and M. Hart. This work is supported by the Office of Naval Research under grant #N00014-93-1-0099. The microscopy was performed at the National Science Foundation supported Center for High Resolution Electron Microscopy, grant #DMR-91-15680.

References

[a]Center for Solid State Science, Arizona State University, Tempe, AZ 85287.

1. N.D. Mermin, H. Wagner, Phys. Rev. Lett. 17, 1133 (1966).
2. T.B. Massalski, **Binary Phase Diagrams : vol. 2**, (ASM International, Dayton, OH, 1990).
3. O.N. Mryasov, A.I. Liechtenstein, L.M. Sandratskii, V.A. Gubanov, J. Phys.: Condens. Matter 3, 7683 (1991); G.L. Krasko, G.B. Olson, Phys. Rev. B40, 11536 (1989); T. Kraft, M. Methfessel, M. van Schilfgaarde, M. Scheffler, Phy. Rev. B47, 9862 (1993); V.L. Moruzzi, P.M. Marcus, K. Schwarz, P. Mohn, Phys. B34, 1784 (1986).
4. C. Liu, E.R. Moog, S.D. Bader, Phys. Rev. Lett. 60, 2422 (1988); C. Liu, E.R. Moog, S.D. Bader, J. Appl. Phys. 64, 5325 (1988); C. Liu, S.D. Bader, J. Vac. Sci. Technol. A8, 2727 (1990); S.D. Bader, Proc. IEEE 78, 909 (1990).
5. W.R. Bennett, W. Schwarzacher, W.F. Egelhoff Jr., Phys. Rev. Lett. 65,3169 (1990).
6. D. Pescia, M. Stampanoni, G.L.Bona, A. Vaterlaus, R.F. Willis, F. Meier, Phys. Rev. Lett. 58, 2126 (1987).
7. D.P. Pappas, K.-P. Kamper, H.Hopster, Phys. Rev. Lett. 64, 3179 (1990).
8. D.P. Pappas, K.-P. Kamper, B.P. Miller, H.Hopster, D.E. Fowler, A.C. Luntz, C.R. Brundle, Z.-X. Shen, J. Appl. Phys. 69, 5209 (1991).
9. W.A.A. Macedo, W. Keune, Phys. Rev. Lett. 61, 475 (1988).
10. F.J. Himpsel, Phys. Rev. Lett. 67, 2363 (1991).
11. R. Allenspach, A. Bishof, Phys. Rev. Lett. 69, 3385 (1992).
12. P. Xhonneux, E. Courtens, Phys. Rev. B46, 5561 (1992).
13. J. Thomassen, F. May, B. Feldmann, M. Wuttig, H. Ibach, Phys. Rev. Lett. 69, 3831 (1992).

14. W.A. Jesser, J.W. Mathews, Phil. Mag. 15, 1097 (1967); Phil. Mag. 17, 461 (1968).

15. S.A. Chambers, T.J. Wagener, J.H. Weaver, Phys. Rev. B36, 8982 (1987).

16. D.A. Steigerwald, W.F. Egelhoff Jr, Surf. Sci. 192, L887 (1987); D.A. Steigerwald, F. Jacob, W.F. Egelhoff Jr., Surf. Sci. 202, 472 (1988).

17. H. Glatzel, Th. Farster, B.M.U. Scherzer, V. Dose, Surf. Sci. 254, 58 (1991).

18. A. Brodde, H. Neddermeyer, Ultramicr. 42-44, 556 (1991).

19. H. Magnan, D. Chandesris, B. Villette, D. Heckmann, J. Lecante, Phys. Rev. Lett. 67, 859 (1991).

20. G.G. Hembree, P.A. Crozier, J.S. Drucker, M. Krishnamurthy, J.A. Venables, J.M. Cowley, Ultramicr. **31**, 111 (1989).

21. Crystals were custom fabricated by Virgil Straughn, Monocrystals Inc., 1721 Sherwood Blvd., Cleveland, OH 44117.

22. K. Heim, S. Healy, Z.J. Yang, J.S. Drucker, G.G. Hembree, M. R Scheinfein, J. Appl. Phys. (to be published).

23. D. Pescia, V.L. Pokrovsky, Phys. Rev. Lett. 65, 2599 (1990); A. Kashuba, V.L. Pokrovsky, Phys. Rev. Lett. 70, 3155 (1993).

24. L.J. Swartzentruber, L.H. Bennett, M.T. Kief, W.F. Egelhoff, Jr. (in press, 1993).

25. S.W. Sun, R.C. O'Handley, Phys. Rev. Lett. 66, 2798 (1991); R.W. O'Handley, S. W. Sun , J. Mag. Mag. Mat. 10-4-107, 1717 (1992); R.C. O'Handley, S.W. Sun, in Science and Technology of Nanostructured Magnetic Materials , G.C. Hadjipanayis, G.A. Prinz, eds. (Plenum Press, New York), p. 109; R.C. O'Handley, S.W. Sun, Mat. Res. Soc. Symp. Proc. 231, 485 (1992).

Figure Captions

Figure 1: Room temperature grown fcc Fe/Cu(100) polar and longitudinal surface magneto-optical Kerr effect (SMOKE) hysteresis loops. The incident angle is 45^{o} for both longitudinal and polar SMOKE measurements which were made at room temperature.

Figure 2: High resolution secondary electron micrographs of (a) the clean Cu(100) surface. The white lines are steps (step bands) between terraces. The surface after deposition of (b) 2.1 ML and (c) 3.5 ML of Fe.

Figure 3: Room temperature grown 3.5 ML fcc Fe/Cu(100) polar and longitudinal SMOKE hysteresis loops. As grown, (a) longitudinal and (c) polar loops. After applying 9.0 kOe polar field, (b) longitudinal and (d) polar loops. (e) Polar loop after heating to 40 C, and (f) after applying a 1.5 kOe longitudinal field. All loops are on the same calibrated scale.

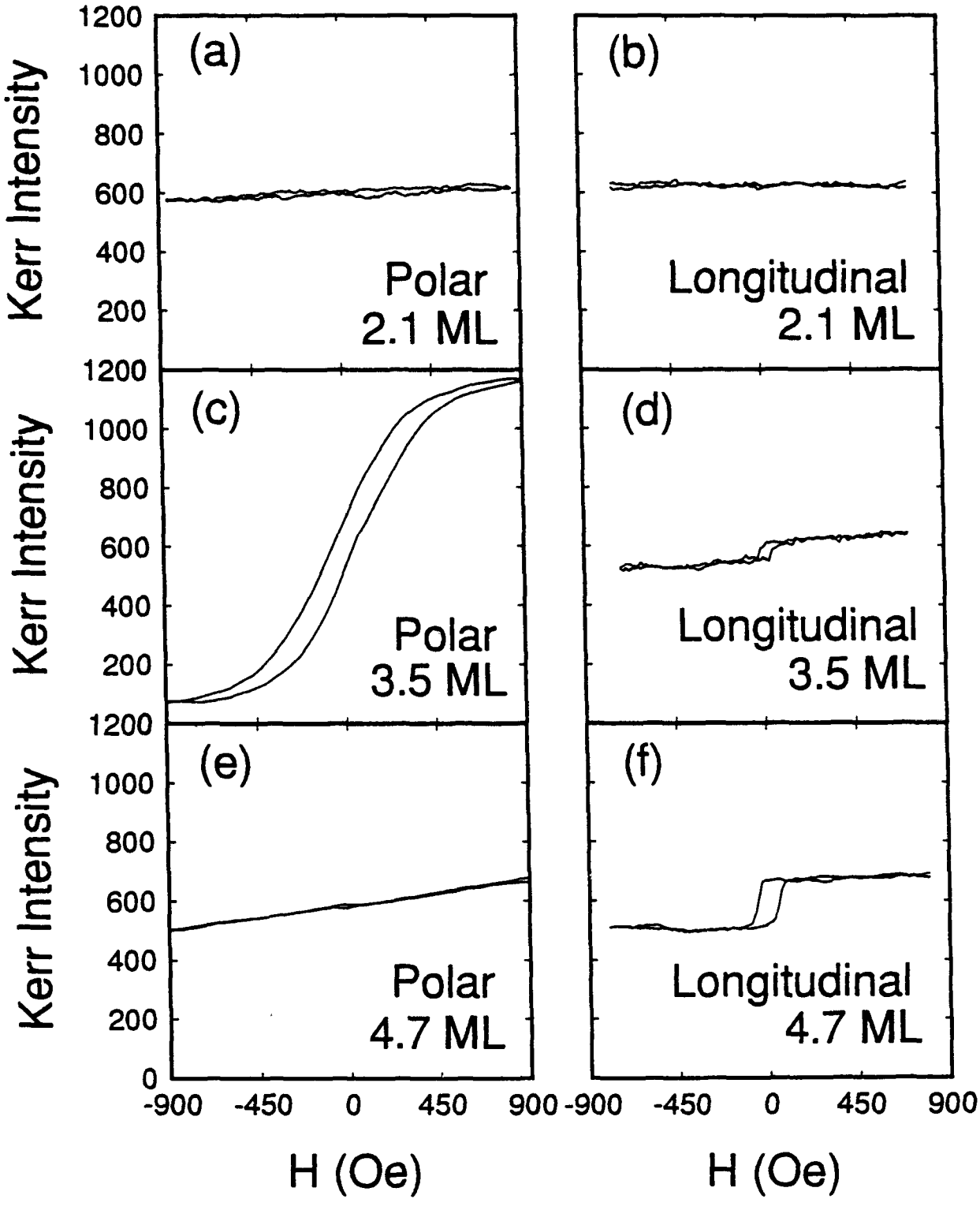

Removed at ref
Fig. 1
APL #L-9370

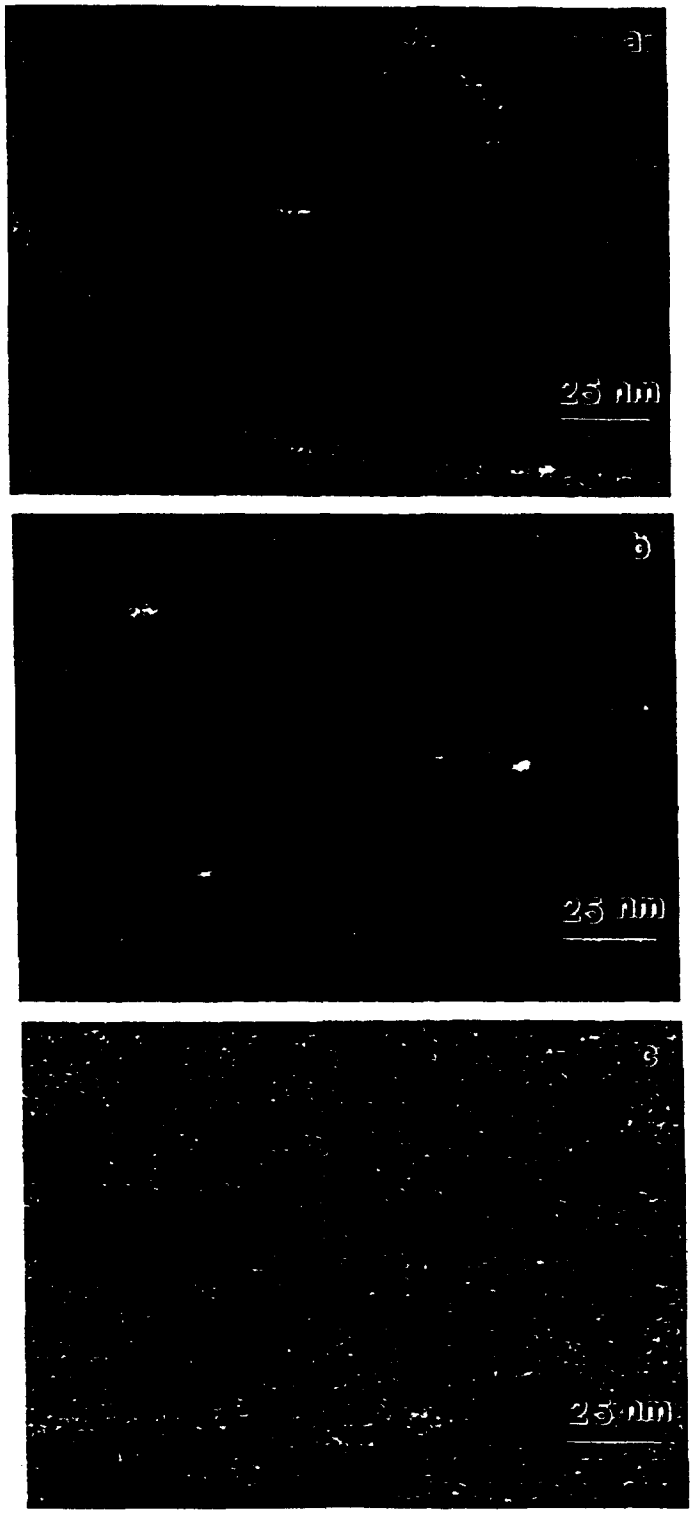

Fig. 2
- Amano et al.
VDL #L-9378

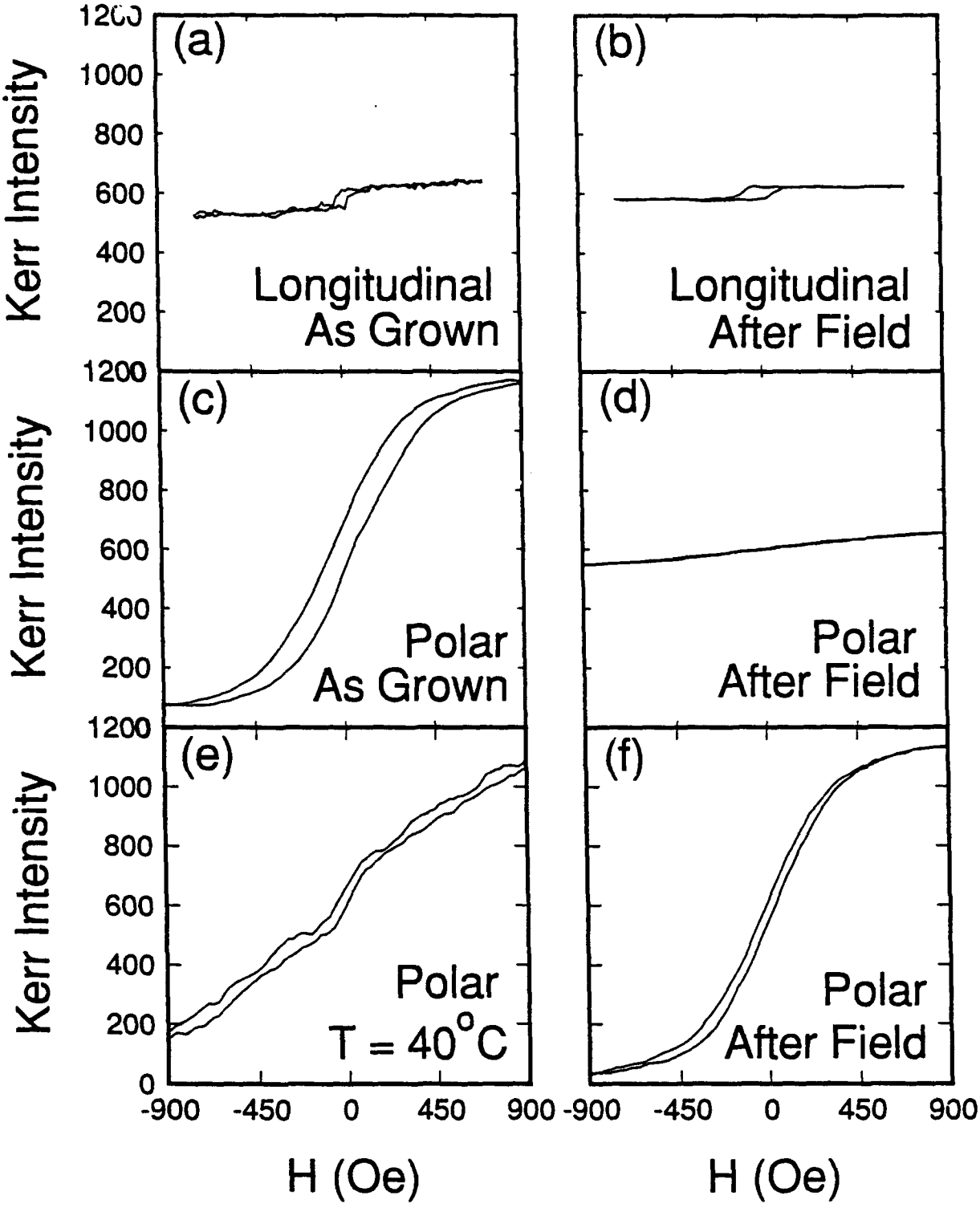

Fig 3
Hermance et al.
AEL # L-9378

Surface Magnetization Processes Investigated by The Combined Surface Magneto-Optical Kerr Effects in Fe/Cu(100) Thin Films

Z.J. Yang, S.D.Healy, K.R.Heim, J.S.Drucker, G.G.Hembree, and M.R. Scheinfein
Department of Physics and the Center for Solid State Science
Arizona State University
Tempe, AZ 85287-1504

(Received 16 August 1993)

Abstract

Surface and ultrathin-film anisotropies in epitaxial fcc Fe thin films grown on room temperature Cu(100) single crystals in an ultrahigh vacuum has been investigated, in situ, by the combined surface magneto-optical Kerr effects (SMOKE). When the applied field is perpendicular to the film surface, rotation processes occurring between out-of-plane and in-plane directions suggest the presence of an induced uniaxial (canted) anisotropy directed out of the plane of the film. This hypothesis is tested with a simple coherent rotation model.

PACS numbers: 75.70.Ak, 68.55.Jk, 75.30.Gw, 75.30.Pd

(in press, J. Appl. Phys.)

I. Introduction

The low dimensional properties predicted for ultrathin ferromagnetic films has stimulated considerable interest in exploring epitaxial metal/metal systems [1]. The most studied, and perhaps the most complex metal/metal epitaxial system is fcc Fe/Cu(100). Interpretation of data from the fcc Fe/Cu(100) system is complicated by rich physical structure which includes bilayer growth during initial phases of epitaxy [2-6], strain-relief at intermediate thicknesses, weak surface reconstructions [7], and fcc to bcc transitions [8]. Behavior of growth-temperature and film-thickness correlations with the magnetic spin orientations have also been intensively studied [2, 9, 10]. Our results for room temperature epitaxial Fe/Cu(100) thin films [11,12] indicate that subsurface Fe islands can form during the initial phases of epitaxy. For films thicker than 2 ML, nearly continuous Fe films have been observed, consistent with the onset of ferromagnetic ordering. Polar and longitudinal Kerr-effect measurements show that the easy axis transition from out-of-plane to in-plane (of the film) occurs near a thickness of 4.7 ML. Here, we describe a unique implementation of a combined three-axis magneto-optical Kerr effect apparatus which is used to explore mixed in-plane/out-of-plane rotation modes in ultrathin film Fe/Cu(100).

II. The Combined Three-Axis Surface Magneto-optical Kerr Effects

Three magneto-optical Kerr effects (polar, longitudinal, and transverse effects are shown in Fig.1) are classified according to the direction of the magnetization with respect to the plane of the incidence. Since the Kerr effect exists for any arbitrary direction of the magnetization (relative to the scattering plane), for non-normal incidence, magnetization loops obtained from any of the three Kerr effects may contribute to the detected signal. With different orientations of polarizer, modulator and analyzer, SMOKE can detect either all three magnetization components or any one of them. Thus, thin-film anisotropies and switching modes can be studied by comparing combined Kerr-effect magnetization loops [13,14]. The

normalized light intensity of the combined three-axis surface magneto-optical Kerr effects for our SMOKE measurements can be expressed as [13]

$$I = m_p^2 (r_{ps}^p)^2 + m_l^2 (r_{ps}^l)^2 + 2 m_p m_l r_{ps}^p r_{ps}^l \cos(\delta_{ps}^p - \delta_{ps}^l)$$
$$+0.2 r_{pp}^l m_p r_{ps}^p \sin(\delta_{pp}^l - \delta_{ps}^p) \sin \omega t + 0.2 r_{pp}^l m_l r_{ps}^l \sin(\delta_{pp}^l - \delta_{ps}^l) \sin \omega t, \quad (1)$$

where m_l and m_p are the direction cosines of the magnetization axes along the applied field direction (projection of M onto H) for longitudinal and polar Kerr effects respectively. r_{ps}^l and δ_{ps}^l are the absolute magnitude and the phase angle of the Fresnel reflection coefficients (superscripts indicate (p) polar or (l) longitudinal Kerr effects), and ω is the angular frequency of the modulator [13]. The expression for the intensity is independent of the transverse Kerr-effect regardless of the direction of the applied magnetic field in our SMOKE arrangement. It includes the contributions from both polar and longitudinal Kerr effects which allows us to investigate magnetization reorientations between out-of-plane and in-plane directions simultaneously.

III. Experimental Results

The specimen preparation chamber of a UHV scanning transmission electron microscope (STEM) [2], a Vacuum Generators HB501-S, operating at base pressures of 5 x 10^{-11} mbar, has been equipped with an in-situ SMOKE characterization system. Longitudinal, polar and transverse hysteresis loops were recorded by scattering modulated (polarized), He-Ne (632.8 nm) laser light from magnetic surfaces at an angle of incidence of 45^o [13]. Nanometer lateral spatial resolution surface microanalysis, using secondary electron or Auger electron spectroscopy and imaging allows for epitaxial film microstructure to be correlated with magnetic properties.

Single crystal Cu(100) substrates, were electropolished, cyclically sputtered at 330° C with 600 eV Ar ions at 45° incident angles, then annealed at 600° C. The thickness dependence of SMOKE hysteresis loops of as-grown fcc Fe on room temperature Cu(100) substrates has been given elsewhere [2]. In summary, for Fe film thicknesses below 2 ML, no magnetic response was observed. Initial magnetic response is observed as a zero-remanence, linear hysteresis loop in the polar direction, with no magnetization in-plane. At intermediate thicknesses, 3.5 ML, remanent polar and longitudinal SMOKE loops are observed. While the in-plane loop is square, the tilted polar loop displays the effects of shape anisotropy indicating a canted easy-axis. SMOKE loops from thicker films, 4.7 ML, loose polar remanence, but retain square in-plane loops characteristic of an in-plane easy-axis.

We examined the magnetization switching process for the as-deposited 4.7 ML thick Fe. In Fig. 2a-d, SMOKE loops are shown for applied fields along the longitudinal, 45° from longitudinal (in the plane of the film surface), transverse, and normal to the film surface (polar) directions respectively. Applied fields in Fig. 2a-c are in the film plane. A coherent rotation [14,15] model was employed to interpret these results. The normalized energy functional is given in eqn. 2, where K_{in} and K_{out} are the in-plane and out-of-plane anisotropies, M_S is the saturation magnetization, H_l, H_t, and H_p are the longitudinal, transverse and polar applied magnetic fields, θ is the polar angle (from the polar direction), ϕ is the azimuthal angle (from the longitudinal direction), α defines the out-of-plane easy axis angle, β defines the direction of the easy axis in the film plane, and c is a constant whose value is 1 (2) for uniaxial (cubic) in-plane anisotropy. External fields include the ramping field and any residual external stray fields. This expression was minimized using a conjugate gradient method. The results of this minimization are shown in Fig. 3a-f. The computed loops are meant to indicate gross structure as a means of interpreting the SMOKE results, and

discrepancies between the computed loops and the measurements are due to the crudeness of the model (i.e. no domain walls or domain wall motion).

$$E = \frac{1}{2}\sin^2(\theta-\alpha) + \frac{1}{2c}\frac{K_{in}}{K_{out}}\sin^2\{c(\phi-\beta)\}\sin^2\theta + \frac{2\pi M_s}{\left[\frac{2K_{out}}{M_s}\right]}\cos^2\theta -$$

$$\left\{\frac{H_l}{\left[\frac{2K_{out}}{M_s}\right]}\sin\theta\cos\varphi + \frac{H_t}{\left[\frac{2K_{out}}{M_s}\right]}\sin\theta\sin\varphi + \frac{H_p}{\left[\frac{2K_{out}}{M_s}\right]}\cos\theta\right\} \qquad (2)$$

The in-plane anisotropy is cubic, and oriented at 45° from the longitudinal direction (in the plane of the film surface). The perpendicular anisotropy is uniaxial and oriented 10° out of the film surface. The out-of-plane anisotropy was twice as large as the in-plane component, and equal to $2\pi M_s$. Figs. 3a-d show SMOKE hysteresis loops computed for the identical conditions described for Figs. 2a-d. Since the polar Kerr signal contains both longitudinal and polar components (eqn. 1), Fig. 3e and f show the polar and longitudinal components respectively. The polar signal is 5 times as large and of opposite sign than the longitudinal signal [13]. The general features are the asymmetrical structure on the corners of the loops in Figs. 2b and 3b, the twin peak structures in Figs. 2c and 3c, and the canted/inverted loops in Figs. 2d and 3d. When the field is applied in the transverse direction, a small stray field forces the loops to close in the same direction, thus not completing a 360° rotation in-plane. This is strong evidence for in-plane biaxial anisotropy [13]. When the field is applied along the polar direction, the magnetization rotates from a direction perpendicular to the plane into the plane as the field is reduced. As the field changes sign, the magnetization rotates in the plane of the surface first, aligning itself with the projection of the easy magnetization direction in the plane of the film. As the field is further

increased, the linear magnetization curve is once again observed. Upon return, the magnetization rotates within the film plane thus completing at least a 180^{o} rotation within the film plane during the switching process. These observations provide direct evidence for a canted induced uniaxial anisotropy.

IV. Conclusion

Three axis SMOKE measurements were used to determine the switching mode of intermediate thickness fcc Fe/Cu(100) epitaxial thin films. SMOKE loops observed with polar applied fields indicate a canted induced uniaxial anisotropy.

Acknowledgments

This work was supported by the Office of Naval Research under grant #N00014-93-1-0099.

References

1. U.Gradmann, J. Mag. Mag. Mat. 100, 481(1991).
2. G.G.Hembree, Jeff Drucker, S.D.Healy, K.R.Heim, Z.J.Yang, M.R.Scheinfein, Appl. Phys. Lett. (in press).
3. S.A.Chambers, T.J.Wagener, J.H.Weaver, Phys. Rev. B36, 8982(1987).
4. D.A.Steigerwald, W.F.Egelhoff Jr, Surf. Sci. 192,L887(1987); D.A.Steigerwald, F.Jacob, W.F.Egelhoff Jr, Surf. Sci. 202,472(1988).
5. H.Glatzel, Th.Farster, B.M.U.Scherzer, V.Dose, Surf. Sci. 254,58(1991).
6. A.Brodde, H.Neddermeyer, Ultramicr. 42-44,556(1991).
7. P.Xhonneux, E,Courtens, Phys Rev. B46, 5561(1992).
8. J.Thomassen, F.May, B.Feldmann, M.Wuttig, H.Ibach, Phys. Rev. Lett. 69, 3831(1992).

9. L.M.Falicov, Daniel T.Pierce, S.D.Bader, R.Gronsky, Kristl B.Hathaway, Herbert J.Hopster, David N.Lambeth, S.S.P.Parkin, Gary Prinz, Myron Salamon, Ivan K.Schuller, R.H.Victora, J. Mater. Res., 5(6), 1299(1990).

10. C.Liu, E.R.Moog, and S.D.Bader, Phys. Rev. Lett., 60, 2422(1988).

11. K.R.Heim, S.D.Healy, Z.J.Yang, G.G.Hembree, J.S.Drucker, M.R.Scheinfein, J. Appl. Phys. (in press).

12. S.D.Healy, K.R.Heim, Z.J.Yang, J.S.Drucker, G.G.Hembree, M.R.Scheinfein, J. Appl. Phys. (in press).

13. Z.J.Yang, M.R.Scheinfein, J. Appl. Phys. (in press).

14. J.M.Florczak, E.Dan Dahlberg, J.N.Kuznia, A.M.Wowchak, P.I.Cohen, J. Appl. Phys. 69, 4997 (1991).

15. E.C.Stoner and E.P.Wohlfarth, Phil. Trans. Roy. Soc., A240, 74(1948).

Figure Captions:

Figure 1: A schematic diagram of a SMOKE experiment. The polarizer, modulator and analyzer angles are θ_p, θ_m, and θ_a respectively relative to the scattering plane. The longitudinal, transverse and polar Kerr effect directions are also shown.

Figure 2: SMOKE loops are shown for applied fields along the (a) longitudinal, (b) 45^o from longitudinal (in the plane of the film surface), (c) transverse, and (d) normal to the film surface (polar) directions respectively. Applied fields in a-c are in the film plane.

Figure 3: Computed SMOKE loops are shown for applied fields along the (a) longitudinal, (b) 45^o from longitudinal (in the plane of the film surface), (c) transverse, and (d) normal to the film surface (polar) directions respectively. Since the polar Kerr signal contains both

longitudinal and polar components e and f show the polar and longitudinal components (to 3d) respectively. All loops are displayed on the same scale.

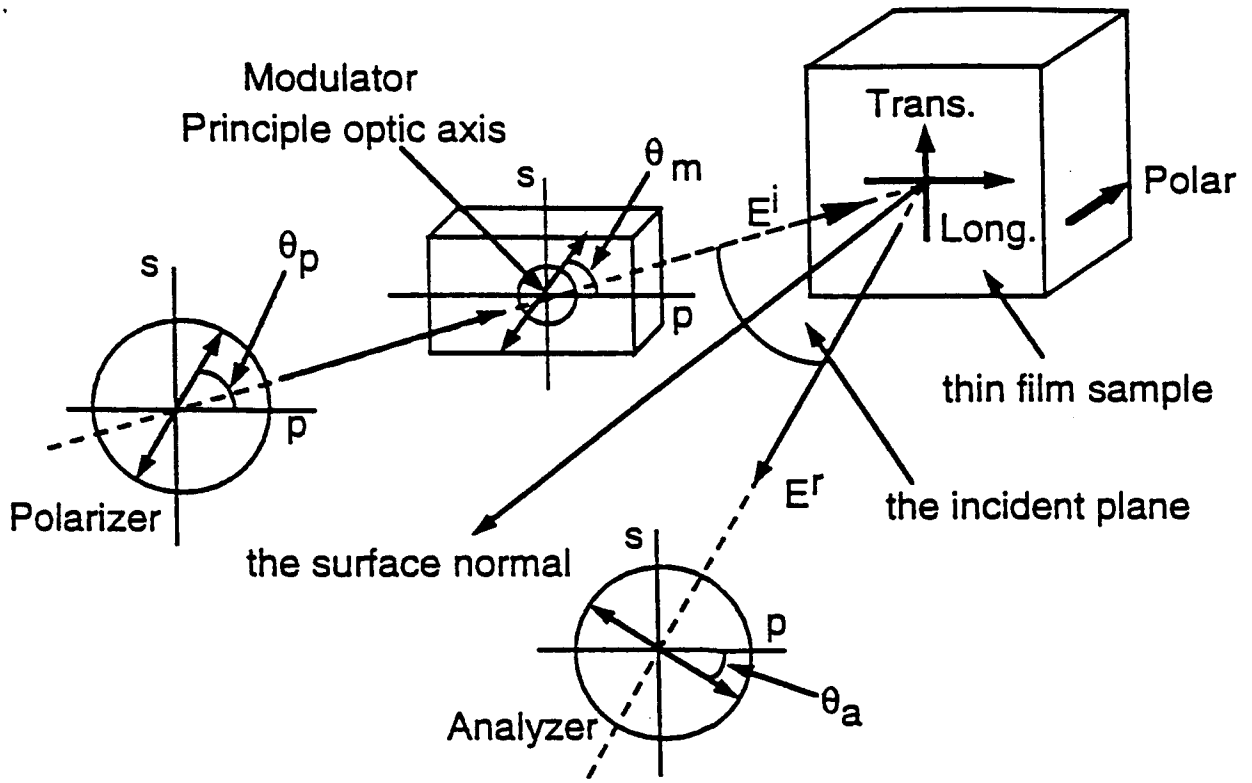
Modulator
Principle optic axis
s
θ m
Trans.
Polar
Long.
E^i
s
θp
p
p
thin film sample
Polarizer
E^r
the incident plane
the surface normal
s
p
θa
Analyzer

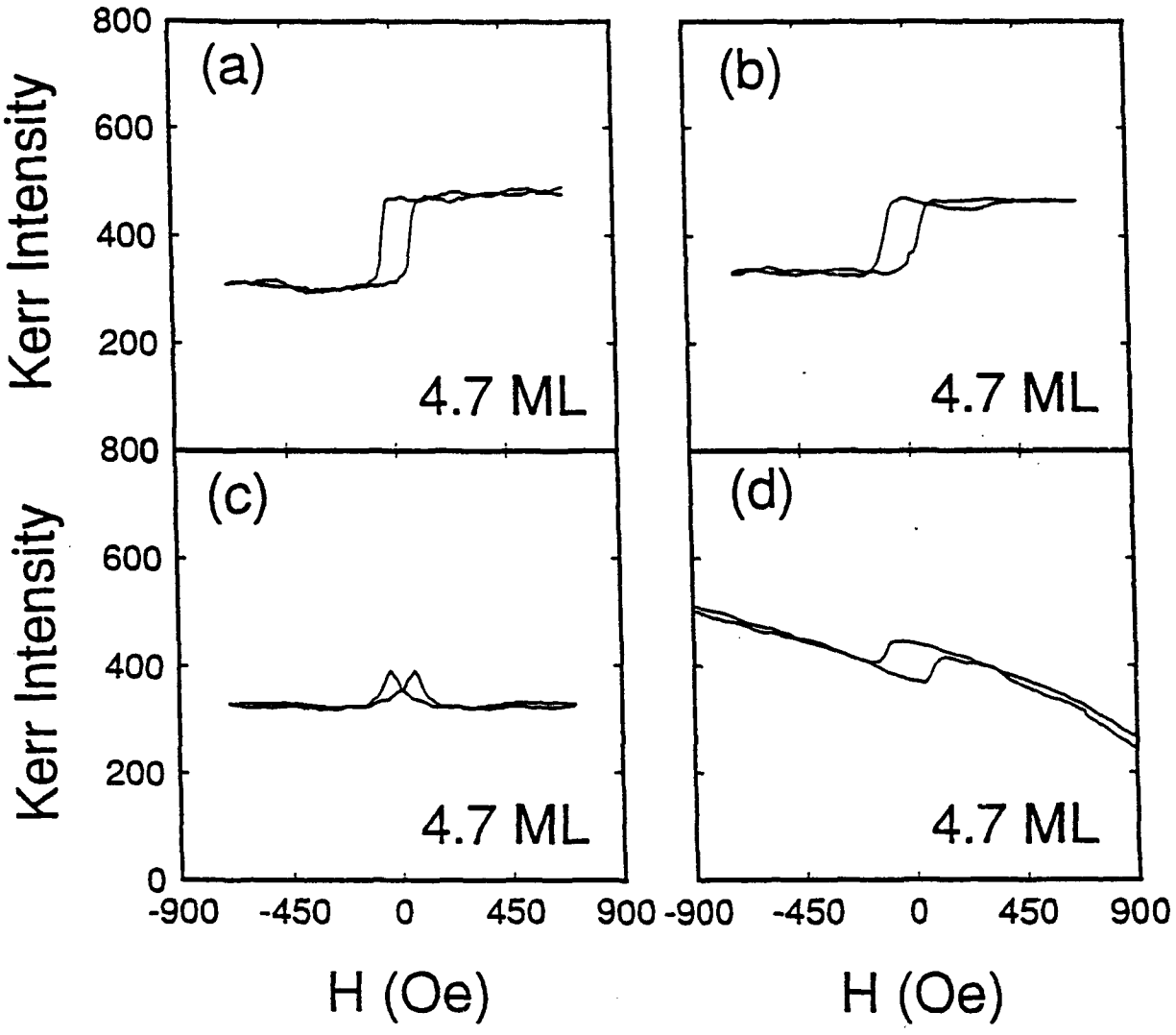
(a)
(b)
(c)
(d)
4.7 ML
4.7 ML
4.7 ML
4.7 ML
Kerr Intensity
Kerr Intensity
800
600
400
200
800
600
400
200
0
-900
-450
0
450
900
-900
-450
0
450
900
H (Oe)
H (Oe)

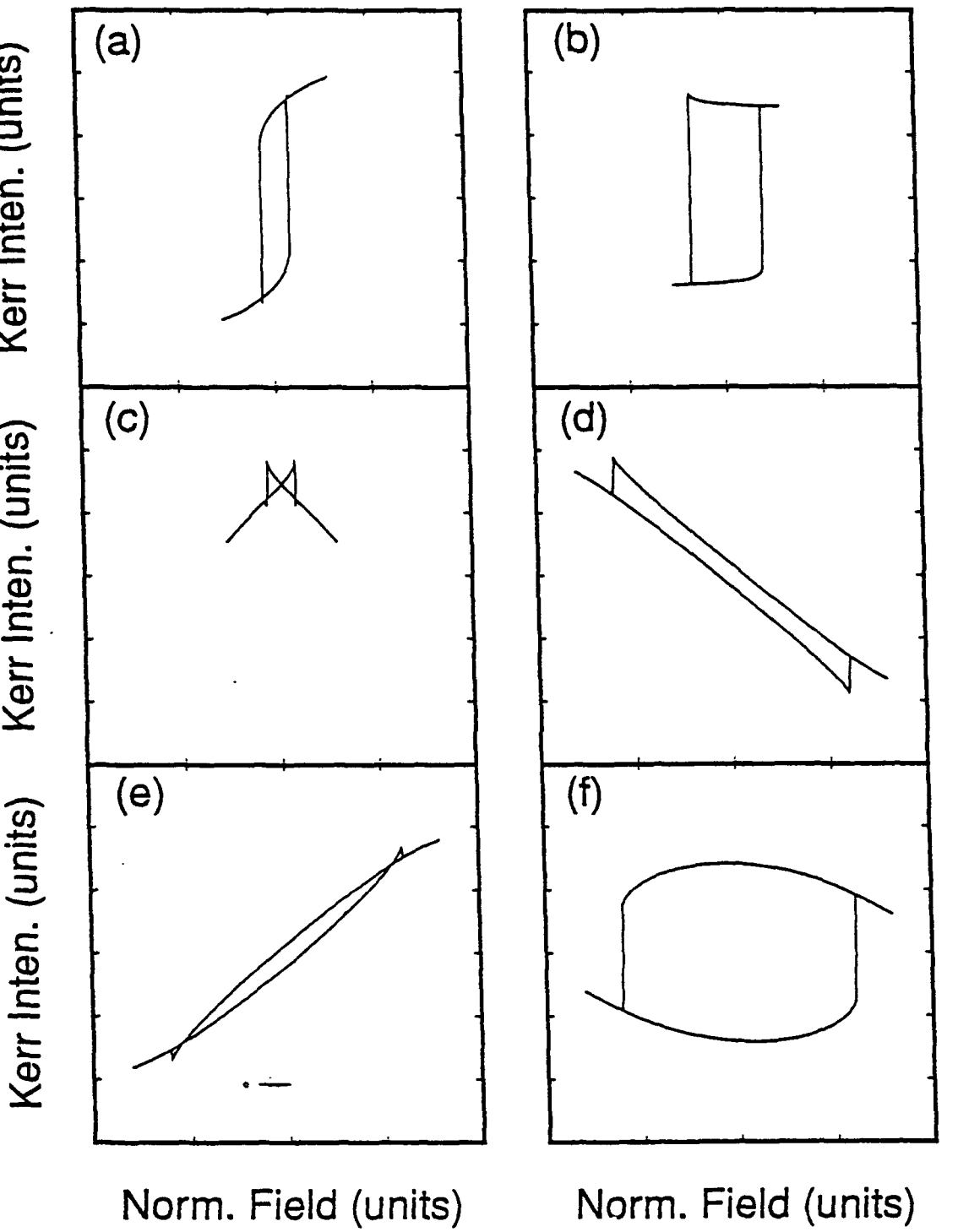
(a)
(b)
(c)
(d)
(e)
(f)
Kerr Inten. (units)
Kerr Inten. (units)
Kerr Inten. (units)
Norm. Field (units)
Norm. Field (units)

The Initial Phases of Epitaxy of fcc Fe/Cu(100): Supersurface and Subsurface Island Formation

S.D. Healy, K.R. Heim, Z.J. Yang, G.G. Hembree,

J. S. Drucker*, M. R. Scheinfein

Department of Physics and Astronomy

*Center for Solid State Science

Arizona State University, Tempe, AZ 85287-1504

(Received 22 June 1993)

Abstract

Nanometer transverse resolved real space observations of the initial phases of room temperature heteroepitaxy of fcc Fe/Cu(100) indicate that vertical atomic site exchange occurs locally. The formation of two-dimensional supersurface and subsurface islands has been characterized by secondary and Auger electron imaging. The persistence of vertical site exchange during the deposition of the first two monolayers is not inconsistent with the lack of observed ferromagnetism for the room-temperature grown fcc Fe/Cu(100) at these coverages.

PACS numbers: 75.70.Ak, 68.55.Jk, 75.30.Gw, 75.30.Pd

(in press J Appl. Phys)

Ferromagnetic ultrathin epitaxial films grown on single crystal metal substrates display unusual properties characteristic of two-dimensional ferromagnetism stabilized by magnetic (surface) anisotropy [1]. Extensive work has been devoted to correlating film microstructure with magnetic properties of the metastable [2] epitaxial fcc Fe/Cu(100) system. This has been stimulated by observations of rich structural properties present during various phases of film growth [3-10], including bilayer growth during initial phases of epitaxy [6,7], weak surface reconstructions [3], and strain-relief and fcc to bcc transitions for thicknesses greater than 11 ML [e.g. 4]. Vertical site exchange during the initial phases of epitaxy have been observed by High-Resolution Low-Energy Electron Diffraction [11], X-ray Photoelectron forward scattering [12] and scanning tunneling microscopy [13]. In this paper, we report not only on the supersurface Fe island formation, but also on real space, chemically specific, nanometer resolved observations of what appears to be subsurface island formation during the initial phases of room temperature epitaxial growth of fcc Fe/Cu(100).

The specimen preparation chamber of a UHV scanning transmission electron microscope (STEM) [14], a Vacuum Generators HB501-S, operating at a base pressure of $5x10^{-11}$ mbar, has been equipped for the in-situ preparation and characterization of ultrathin magnetic films. This instrumentation includes an ion sputtering gun, a broad beam Auger electron spectrometer, a RHEED analysis system, a specimen heating stage ($T < 800^{o}$ C) and an electron beam evaporator. Magnetic properties are characterized using a novel three-axis implementation of the surface magneto-optic Kerr effect (SMOKE) [15]. Nanometer lateral spatial resolution surface microanalysis, using secondary electron (SE) and Auger electron (AE) spectroscopy and imaging [14], was performed in the magnetic field of the STEM objective lens using the parallelizer principle [14,16]. This instrumentation allows for epitaxial film microstructure to be correlated with magnetic properties and is described in detail elsewhere [17].

Single crystal Cu(100) substrates , 1mm thick and 3mm in diameter, were electropolished [18], sputtered at 330° C with 225 nA of 600 eV Ar ions at 45° incident angles, then annealed at 600° C. Samples were observed in the electron microscope with biased SE imaging after the surface oxygen concentration had been depleted below the minimum detectable limits of our broad beam AE spectrometer. These surfaces often displayed small copper-oxide islands [17] at coverages of less than 0.01% of a monolayer which can be imaged in the microscope. Fe films were grown with an electron beam Fe source on clean, room temperature ($T < 40^{o}$ C) Cu(100) surfaces. Room temperature growth ensures longer (surface) diffusion lengths and films with lower defect densities. Evaporation rates of 0.14 ML/min were calibrated using Auger electron spectroscopy, Rutherford backscattering and a quartz-crystal microbalance. The pressure during evaporation was normally below 2×10^{-9} mbar.

The thickness dependence of the SMOKE hysteresis loops of as-grown fcc Fe/Cu(100) films, and the observation of a field induced, metastable state has been correlated with film microstructure [19]. Here, we focus on the characterization of films during the initial phases of epitaxy which are observed to be non-magnetic. Fig. 1 illustrates the surface structure of clean Cu(100) as observed, in-situ, using nm resolution UHV SE microscopy The surface has terraces with an average width between 25 and 75 nm (although some regions of the surface have extremely broad terraces), separated by steps (step bands) seen as white lines. The widely separated nodules are copper-oxide contamination remaining after surface preparation. After Fe deposition, RHEED analysis indicated an fcc film structure with the in-plane lattice constant of the substrate (3.61 Å) for all films thinner than 10 ML. (Our RHEED measurements permit an evaluation of the in-plane lattice constant to within ±4%.)

At low film coverages, supersurface island formation can be observed locally by correlating the SE images with the Cu and Fe AE images. One such set of spatially correlated images is displayed in Figure 2 for a 0.33 ML thick Fe film. SE images are

sensitive to both the work function and topography of the surface [20]. The SE image in figure 2a illustrates supersurface Fe islands with the corresponding contour plot shown in figure 2b. The large island (~45 nm in diameter) has intensity contours near its upper left quadrant indicating that this island is composed of more than one monolayer of Fe within the bulk of the island. The contrast of the smaller islands is identical to the contrast of the tip of the larger island (within the signal-to-noise limits of these measurements) indicating identical Fe island thicknesses. AE images and contour maps derived from the Cu (Figs. 2c and 2d) and Fe (Figs. 2e and 2f) Auger electron signals can be directly correlated with the SE image of the Fe islands. The AE images are produced by rastering the finely focused 100 keV incident electron beam across the sample surface and collecting most of the Fe (Cu) LMM peak Auger electrons using a spectrometer with a 1.5 eV window which is selected to pass electrons with the respective energy thus generating a two-dimensional surface map . A background map for each Auger map is subsequently acquired by selecting the pass band of the spectrometer to lie 20 eV higher than the Auger peak energy. The images shown in Figs. 2c and 2e result from subtracting the background map from the peak map, such that the intensity within each pixel of the image is proportional to the number of counts within a particular Auger peak, and, therefore, proportional to the number of atoms probed by the incident beam [14] (the sensitivity factors for the Cu and Fe LMM peaks are almost identical). The black areas in Fig. 2c indicate the lack of a Cu signal, while the white areas in Fig. 2e indicate the presence of Fe. It is evident by correlating the contrast in the images and contour maps that the large island and several smaller islands are composed of Fe. Since the signal-to-noise ratio is much better in the SE image, the island density pictured in Fig. 2a likely characterizes the surface.

Figure 3a-c displays SE, Cu AE and Fe AE images respectively, all in registry for a Cu substrate with 1.7 ML of Fe deposited at room temperature. The bright regions in the SE image are not correlated with any structure in the Cu (Fig. 3b) or Fe (Fig. 3c) AE images. However, these same Cu and Fe AE images with superimposed contour plots,

shown in Figs. 4a and 4b respectively, indicate the regions depleted of Cu are rich in Fe. Since there is no contrast in the SE image, and the SE yield for fcc Fe and Cu are practically identical ($\delta_{Fe}=\delta_{Cu}=0.38$ at 20 keV) [21], we conclude that there is no topographic structure on the surface in this region, indicating that the contrast observed in the AE images is a result of two-dimensional subsurface island formation. This conclusion is consistent with the work of others [11, 12, 13]. We have also observed both types of island growth as well as layer-by-layer growth in the same film at different positions along the film. This indicates that these phenomena are controlled by locally varying template surface conditions.

Our observations suggest that in the regions where subsurface islands occur, a vertical Fe-Cu atomic site exchange occurs. This process continues until the driving force causing the exchange diminishes. We observed this Fe coverage to be thicker than 2 ML, beyond which continuous Fe films grew.

The lack of ferromagnetic ordering observed in this sub-2 ML regime is not inconsistent with the observed growth process. In order for the moment of an Fe island to be stable against thermal fluctuations, it must have a minimum size. Assuming a Boltzmann-type probability distribution, it is straight forward to show that most of the Fe islands, which are ~4 nm in diameter (Figs. 2a and 2b), are too small for the moments to be unaffected by thermal energy.

In summary, we have observed both supersurface islanding and subsurface islanding through vertical atomic site exchange in room temperature grown films of fcc Fe/Cu(100) in the 0-2 ML regime. We observed no long range order to either the sub- or supersurface islands. These observations are not inconsistent with the lack of ferromagnetism observed in room temperature grown sub-2 ML fcc Fe/Cu(100) ultrathin films.

We would like to acknowledge stimulating discussions with K. Schmidt, S. Bader and M. Hart. We acknowledge G.-C. Wang for sending prepublication results. This

work is supported by the Office of Naval Research under grant #N00014-93-1-0099. The microscopy was performed at the National Science Foundation supported Center for High Resolution Electron Microscopy at Arizona State University, grant #DMR-91-15680.

References

1. N.D. Mermin, H. Wagner, Phys. Rev. Lett. 17, 1133 (1966).
2. L.J. Schwartzendrubber, **Binary Phase Diagrams: vol 2** (Publisher, 1990).
3. P. Xhonneux, E. Courtens, Phys. Rev. B46, 556 (1992).
4. J. Thomassen, F. May, B. Feldmann, M. Wuttig, H. Ibach, Phys. Rev. Lett. 69, 3831 (1992); J. Thomassen, B. Feldmann, M. Wuttig, Surf. Sci. 264, 406 (1992); H. Landskron, G. Schmidt, K. Heinz, K. Müller, C. Stuhlmann, U. Beckers, M. Wuttig, H. Ibach, Surf. Sci. 256, 115 (1991).
5. W.A. Jesser, J.W. Matthews, Phil. Mag. 15, 1097 (1967); W. A. Jesser, J. W. Matthews,Phil. Mag. 17, 461 (1968).
6. S.A. Chambers, T.J. Wagener, J.H. Weaver, Phys. Rev. B36, 8992 (1987); H. Glatzel, Th. Fauster, B.M.U. Scherzer, V. Dose, Surf. Sci. 254, 58 (1991).
7. D.A. Steigerwald, W.F. Egelhoff Jr, Surf. Sci. 192, L887 (1987); D.A. Steigerwald, I. Jacob, W.F. Egelhoff Jr., Surf. Sci. 202, 472 (1988).
8. S.H. Lu, J. Quinn, D. Tian, F. Jona, P.M. Marcus, Surf. Sci. 209, 364 (1989)
9. A. Brodde, H. Neddermeyer, Ultramicr. 42-44, 556 (1991).
10. H. Magnan, D. Chandesris, B. Villette, D. Heckmann, J. Lecante, Phys. Rev. Lett. 67, 859 (1991).
11. Y.-L. He, G.-C. Wang, Phys. Rev. Lett. (in press).
12. W.F. Egelhoff, Jr. Mat. Res. Soc. Symp. Proc. 229, 27 (1991).
13. S. Rousset, S. Chiang, D.E. Fowler, D.D. Chambliss, Phys. Rev. Lett. 69, 3200 (1992); H. Neddermeyer, private communication.
14. G.G. Hembree, P.A. Crozier, J.S. Drucker, M. Krishnamurthy, J.A. Venables, J.M. Cowley, Ultramicr. **31**, 111 (1989).
15. Z.J. Yang, M.R. Scheinfein, J. Appl. Phys. (submitted).

16. A.J. Bleeker, Ph. D. Thesis Technische Universiteit Delft, (1991); A. Bleeker, P. Kruit, Nucl. Instr. Meth. **A298**, 269 (1990); P. Kruit, J. A. Venables, Ultramicr. **25**, 183 (1988).

17. K.R. Heim, S.D. Healy, Z.J. Yang, G.G. Hembree, J.S. Drucker, M.R. Scheinfein, J. Appl. Phys. (submitted).

18. Crystals were custom fabricated by Virgil Straughn, Monocrystals Inc. Cleveland, OH.

19. G.G. Hembree, Jeff Drucker, S.D. Healy, K.R. Heim, Z.J. Yang, M.R. Scheinfein, Phys. Rev. Lett. (submitted).

20. L. Reimer, Scanning Electron Microscopy, (Springer-Verlag, Berlin, 1985).

21. H. Seiler, J. Appl. Phys. 54, R1 (1983)

Figure Captions

Figure 1: High resolution secondary electron micrographs of a clean Cu(100) surface. The white lines are steps (step bands) between terraces. The terraces have an average width of 25 to 75 nm.

Figure 2: After deposition of 0.33 ML of Fe at room temperature supersurface islands are observed: (a) secondary electron (SE) image, (b) contour map of SE image indicating island positions, (c) Cu LMM Auger electron (AE) image indicating Cu depletion (black) regions, (d) corresponding contour map of the Cu AE image, (e) Fe LMM AE image indicating Fe (white) islands, and (f) the corresponding contour map of the Fe AE image. The correlation of these three signals indicates that the islands have formed upon the Cu surface. These three images have identical scale factors.

Figure 3: After deposition of 1.7 ML of Fe at room temperature, subsurface islands are observed. (a) Secondary electron image, (b) Cu LMM Auger electron (AE) image indicating Cu depletion regions (black), and (c) Fe LMM AE image indicating Fe rich regions (white). The correlation of the structure in (b) and (c) and the lack of any contrast in (a) indicates that these islands are within the surface of the substrate. These three images have identical scale factors.

Figure 4: The same surface as depicted in figure 3: (a) Cu LMM Auger electron (AE) image indicating Cu depletion regions (black) with superimposed subsurface island contour lines and (b) Fe LMM AE image indicating Fe rich regions (white) with superimposed subsurface island contour lines. These two images have identical scale factors.

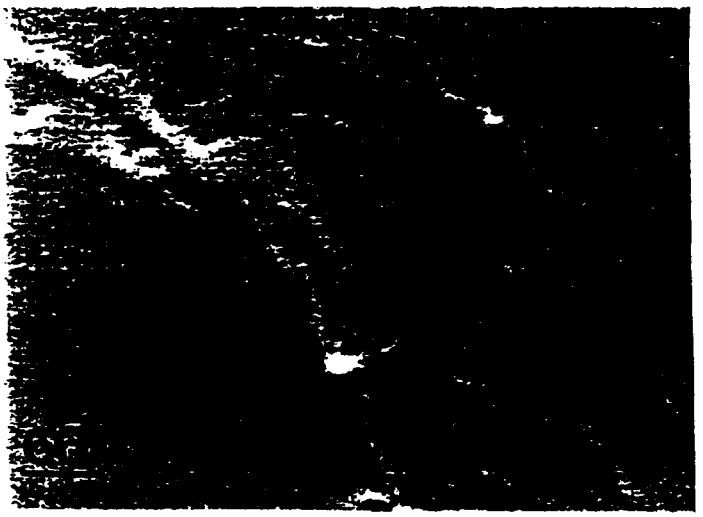

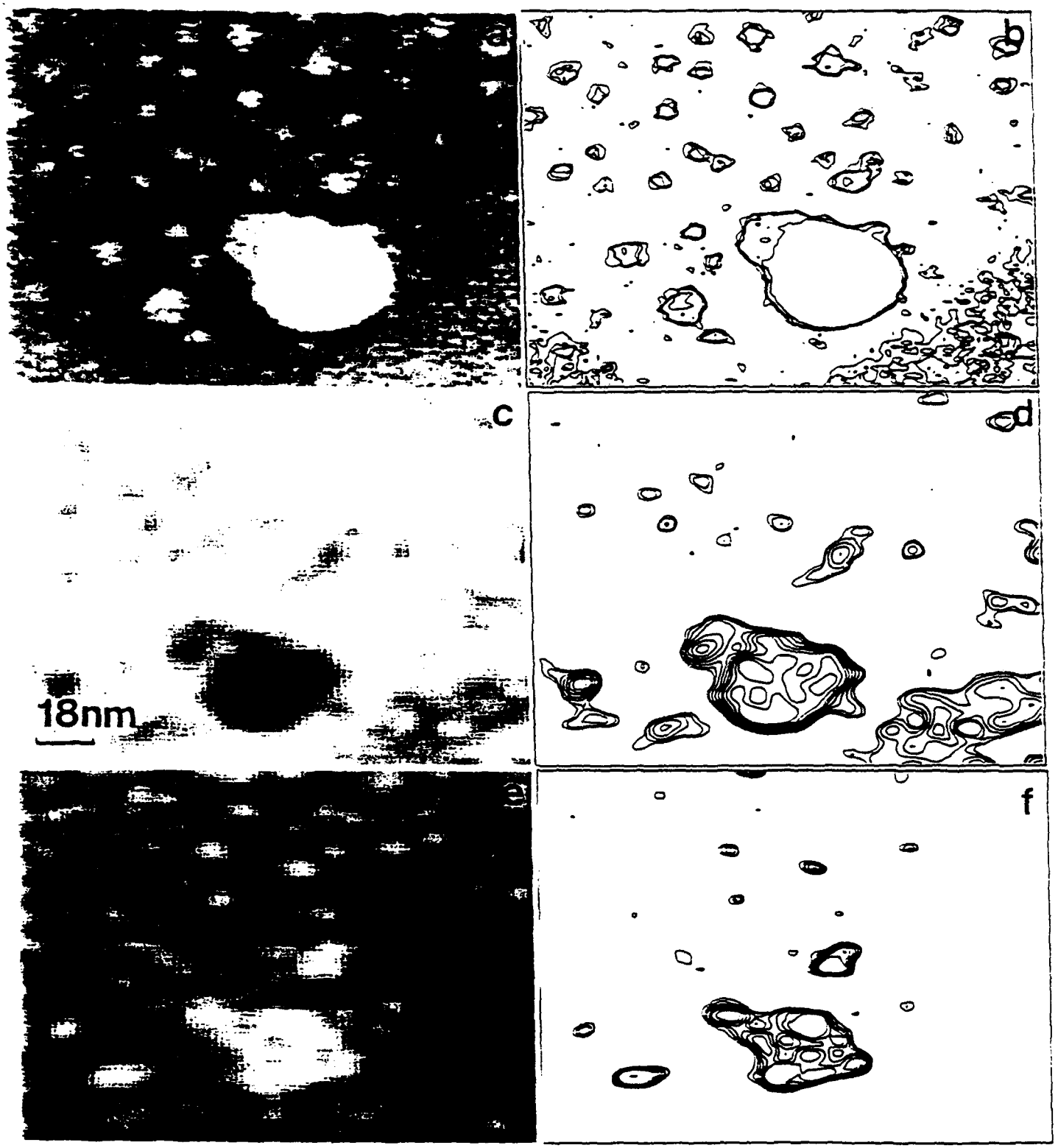

fig 2

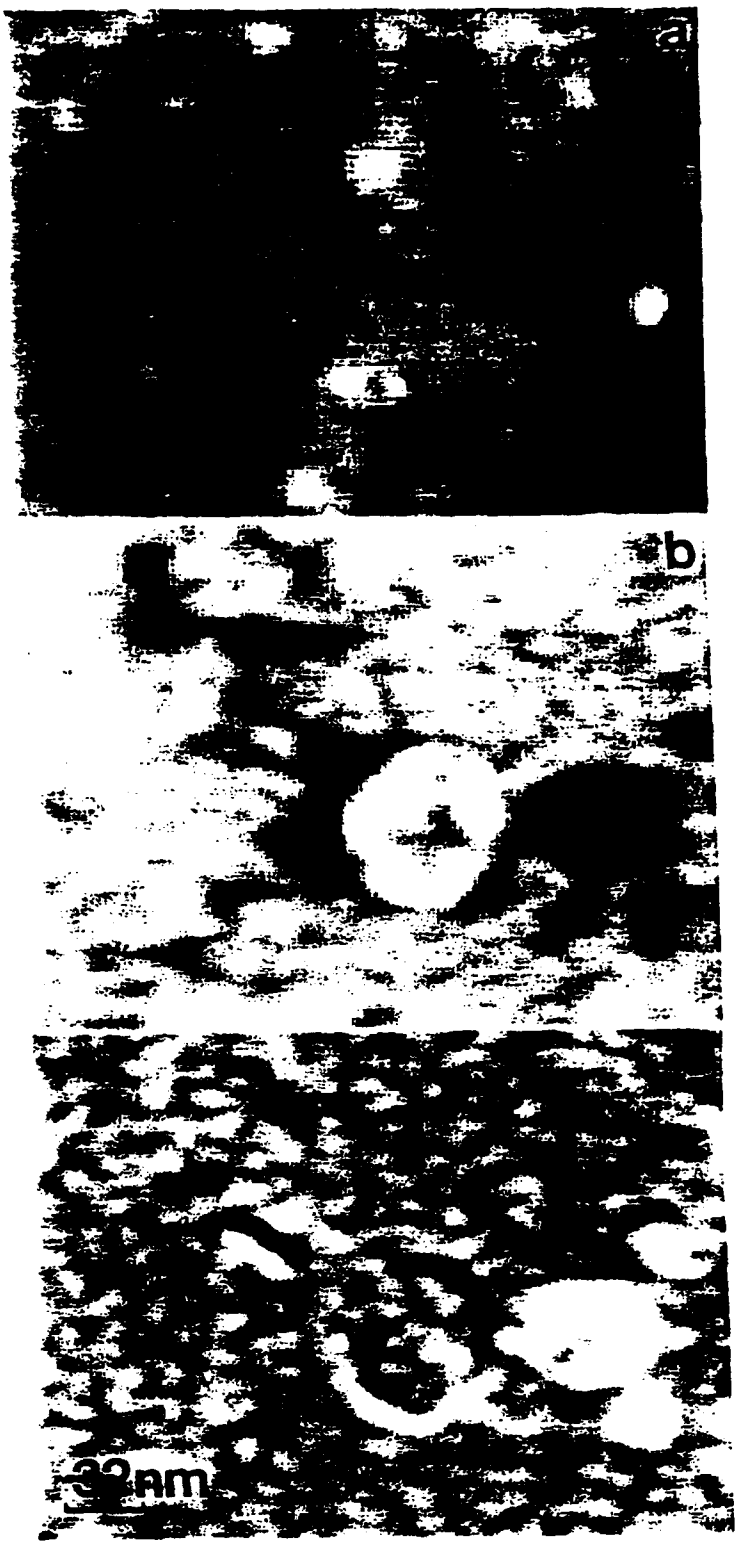

Fig 3

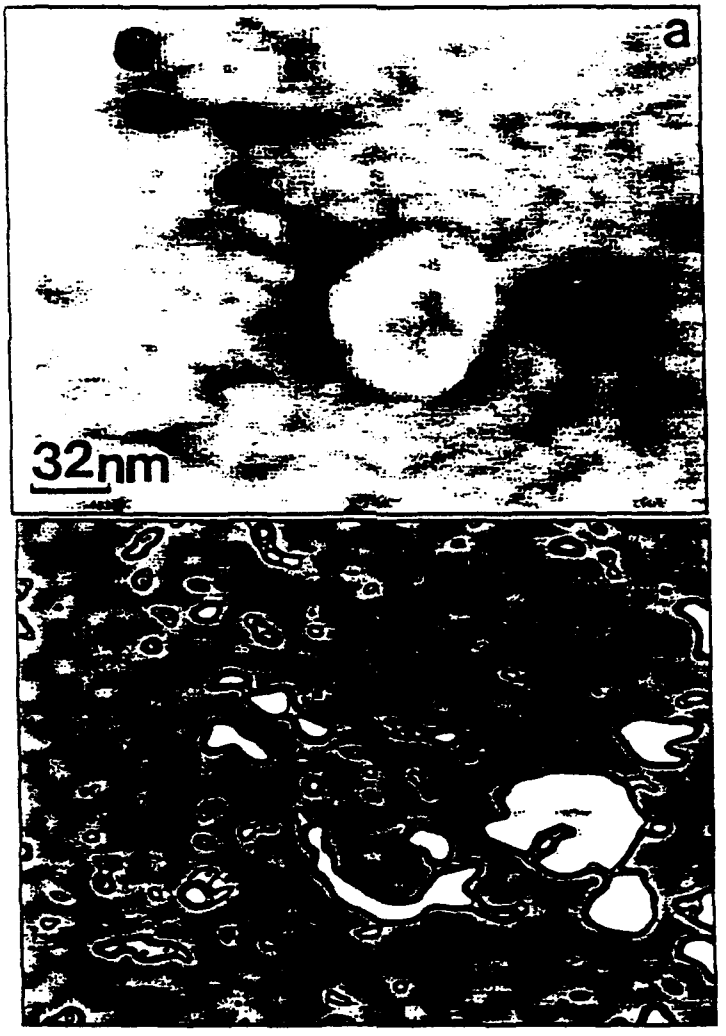

Fig 4

Monodisperse Island Size Distributions for Fe/CaF_2/Si(111)

K. R. Heim, G. G. Hembree, and M. R. Scheinfein
Box 871504
Department of Physics and Astronomy
Arizona State University, Tempe, AZ 85287-1504
(received 11/5/93)

Abstract

The initial stage of Fe island growth on CaF_2/Si(111) was studied with a nanometer lateral spatial resolution ultra high vacuum scanning electron microscope. A 60 minute deposition at a rate of 0.11 Å/min on near room temperature CaF_2/Si(111) substrates produced a relatively uniform distribution of islands that cover 23% of the substrate with an island density of 7.4×10^{12} islands/cm^2. This Fe/CaF_2/Si(111) system, with its narrow size distribution of 2.0 ± 0.3 nm diameter (non-ferromagnetic) Fe islands separated by distances less than the mean free path of conduction electrons in metals, is expected to exhibit giant magnetoresistance when covered with a noble metal.

PACS numbers: 61.16.Di, 61.80.Fe, 68.55.Bd, 75.50.Bb, 75.30.Pd

Submitted APL 11/5/93

Recent progress in the experimental study of the growth and characterization of metals on insulators has been motivated by expectations that these materials will improve upon our current solid state device technology. Components such as quantum-interference high-speed electron devices [1], triple-barrier resonant tunneling diodes [2], hot electron transistors [3], and metal-epitaxial insulator-semiconductor field-effect transistors [4] have been fabricated or proposed using metals, insulators, and semiconductors. Presently, the majority of solid state devices are fabricated using Si as the semiconducting material due to the existence of its native oxide, SiO_2. The lack of an atomically smooth SiO_2-Si interface does, however, impede the production of three dimensional Si-based devices. Rough interfaces not only decrease the mobility of carriers in devices, but can also destroy the three dimensional epitaxial ordering of subsequent depositions. CaF_2 has been considered as a suitable replacement for SiO_2 since it can be grown epitaxially and atomically smooth on Si(111) substrates [5]. A small lattice mismatch (0.6% at 298 K) between CaF_2 and Si, a relatively large band gap (12.1 eV) for electronic isolation, and a larger dielectric constant (6.8) than SiO_2 (3.9) for an increased electric field at the insulator-semiconductor device interface are but a few of the many reasons for considering CaF_2 as an obvious replacement for the native SiO_2 [5]. In addition, CaF_2 layers may be used as a buffer region such that devices utilizing highly reactive metals such as Fe are not able to form compounds with the Si substrate. The deposition of Fe on CaF_2/Si(111) would enable the fabrication of fully integrated electronic and magnetic devices on a single substrate. Magnetic sensors, high speed microwave waveguides [6], and non-volatile memories [6] are just three of the many applications which may result from constructing solid state devices using Fe, CaF_2, and Si.

For very slow growth rates the adsorbate topology is expected to approximate structures produced under equilibrium conditions. In this regime, the growth mode is controlled by surface energy imbalances. As Bauer has already set forth [7], a system in equilibrium can be characterized in terms of the surface energy of the adsorbate (γ_a), substrate (γ_s), and the interface between them (γ_i). When $\gamma_a + \gamma_i > \gamma_s$ the deposited material is not expected to spread evenly over the substrate's

surface. Fe and $CaF_2(111)$ are known to possess surface energies of 2475 erg/cm^2 [8] and 450-550 erg/cm^2 [9], hence, Fe island formation on CaF_2 is expected. We are interested in the formation of monodisperse transition metal island size distributions because ferromagnetic or paramagnetic granules embedded in a three-dimensional noble metal matrix have been shown to exhibit giant magnetoresistive behavior if the granules are properly spaced and smaller than some critical radius [10]. This leads to the natural extension whereby a two-dimensional array of isolated ferromagnetic particles, such as Fe islands on an insulating CaF_2 substrate, covered by a noble metal is expected to yield two-dimensional giant magnetoresistance (GMR) effects. In addition, since CaF_2 can be chemically altered by electron beam exposure [11], growth modes may be controlled for selected regions of the surface prior to metal deposition by modifying the surface composition with an electron beam. A further increase in electron irradiation and exposure to residual oxygen allows the CaF_2 to be used as an electron beam resist [11], thereby expediting the fabrication of nm-size and low dimensional magnetic devices.

In this letter, structural and magnetic measurements obtained during the initial stages of growth for the Fe/CaF_2/Si(111) system are reported. The growth and preparation conditions for the CaF_2/Si(111) substrates have been described in detail elsewhere [12]. Samples of 100 Å thick CaF_2/Si(111) [13] were cut into 3 mm discs with an ultrasonic drill. The samples were placed in an ultra high vacuum (UHV) chamber which was baked at 170 °C for more than 24 hours resulting in a base pressure less than 5×10^{-11} mbar. Our vacuum chamber is equipped with standard surface science preparation, deposition, and analysis instrumentation [14], an *in situ* surface magneto-optic Kerr light scattering station and is mechanically connected to a modified Vacuum Generators HB501-S UHV-STEM. This UHV instrument has been constructed for *in situ* processing and subsequent surface observation with nanometer resolution secondary electron (SE) and Auger electron microscopy.

SE microscopy (100 keV and ~10 pA incident beam current), using a through-the-lens detection scheme [15], performed before and after (radiatively) annealing the CaF_2/Si(111) substrates at 300 °C for 60 minutes, revealed that areas of obvious surface contamination were not reduced by heating. Broad-beam Auger electron spectroscopy (AES) displayed no statistically significant changes in the chemical composition of the CaF_2 surface after annealing for 60 minutes at temperatures up to 400 °C. Higher annealing temperatures do, however, produce significant changes in the surface morphology. These changes have been observed with SE microscopy. An unannealed CaF_2/Si(111) specimen is shown in Fig. 1a. The saw-toothed step edge visible in Fig. 1a is a typical surface feature of the many samples observed. Fig. 1b indicates that, after a 60 minute, 400 °C anneal, numerous, almost triangularly arranged pits are formed. These morphological changes may have resulted from the relief of stresses present during the growth of the CaF_2 [16]. In order to prevent severe surface modifications (pitting) during cleaning, the substrates were either annealed for 60 minutes at 300 °C or for 24 hours at 170 °C prior to the Fe deposition. Obvious contamination occupied small, localized regions of the total CaF_2 surface area (10-30%), such that Fe island size distributions could be determined from regions between the contaminated areas. Fe was deposited using an electron beam evaporator. The evaporation rate was confirmed by Rutherford backscattering, AES, and quartz-crystal microbalance techniques. The pressure during growth was typically less than 2×10^{-9} mbar with the substrates held at either room temperature or 140 °C.

The initial stage of Fe/CaF_2 growth proceeds by three dimensional islanding. Fig. 1c is an example of a 60 minute Fe deposition at a rate of 0.11 Å/min on a room temperature substrate. The relatively even distribution of 2.0 nm diameter Fe islands on a 100 Å thick CaF_2(111) surface is clearly displayed. Inset in Fig. 1c is the corresponding Fe island size distribution. Particle size analysis of the SE images revealed no statistical difference between the diameters and spatial distribution of Fe islands grown on 140 °C and room temperature CaF_2/Si(111) substrates. A post-growth anneal of 140 °C on room temperature grown films did not produce a noticeable

change in the Fe island size distribution. Statistical analysis performed on a large variety of images yielded the following information for a 60 minute deposition of Fe (0.11 Å/min) on room temperature or 140 °C CaF_2/Si(111) substrates: (1) An average Fe island diameter of 2.0 ± 0.3 nm; (2) A range of Fe island diameters where 85% of the population will lie within 2.0 ± 1.0 nm; (3) An average Fe island separation of 2.0 ± 0.4 nm; (4) A 23% coverage of CaF_2(111) with Fe islands; (5) The number of Fe islands per unit area is 7.4×10^{12} islands/cm^2; (6) The mean distance between Fe island centers is approximately 3.7 ± 0.6 nm; (7) No geometric ordering of the islands was observed based on fast Fourier transform image analysis.

A simple energy calculation indicates that a hemispherically shaped, unstressed, and magnetically ordered Fe particle must contain a single magnetic domain for diameters on the order of a few tens of nanometers. This transition is a result of domain formation becoming energetically unfavorable as the magnetic particle becomes smaller due to the domain boundary energy becoming a large percentage of the total energy. The islands observed in Fig. 1c are smaller than the critical single domain size and separated by less than the mean free path of conduction electrons in metals (near 30 nm at room temperature for Cu [17]). These properties make this system of nm-size Fe islands on an insulator, when covered by a noble metal, an excellent candidate for room temperature GMR studies [10,18].

In situ surface magneto-optic Kerr effect (SMOKE) measurements were not sensitive enough to detect a magnetic signal for this metal/insulator system. Our facility is capable of detecting magnetization variations resulting from Fe thickness changes as small as 0.22 Å for ultra thin films of fcc Fe/Cu(100) [14]. Therefore, since no signal was detected, we conclude that ferromagnetism in the island array is not present. A simple Langevin paramagnetism calculation indicated that a superparamagnetic signal would not be apparent using our maximum applied magnetic field of approximately 1000 Oe for islands with a diameter less than 2.8 nm, hence, we are not able to distinguish between superparamagnetic and nonmagnetic behavior. This would imply that a larger

field and more sensitive detection equipment (as with a SQUID) is necessary to observe the expected Fe island superparamagnetic behavior. Furthermore, AES measurements exhibited residual oxygen contamination within the CaF_2 surface layers prior to Fe deposition. This contamination could alter the magnetic response of the Fe film if some species of Fe_xO_y forms. The various combinations of Fe_xO_y are known to display ferromagnetic, antiferromagnetic, and ferrimagnetic behavior [19] and thus cannot be overlooked as a possible explanation for the lack of observed magnetic response.

Fig. 1d displays a SE image of Fe islands on a 100 Å thick CaF_2/Si(111) surface and an oxidized Si(111) surface. The oxidized Si region is visible because the CaF_2 had locally lifted off of the Si crystal, perhaps during 3 mm disc preparations. The existence of Fe islands on the Si region, while also possessing a similar diameter as those on the CaF_2 region, suggests that the thermodynamically favorable reaction of silicide formation did not occur. It appears that the Si had been chemically changed into an insulating, lower surface energy, and less reactive SiO_2 surface. The difference of Fe mobility in the two distinct regions is made apparent by the difference in mean inter-island separation. In addition, the (position) stability of the Fe islands shown in Fig. 1d was monitored as a function of electron beam exposure. A SE image formed by subtracting two images of the same area taken after a total electron dose of 6000 C/cm^2 revealed that the Fe islands remained fixed in position on both the CaF_2 and the SiO_2 regions.

Fe is not expected to form compounds with CaF_2. Thermochemical considerations reveal that Fe is much less reactive with CaF_2 than with NaCl [20]. Wassermann et al. and Matthews [21] found that the Fe/NaCl system does not initiate compound formation at the interface. These two considerations imply that there is a high probability of maintaining chemically distinct Fe and CaF_2 regions when Fe is deposited under UHV conditions on CaF_2 substrates held at or below 700 °C. This does not preclude the existence of other channels for Fe compound formation. For example, it is possible that the 100 Å thick CaF_2 does not completely inhibit iron silicide formation.

Pinholes, located within the CaF_2 film, may be a conduit for mass transfer. Although black, round-shaped regions (pinholes) were observed via SE microscopy, the absence of denuded zones surrounding these black areas and the resulting uniform Fe island distribution over the complete CaF_2 surface seems to suggest little, if any, chemical reactivity. Nonetheless, based on a hemispherical model of Fe islands, particle size analysis implies that at least 20% of the Fe is unaccounted for. This deficiency may be attributed to the model employed. Cylindrical shaped islands with an axis length equal to the radius would enclose a volume 50% larger than a hemispherical island of the same radius. Certainly, islands which are slightly hemispherical at the top and cylindrical at the base would indicate that all the Fe is, in fact, accounted for.

A narrow size distribution of 2.0 nm diameter Fe islands was grown on CaF_2/Si(111) surfaces held at or near room temperature. This system, an arrangement of possibly single domain particles separated by less than the mean free path of conduction electrons in metals, is an exciting new candidate for GMR studies. Further work must be completed to determine whether the Fe is; magnetic, affected by the inherent oxygen contamination, chemically separated from the Si, and controllable so that various size islands may be formed by changing the deposition rate, substrate temperature, substrate surface energy, and quantity of Fe deposited.

The authors wish to acknowledge thoughtful discussions with D. Loretto, J. Venables, J. Drucker, P. Bennett and W. Petuskey. We are also indebted to D. Loretto of Lawrence Berkeley Laboratory for supplying the CaF_2/Si(111) samples. This work is supported by the Office of Naval Research under grant No. N00014-93-1-0099 and the National Science Foundation under grant No. DMR 89-14761. The microscopy was performed at the National Science Foundation supported Center for High Resolution Electron Microscopy at Arizona State University, grant No. DMR-91-15680.

References

1 T. Sakaguchi, M. Watanabe, and M. Asada, IEICE Trans. **E 74**, 3326 (1991).

2. M. Watanabe, T. Suemasu, S. Muratake, and M. Asada, Appl. Phys. Lett. **62**, 300 (1993).

3. S. Muratake, M. Watanabe, T. Suemasu, and M. Asada, Electronics Letters **28**, 1002 (1992). T. Suemasu, M. Watanabe, M. Asada, and N. Suzuki, Electronics Letters **28**, 1432 (1992).

4. T. P. Smith, J. M. Phillips, W. M. Augustyniak, and P. J. Stiles, Appl. Phys. Lett. **45**, 907 (1984).

5. L. J. Schowalter and R. W. Fathauer, CRC Critical Reviews in Solid State and Materials Sciences **15**, 367 (1989).

6. E. Schloemann, R. Tustison, J. Weissman, H. J. Van Hook, and T. Varitimos, J. Appl. Phys. **63**, 3140 (1988).

7. E. Bauer, Z. Krist. **110**, 372 (1958).

8. F. R. de Boer, R. Boom, W. C. M. Mattens, A. R. Miedema, and A. K. Niessen, *Cohesion in Metals Transition Metal Alloys* (North-Holland Elsevier Science Publishers, NY, 1988).

9. J. J. Gilman, J. Appl. Phys. **31**, 2208 (1960). G. C. Benson and T. A. Claxton, Can. J. Phys. **41**, 1287 (1963). P. W. Tasker, J. Phys. (Paris) **41**, C6-488 (1980).

10. J. Q. Xiao, J. S. Jiang, and C. L. Chien, Phys. Rev. Lett. **68**, 3749 (1992).

11. T. R. Harrison, P. M. Mankiewich, and A. H. Dayem, Appl. Phys. Lett. **41**, 1102 (1982). P. M. Mankiewich, H. G. Craighead, T. R. Harrison, and A. H. Dayem, Appl. Phys. Lett. **44**, 468 (1984). M. Scheinfein and M. Isaacson, J. Vac. Sci. Technol. **B 4**, 326 (1986).

12. C. A. Lucas and D. Loretto, Appl. Phys. Lett. **60**, 2071 (1992).

13. The CaF_2/Si(111) samples were kindly provided by D. Loretto of Lawrence Berkeley Laboratory.

14. K. R. Heim, S. D. Healy, Z. J. Yang, J. S. Drucker, G. G. Hembree, and M. R. Scheinfein, J. Appl. Phys. **74**, (in press) (1993).

15. G. Hembree, J. Drucker, C. Luo, M. Krishnamurthy, and J. Venables, Appl. Phys. Lett. **58**, 1890 (1991). G. G. Hembree and J. A. Venables, Ultramicroscopy **47**, 109 (1992). J. Liu, G. G. Hembree, G. E. Spinnler, and J. A. Venables, Surface Science Lett. **262**, L111 (1992). J. Liu, G. G. Hembree, G. E. Spinnler, and J. A. Venables, Catalysis Lett. **15**, 133 (1992). P. Kruit and J. A. Venables, Ultramicroscopy **25**, 183 (1988). P. Kruit, Adv. Opt. Electron Microsc. **12**, 93 (1991).

16. Private communication with D. Loretto: Bright field transmission electron microscopy performed on the CaF_2/Si(111) samples revealed a non uniform distribution of line defects at the CaF_2-Si(111) interface. This is an indication that stress relief occurred during the CaF_2 growth. In comparison, an unrelaxed film will display a parallel array of line defects corresponding to the original steps on the Si(111) surface.

17. C. Kittel, *Introduction to Solid State Physics, fourth edition* (John Wiley & Sons, 1971), page 259.

18. C. L. Chien, J. Appl. Phys. **69**, 5267 (1991). A. E. Berkowitz, J. R. Mitchell, M. J. Carey, A. P. Young, S. Zhang, F. E. Spada, F. T. Parker, A. Hutten, and G. Thomas, Phys. Rev. Lett. **68**, 3745 (1992). A. E. Berkowitz, J. R. Mitchell, M. J. Carey, A. P. Young, D. Rao, A. Starr, S. Zhang, F. E. Spada, F. T. Parker, A. Hutten, and G. Thomas, J. Appl. Phys. **73**, 5320 (1993).

19. J. Crangle, *Solid State Magnetism* (Edward Arnold, 1991), page 187.

20. Calculations were made to determine the change in the Gibbs energy during formation reactions of Fe with CaF_2 and Fe with NaCl (both at 700 K and 1000 K). The results indicate that a chemical reaction beginning with gaseous reactants is more likely than those beginning with solid reactants, although both cases favored an Fe-NaCl reaction over an Fe-CaF_2 reaction. This, coupled with the fact that NaCl has a much higher vapor pressure than CaF_2 (3.2×10^{-7} vs. 5.4×10^{-20} at 700 K and 3.4×10^{-2} vs. 1.9×10^{-10} at 1000 K,

with pressure in mbars), suggests that a gaseous reaction involving NaCl is more probable than that with CaF_2.

21. E. F. Wassermann and W. Sander, J. Vac. Sci. Technol. **6**, 537 (1969). J. W. Matthews, J. Vac. Sci. Technol. **3**, 133 (1966).

CAPTIONS:

Fig. 1a SE image of an unannealed CaF_2/Si(111) surface. The contrast is due to a saw-tooth step edge which commonly appeared on these surfaces.

Fig. 1b SE image of a CaF_2/Si(111) sample that was annealed for 60 minutes at 400 °C. Morphological changes are apparent by the many triangularly oriented pits now covering the entire CaF_2 surface.

Fig. 1c A 60 minute, room temperature Fe deposition at a rate of 0.11 Å/min on CaF_2/Si(111) produces a monodisperse Fe island distribution. The results of statistical analysis performed on high resolution SE images is quoted in the text. The ordinate and the abscissa of the inset histogram are "number of Fe islands" and "diameter of Fe islands (nm)", respectively. The vertical scale varies from 0 to 25 while the horizontal scale extends from 0 to 5.

Fig. 1d A SE image formed under the same conditions as Fig. 1c but in a region where some CaF_2 has locally lifted off the Si(111) substrate. Fe islands are visible on the CaF_2/Si(111) surface (top), the oxidized Si(111) surface (bottom), and the inverted CaF_2 surface (right). A difference in Fe mobility can be observed by comparing the mean inter-island separation between the top and bottom regions.

(a)

Absolute Magnetometry at nm Transverse Spatial Resolution: STEM Holography of Thin Cobalt Films

Marian Mankos, M. R. Scheinfein and J. M. Cowley
Department of Physics and Astronomy, Arizona State University
Tempe, AZ 85287-1504, USA

Abstract:

A new method for the absolute measurement of magnetization at nanometer spatial resolution in magnetic thin films has been developed. A biprism placed in the illumination system of a scanning transmission electron microscope allows the operation of two distinct holography modes. The absolute mode displays a linear change in phase difference for regions of constant magnetization and thickness and the slope determines the magnitude of magnetization. The differential mode displays a constant value of phase difference in these regions allowing a simple and straightforward determination of domain wall profiles. Micromagnetic structure extracted from identical areas of thin Co films is compared using the new holography modes, Differential Phase Contrast Lorentz microscopy and conventional Fresnel Lorentz microscopy in the same instrument.

PACS : 75.25.+Z, 75.60.-d, 42.40.Kw, 07.60.Ly

(Submitted J. Appl. Phys)

I. Introduction

Synthesized magnetic structures and devices are attracting scientific interest due to their many unique and unusual properties which are often governed by their micromagnetic structure. Multilayer structures composed of magnetic layers separated by nonmagnetic spacers[1], granular giant magnetoresistance films composed of magnetic and nonmagnetic metals[2], or Fe-Si and Fe-Zr base nanocrystalline soft magnetic alloys[3] exhibit phenomena whose interpretation requires knowledge of the micromagnetic structure at nanometer scale. At present a variety of techniques for the observation of magnetic structure, including the Bitter pattern method[4], magneto-optical methods[5], X-ray and neutron topography[6,7], magnetic force microscopy[8] and electron microscopy[9], are available. Electron microscopy is the only method to date capable of delivering structural information at nanometer (point) resolution. Various modes of Lorentz microscopy[10,11], revealing the in-plane component of magnetization as well as the local (microcrystalline) microstructure, have been implemented in a dedicated scanning transmission electron microscope (STEM). The improved performance of electron microscopes equipped with high brightness and coherent field emission sources, the availability of efficient new detection systems (CCD cameras), and fast image processing techniques have facilitated a wave of new applications of electron holography[12,13]. In electron holography, both the amplitude and phase of the transmitted electron waves are recorded whereas in conventional electron microscopy only the modulus of the wave amplitude is recorded. The phase shift in the specimen which contains valuable information about the local distribution of scalar and vector potentials can be retrieved from an electron hologram[14,15]. We use this STEM electron holography to explore the micromagnetic structure of cobalt thin films e-beam sputtered on holey amorphous carbon films. Since these films have well known micromagnetic structure[16], a comparison with the magnetic structure contrast obtained by the new holography modes is made with well-known classical Lorentz microscopy techniques performed simultaneously on the same samples in the same STEM.

II. Technique and Theory

In off-axis STEM holography[17,18] an electron biprism[19], a conductive wire about 0.5μm in diameter held at a constant potential, is placed in the illuminating system of a STEM (VG Instruments HB 5) as shown in Fig.1a. The wave emitted from the electron source is split by the biprism into two wave packets resulting in the formation of two identical coherent electron probes at the specimen. If the objective lens is operated at a large defocus, a hologram, the interference between the two coherent waves, appears as a fringe-modulated image in the detector plane. The wave vectors and hence the fringe spacing are determined by the electron beam voltage and the voltage applied to the biprism wire. With a defocused objective lens, a large area of the specimen is illuminated and the beam is held stationary (no scanning). The hologram is recorded on a slow-scan CCD camera and reconstructed in the conventional way as in TEM holography[20]. A fast Fourier transform of the hologram yields a diffractogram. The diffractogram has two sidebands whose separation is dependent upon the spacing of the fringes. This side-band separation in off-axis holography allows the removal of the conjugate image present in the hologram. One sideband is isolated and its inverse Fourier transform reveals the amplitude and the phase of the complex image wave. Magnetic thin films are strong phase objects with phase differences of $\geq 10\pi$ rad common, therefore we analyze only the reconstructed phase image. However, the phase retrieval process of inverse transformation only delivers the principal values in the interval $(-\pi,+\pi)$. Thus the phase images must be further processed in order to unwrap the periodicity by successive phase additions or subtractions of 2π.

In the following we present the first experimental results of electron holography obtained in a STEM. The contrast in a STEM electron hologram can be explained by analyzing the wave paths from the source through the specimen to the detector plane. A single wave emerges from the electron source and is split by the biprism, forming two waves. The biprism thus forms two coherent virtual sources Q' and Q", as shown in Fig.1a. There are two different modes of STEM holography, an absolute mode and a differential mode. In the absolute mode, one wave packet passes through vacuum and the other passes through the specimen as shown in Fig.1b. This mode has analogy with TEM electron holography. In the differential mode, both waves traverse the specimen as shown in Fig.1c and interfere in the detector plane. Within the region of overlap in the detector plane the intensity distribution becomes a modulated pattern of cosine fringes

$$I_D(\mathbf{r}) = |a_A(\mathbf{r})\, e^{2\pi i\, \mathbf{k}_A \mathbf{r}} + a_B(\mathbf{r})\, e^{2\pi i\, \mathbf{k}_B \mathbf{r}}|^2 =$$
$$= |a_A(\mathbf{r})|^2 + a_B(\mathbf{r})|^2 + 2|a_A(\mathbf{r})|\,|a_B(\mathbf{r})| \cos[2\pi(\mathbf{k}_A - \mathbf{k}_B).\mathbf{r} + (\varphi_1 - \varphi_2)], \qquad (1)$$

where $\mathbf{k}_A$ and $\mathbf{k}_B$ are the wave vectors of the two interfering waves and $a_A(\mathbf{r})$, $a_B(\mathbf{r})$ are the corresponding amplitudes. The interference pattern contains the amplitude modulation and the phase difference of the waves. With no specimen present the phase shift $\varphi_1 - \varphi_2 = 0$ and the interference results in a set of up to several hundred parallel fringes covering the detector plane. If a specimen is present, the two waves suffer additional phase shifts[21] due to the electromagnetic fields present. Consider the phase difference between paths QAD and QBD, schematically shown in Fig.2 :

$$\varphi_1 - \varphi_2 = 2\pi \oint_{QADBQ} \mathbf{k}\,d\mathbf{l} = \frac{2\pi}{h}\oint \mathbf{p}\,d\mathbf{l} = \frac{1}{\hbar}\oint (m\mathbf{v} - e\mathbf{A})\,d\mathbf{l}$$

$$= \frac{1}{\hbar}\oint m\mathbf{v}\,d\mathbf{l} - \frac{e}{\hbar}\iint \nabla \times \mathbf{A}\,d\mathbf{S} = \frac{1}{\hbar}\oint m\mathbf{v}\,d\mathbf{l} - \frac{e}{\hbar}\iint \mathbf{B}\,d\mathbf{S}, \qquad (2)$$

where $\mathbf{p}=\hbar\mathbf{k}$ is the canonical momentum, $\mathbf{A}$ is the vector potential, $\mathbf{B}$ the magnetic field and S the area enclosed by the path QADBQ. In thin magnetic films the phase shift is dominated by the second term, the magnetic phase shift. The phase difference is thus proportional to the magnetic flux enclosed by the two beam paths as they traverse the specimen. The enclosed area depends upon the separation of the two virtual point sources which in turn depends upon the excitation of the biprism.

III. Experiment

A. Absolute Mode

In the absolute mode, well known from TEM holography, one of the waves passes through vacuum and the other through the specimen (Fig.1b). The phase difference is measured always with respect to vacuum and the reconstructed phase difference represents the absolute phase shift caused by (the enclosed area of) the specimen . In a domain with uniform magnetization located at a sharply defined edge, the phase will change linearly with

increasing distance from the edge as the enclosed flux increases, $\iint \mathbf{B}d\mathbf{S} \cong B_n xt$, where B_n is the magnetization component normal to the plane defined by $\mathbf{k}_A$ and $\mathbf{k}_B$, t is the constant thickness and x is the distance from the edge. The gradient of the phase will determine the magnitude and direction of the magnetization in the domain (to within an overall sign). In the following analysis we neglect the variation of the magnetic film thickness over the analysis region (typical thickness variations are less than a few nm over the ten micron field of view) as well as the phase shift caused by the mean inner potential of the sample. We neglect variations due to the inner potential since it only adds a constant to the phase and the quantitative magnetic information is derived from the gradient of the phase. Any phase changes caused by the inner potential (due to thickness variations) are small (~0.2 rad/nm for cobalt[15] when compared to the absolute phase changes caused by the magnetic field (~10π rad). Fig.3 illustrates the absolute mode of STEM holography. Fig.3a shows the recorded off-line hologram from the thin Co film; evident are the dual images of the edge and domain wall (bright line) and the cosine fringes. The reconstructed phase image in Fig.3b displays a wrapped phase image where the maximum phase change is limited from -π to +π in each band. A three-dimensional unwrapped phase image of the marked region is shown in Fig.3c. The zero phase in vacuum is evident in the flat region in the upper left part of Fig.3c. The linear phase change of 45.9±2.0 mrad/nm indicates that the film is of nearly uniform thickness and uniform saturation magnetization-thickness of 302±9 kOe-nm. This agrees favorably with the accepted value of the saturation magnetization in Co for a 17 nm thick film[22]. The fact that we can make an absolute determination of the magnetization rests upon the knowledge that the fringe spacing is absolutely calibrated. Also evident in Fig.3c is the presence of a domain boundary (108.3±2.0°). This structure is consistent with the presence of 71°, 109° and 180° domain boundaries on ⟨110⟩ surfaces in fcc lattices[23]. The proposed magnetization structure is shown in Fig.3d and will be further verified in Fig.4. The main reasons for measurement uncertainty were magnification calibration and thickness measurement.

In order to examine the unique contrast revealed by STEM holography we compare the micromagnetic structure extracted from the data in Fig.3 with two accepted contrast modes performed in the same STEM instrument without any special adjustment. The marked area in Fig.4 corresponds to the region of the sample analyzed in Fig.3. In Figs.4a,b Differential Phase Contrast (DPC) Lorentz microscopy[24] and in Figs.4c,d Fresnel contrast Lorentz microscopy images of the same region of the same cobalt film are shown. In the DPC mode, images of domains of uniform magnetization can be identified

as areas of bright or dark contrast[11] and the vector nature of the local magnetization can be revealed. Fig.4a shows the projected magnetization on the arrow indicated, where white (black) corresponds to the magnetization parallel (antiparallel) to the arrow. Similarly, Fig.4b illustrates the component of the magnetization projected along the orthogonal in-plane axis as indicated. The orientation of the domains can be extracted straightforwardly from these images and agrees with the proposed structure in Fig.3d. In the Fresnel contrast mode, images of domain walls appear as either black or white bands[9] for the images recorded in the underfocus (Fig.4c) and overfocus (Fig.4d) conditions. Note that the contrast of the domain walls changes from black to white and vice versa when going through focus. We can clearly correlate the domain wall structure emanating from the kink in Fig.4c,d (black in Fig.4c, white in Fig.4d) as the same wall which divides the two regions of uniform magnetization in Fig.4a,b as well as the structure identified as regions of uniform magnetization in the reconstructed hologram in Fig.3c. What we are not able to extract from Fig.4 is the absolute value of magnetization: this would require the accurate measurement of the deflection angle caused by the magnetization in the DPC mode. However, this angle is too small ($\sim 10^{-5}$rad) for an accurate measurement in the electron microscope. In the Fresnel mode it is even more difficult to evaluate the magnitude of the magnetization since it requires an image deconvolution of the domain wall with an exact value of defocus and a known wall profile.

The holographic technique allows the extraction of quantitative information about the magnetic structure at high spatial resolution and therefore significantly expands the abilities of STEM as a tool for investigating magnetic materials. Since the Fresnel mode is still the simplest and fastest way for domain structure observation and the DPC mode provides necessary information about the magnetization orientation in the particular domains, the three techniques used in conjuction in the same instrument provide all the necessary information for complete, calibrated micromagnetic structure determination.

B. Differential Mode

The differential mode of STEM holography has no analogy in TEM holography. Both of the split electron waves pass through the specimen. Here, the two virtual sources are separated by a very small distance when projected onto the sample, typically several tens of nm (Fig.1c). This separation can be varied not only by changing the voltage applied to the

biprism, but also by simply changing the excitation of the condensor and/or objective lenses. The size of the illuminated area which contributes to the phase difference (through the magnetic flux), is approximately constant for every point in the detector plane (illumination is almost parallel). The sensitivity to local changes in the phase is limited in this mode by the separation of the virtual sources. Since the resolution limit in reconstructed holograms is about 2-3 times the cosine fringe spacing[20], a sufficient condition for maintaining the resolution is that the separation of the two dual images in the recorded hologram be less than approximately 3 fringes. If this condition is met, the reconstructed phase difference becomes a direct measure of the local magnetic structure. In this mode domains with constant magnetization are represented as regions of constant phase difference, in contrast to the absolute mode, where the same domains would appear as regions of linear phase difference.

In Fig.5 we show images of a domain wall in the thin Co film, and compare the information retrievable from the differential holography, DPC and Fresnel modes. Figs. 5a-c show the reconstructed phase, processed DPC, and Fresnel images of the domain wall. Figs.5d-f are the corresponding three-dimensional plots of the domain wall profiles for each of the cited methods respectively, and Figs. 5g-i show the domain wall magnetization profiles extracted in a direction perpendicular to the domain wall. The Fresnel mode profile does not allow any direct interpretation of the domain thickness or the magnetization distribution across the domain wall. Comparing the wall profiles from the differential holography and DPC modes, we readily see that the latter displays strong ripple due to scattering contrast from small particles, hence significantly complicating the determination of the wall profile. This ripple is suppressed in the holography mode, because the phase changes caused by these effects are small when compared to the absolute change of phase from the magnetic flux. The residual slope within the two domains in the phase image is due to the complicated magnetization structure along the domain wall. The width of the domain wall (20-80% of maximum value), as determined from the line scans in Fig.5, agrees in both modes quite well : 104 ± 4 nm (differential holography) and 98 ± 7 nm (DPC).

IV. Conclusions

We have developed a new method for the absolute measurement of magnetization in thin magnetic films by STEM holography. The absolute mode of STEM holography displays a linear change in phase difference for regions with constant magnetization and the slope determines the absolute value and direction of magnetization. The differential mode of STEM holography displays a constant value of phase difference for regions with constant magnetization, which simplifies the identification of magnetic structures in the specimen. In addition, no edge or hole is necessary since neither wave packet need pass through vacuum. These results illustrate the power of combining several STEM based techniques for the investigation of magnetic microstructure. The Fresnel mode is best used for fast and simple recognition of magnetic microstructure, the DPC mode is best used for magnetization orientation in domains and most importantly, the holography modes allow absolute determination of magnetization, the determination of equimagnetization lines in domains and a straightforward determination of domain wall profiles. Taking into account the high spatial resolution of a STEM instrument, STEM holography provides a valuable tool for quantitative investigations of magnetic structures at the nanometer level.

V. Acknoledgements

This work was supported by the NSF under grant DMR-9110386, and the Office of Naval research under grant #N00014-93-1-0099 . The electron microscopy was performed in the Center for High-Resolution Electron Microscopy at Arizona State University supported by the NSF grant DMR91-15680. We are grateful to A. Higgs for the setup of the biprism and flawless operation of the HB5 microscope, M.R. McCartney and P. Perkes for help with the hologram reconstruction and image processing and Dr. J.K. Weiss of Emispec Systems for creative data acquisition software.

References

1 M.N. Baibich, J.M. Broto, A. Fert, F. Nguyen Van Dau, F. Petroff, P. Etienne, G. Creuzet, A. Friederich and J. Chazelas, Phys. Rev. Lett. **61** (1988) 2472

2 D.H. Mosca, F. Petroff, A. Fert, P.A. Schroeder, W.P. Pratt, Jr. and R. Laloee, J. Mag. Mag. Mat. **94** (1991) L1

3 Y. Yoshizawa, S. Oguma and K. Yamauchi, J. Appl. Phys. **64** (1988) 6044

4 F. Bitter, Phys. Rev. **38** (1931) 1903

5 M.J. Freiser, IEEE Trans. Mag. vol. **Mag-4** (1968) 152

6 A.R. Lang, Acta Crystallogr. **12** (1959) 249

7 M. Schlenker, J. Linares-Galvez and J. Baruchel, Philos. Mag. **B37** (1978) 1

8 R. Allenspach, H. Salemink, A. Bischof and E. Weibel, Z. Phys. **B67** (1987) 125

9 M.E. Hale, H.W. Fuller and H. Rubinstein, J. Appl. Phys. **30** (1959) 789

10 N.H. Dekkers and H. de Lang, Optik **41** (1974) 1

11 J.N. Chapman, J. Phys D: Appl. Phys. **17** 9191984) 623

12 D. Gabor, Nature **161** (1948) 777

13 A. Tonomura, J. Mag. Mag. Mat. **35** (1983) 963

14 X. Zhang, D.C. Joy, Y. Zhang, T. Hashimoto, L. Allard and T.A. Nolan, Ultramicroscopy **51** (1993) 21

15 M. Gajdardziska-Josifovska, M.R. McCartney, W.J. de Ruijter, David J. Smith, J.K. Weiss and J.M. Zuo, Ultramicroscopy **50** (1993) 285

16 M. Mankos, J.M. Cowley, R.V. Chamberlin, M.R. Scheinfein and J.D. Ayers, Proc. 51st Annual Meeting of the Microscopy Society of America (1993) 1026

17 E.N. Leith and J. Upatnieks, J. Opt. Soc. Am. **52** (1962) 1123

18 J.M. Cowley, Ultramicroscopy **41** (1992) 335

19 G. Möllenstedt and H. Düker, Z. Phys. **145** (1956) 377

20 H. Lichte, in Advances in Optical and Electron Microscopy, vol. **12** (1991) 25

21 Y. Aharonov and D. Bohm, Phys. Rev. **115** (1959) 485

22 B.D. Cullity, in "Introduction to Magnetic Materials", Addison-Wesley Publishing Co. (1972) 617

23 D.J. Craik and R.S. Tebble, in Ferromagnetism and Ferromagnetic Domains", North-Holland Publishing Co. (1965) 157

24 S. Kraut and J.M. Cowley, Microscopy Research and Technique **25** (1993) 341

Figure Captions

Figure 1 : a - Electron-optical set up and ray diagram for off-axis STEM holography. Ray diagrams for the absolute (b) and differential (c) modes of STEM holography.

Figure 2 : Schematic diagram for the calculation of phase difference which give magnetic contrast in the phase image.

Figure 3 : The absolute mode of off-axis STEM holography.
a - Recorded hologram of a thin cobalt film.
b - Wrapped phase image reconstructed from the hologram.
c - Three-dimensional unwrapped phase reconstruction plot of the selection marked in Fig.3b.
d - Proposed domain structure near the kink in the film.

Figure 4 : Classical Lorentz microscopy of the same region as in Fig.4.
a,b - DPC images with magnetization projected along orthogonal axes, as indicated by the arrow.
c,d - Fresnel images acquired in underfocus (c) and overfocus (d) condition.

Figure 5 : Domain wall profile comparison.
a, b, c - Reconstructed unwrapped phase (a), DPC mode (b) and Fresnel mode (c) images of a domain wall in a thin Co film.
d, e, f - Three-dimensional plots of images a-c.
g, h, i - Line profiles across the domain wall, averaged over 100nm.

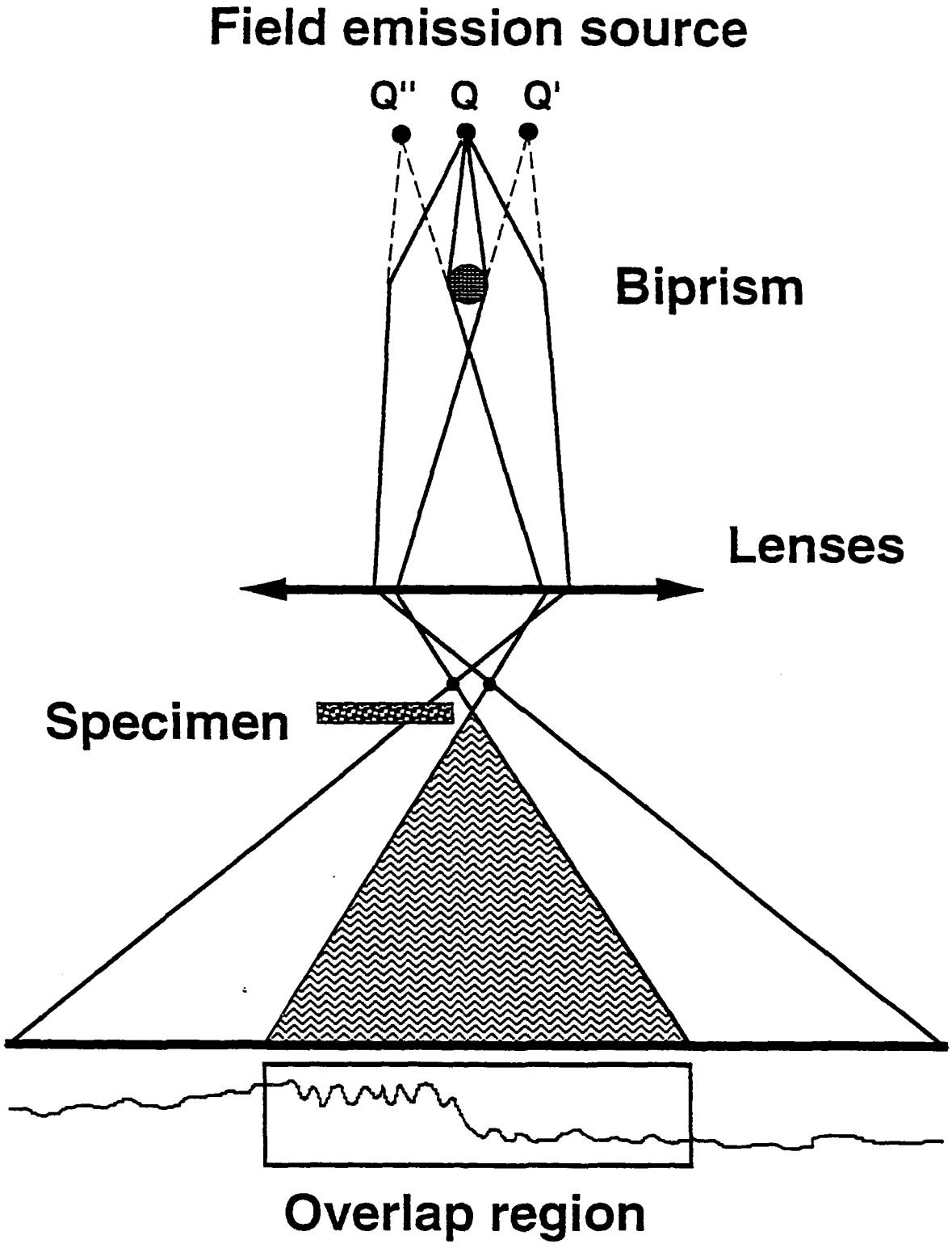
Field emission source
Q''
Q
Q'
Biprism
Lenses
Specimen
Overlap region

Figure 1a

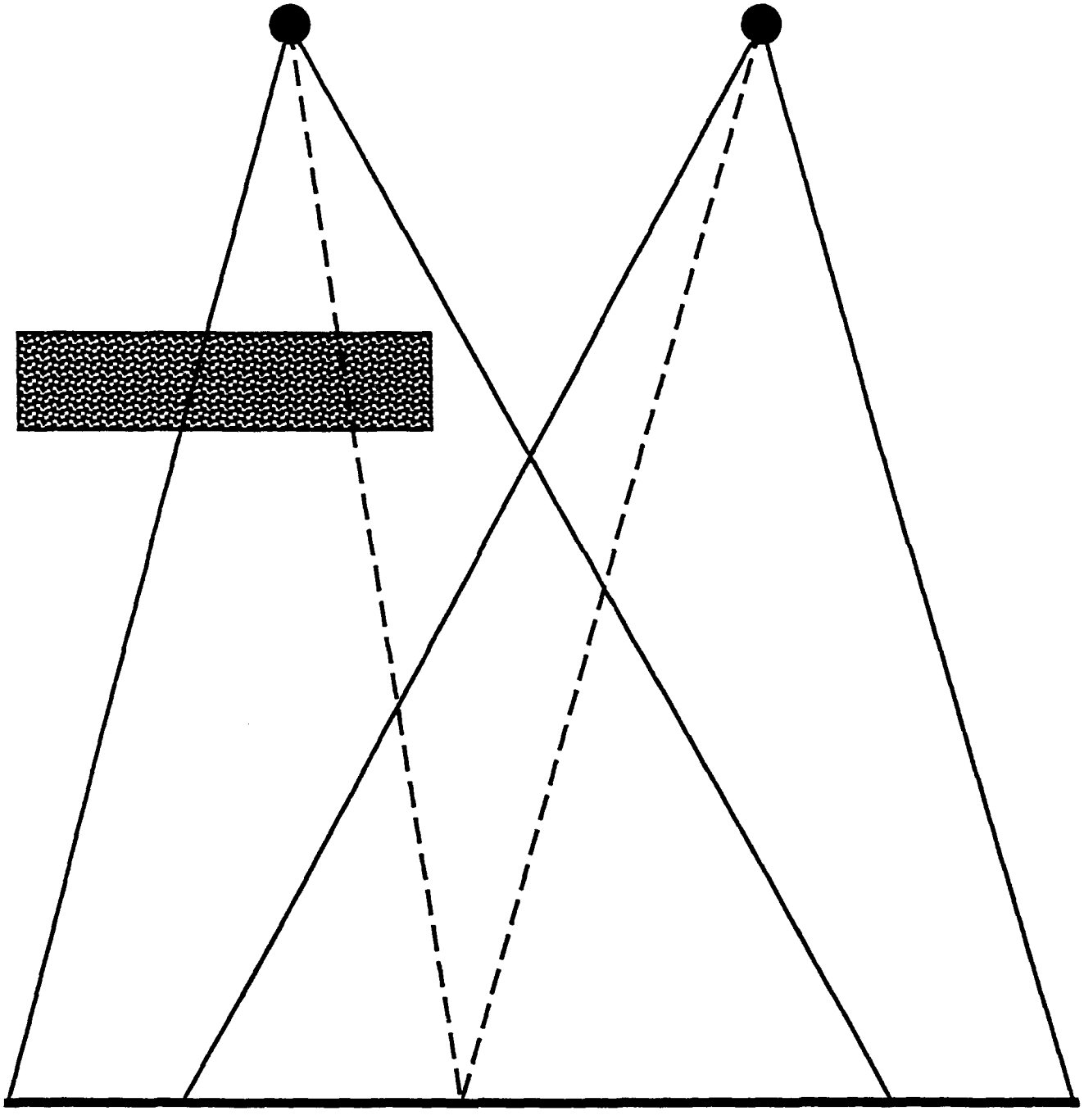

Figure 1b

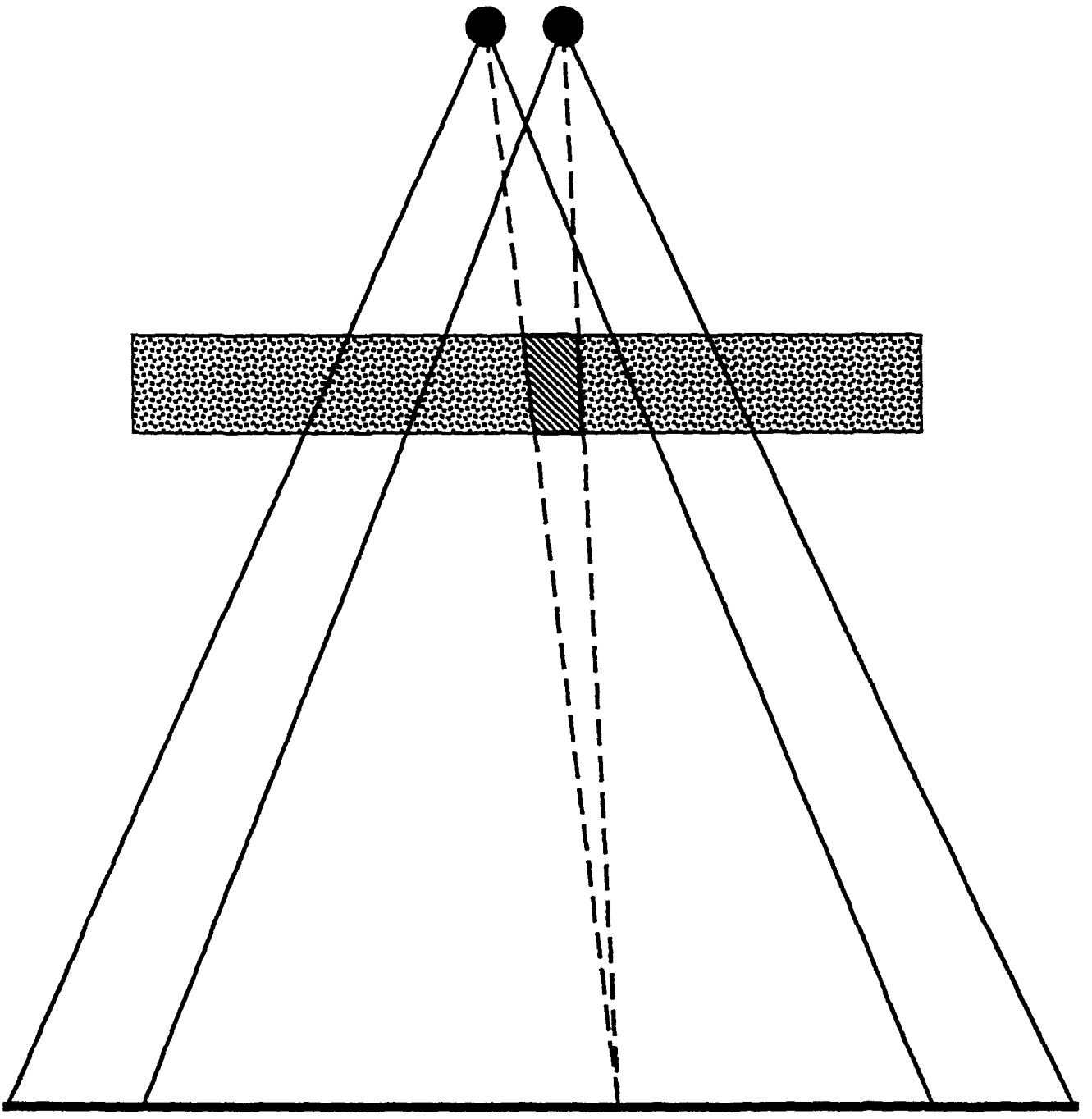

Figure 1c

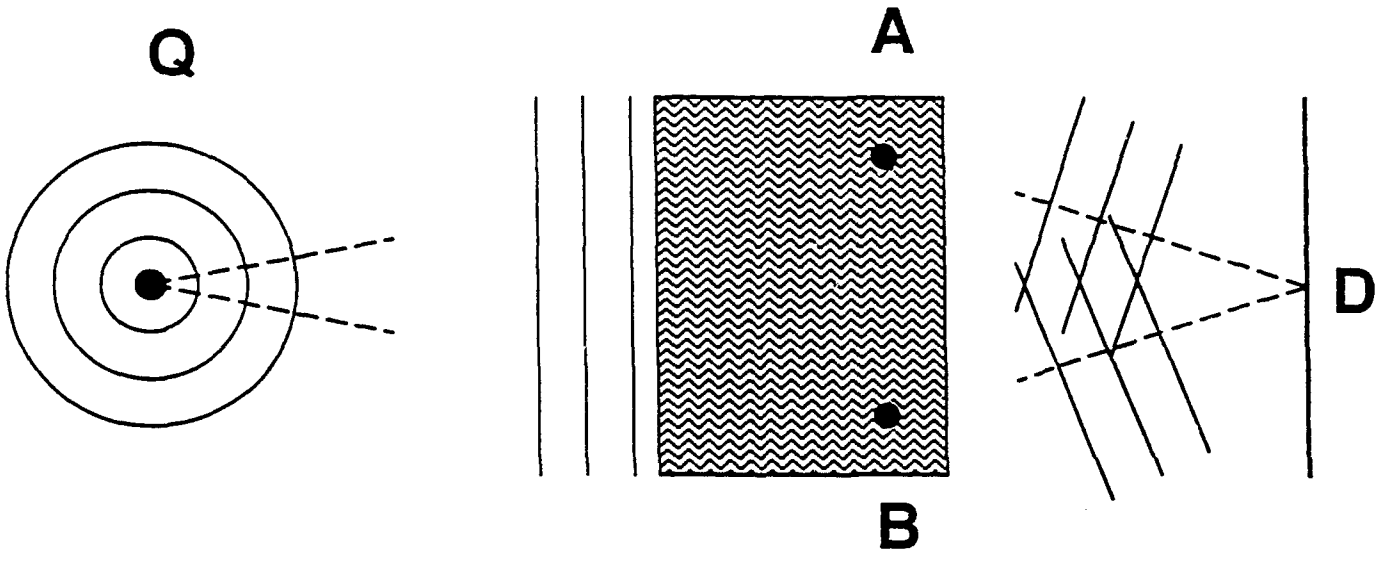

Figure 2

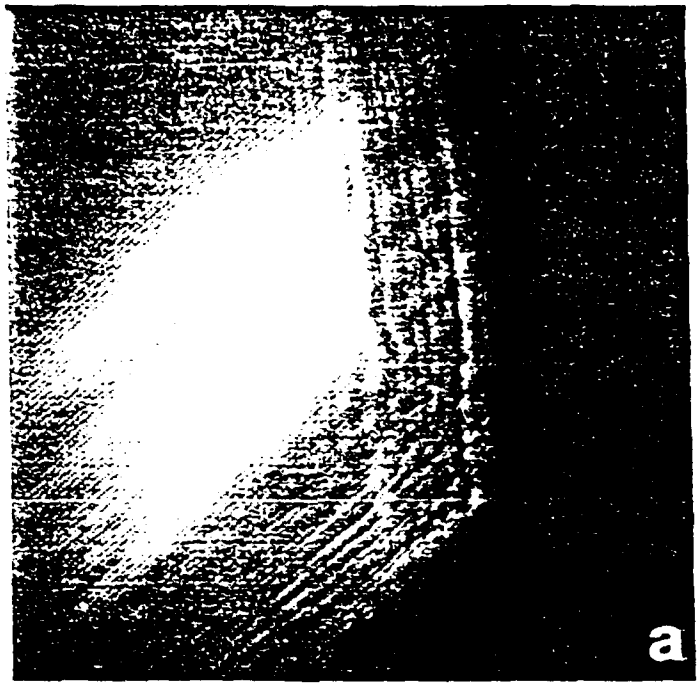

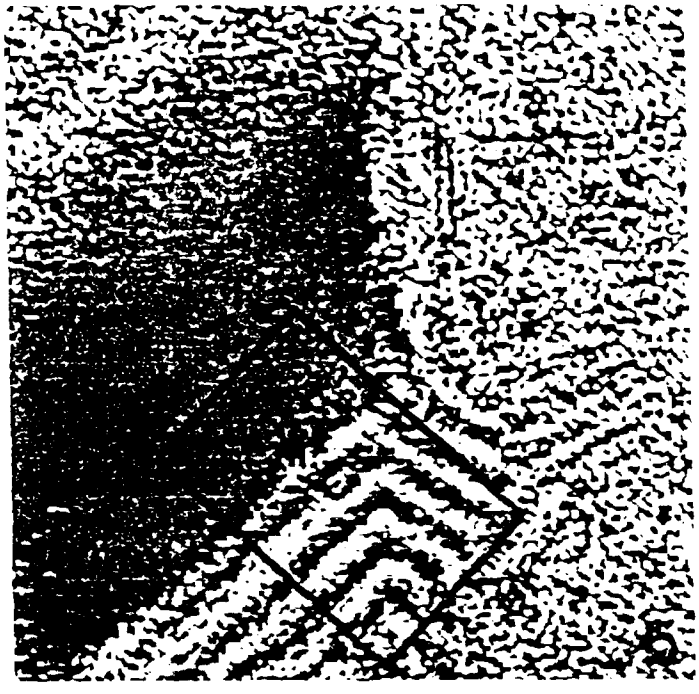

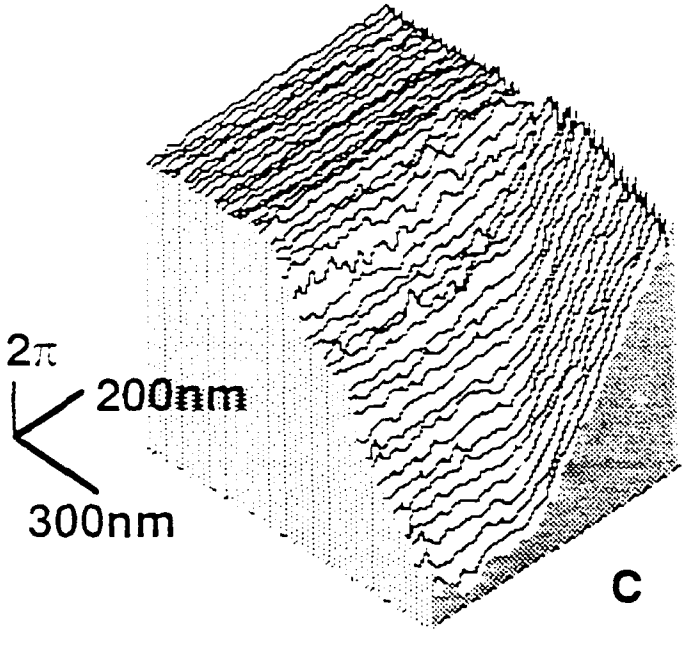

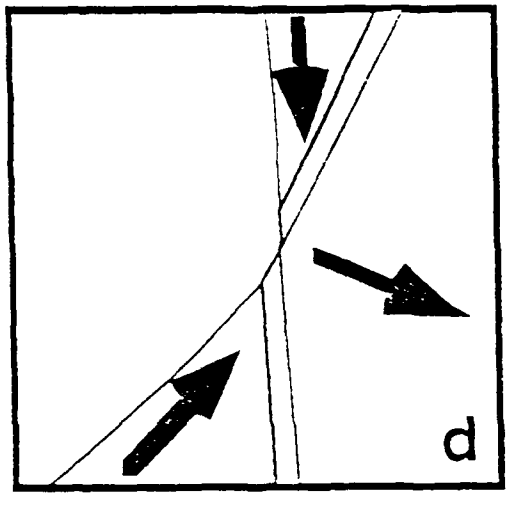

Figure 3

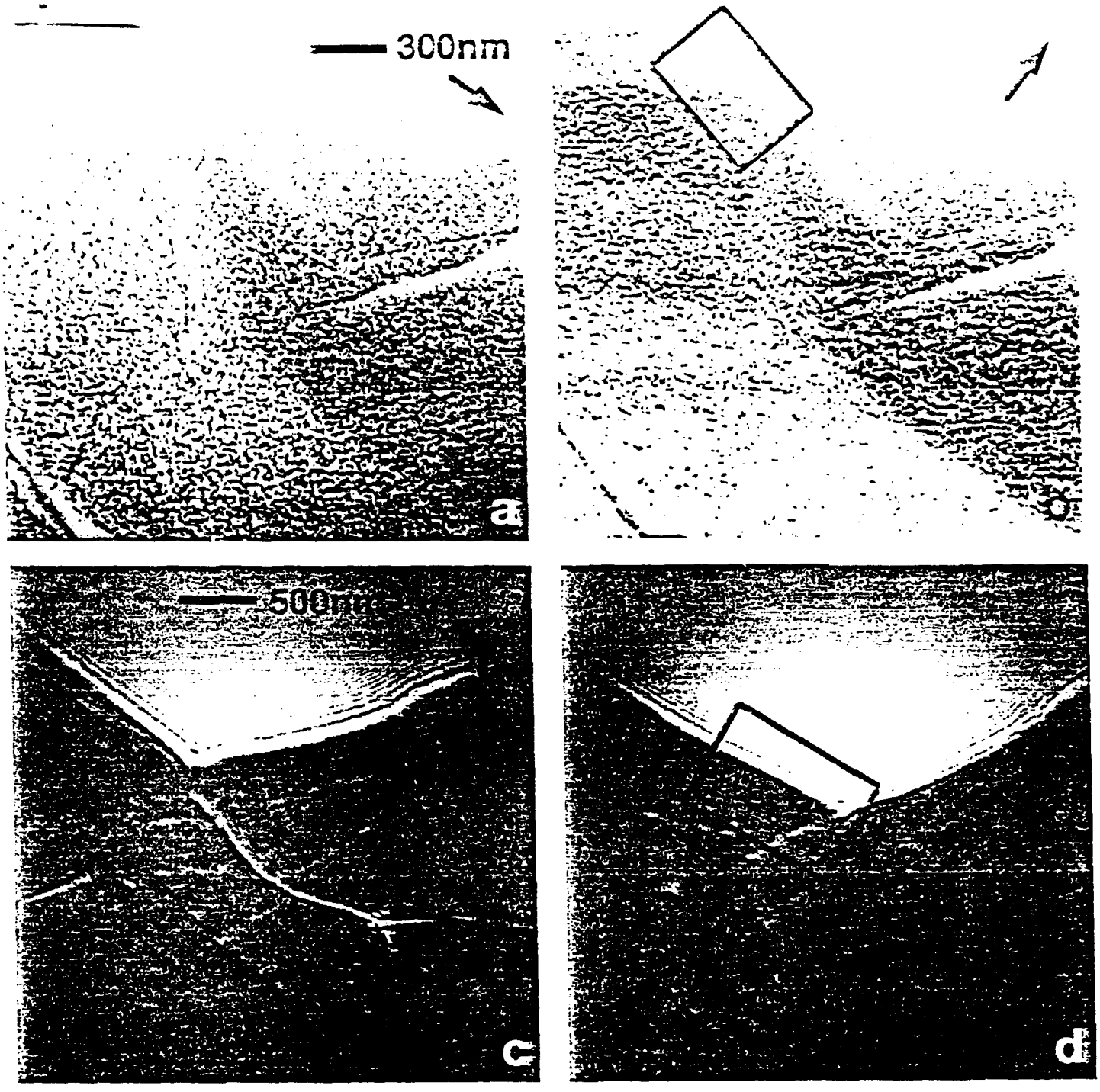

Figure 4

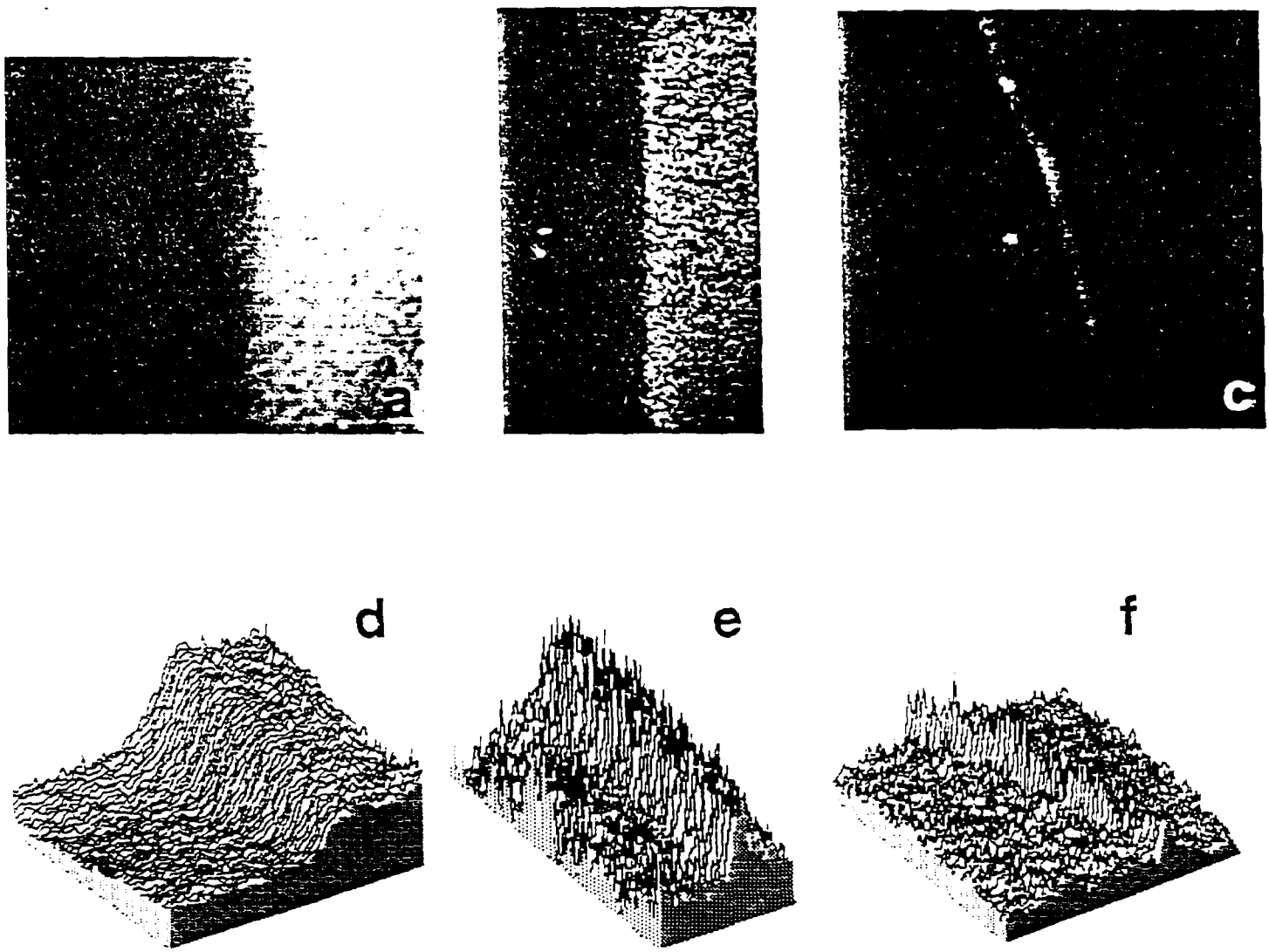
a
c
d
e
f
Phase Difference [rad]
6
4
2
0
-2
-4
0
200
400
600
800
1000
Length [nm]
g
DPC Intensity [rel u]
250
200
150
100
50
0
200
400
600
800
1000
Length [nm]
h
Fresnel Intensity [rel u]
380
370
360
350
340
330
320
0
200
400
600
800
1000
Length [nm]
i

Figure 5

STRUCTURAL AND MAGNETIC PROPERTIES OF EPITAXIALLY GROWN FCC Fe/Cu(100) and Fe/CaF_2/Si(111)

M.R. Scheinfein, S.D. Healy, K.R. Heim, Z.J. Yang, J.S. Drucker*, G.G. Hembree, Department of Physics and Astronomy, *Center for Solid State Science, Arizona State University, Tempe, AZ 85287-1504

ABSTRACT

We have used nanometer spatial resolution secondary electron and Auger electron imaging in an ultra-high vacuum scanning transmission electron microscope to characterize microstructure in ultrathin films of Fe/Cu(100) grown at room temperature and Fe/CaF_2/Si(111) grown at room temperature and 150 C. Thin film microstructure was correlated in situ with magnetic properties by using the surface magneto-optic Kerr effect.

INTRODUCTION

Ferromagnetic ultrathin epitaxial films grown on single crystal metal substrates display unusual properties characteristic of two-dimensional ferromagnetism stabilized by magnetic (surface) anisotropy [1]. The exchange coupling and crystalline anisotropy depend very sensitively on the lattice. Ultrathin films, grown epitaxially on templates which distort the bulk lattice are often highly strained enabling metastable film properties to be explored at room temperature. The most studied, and perhaps the most complex metal/metal epitaxial system is fcc Fe/Cu(100). The fcc phase of Fe, stable in bulk above 911^0 C [2], can be grown epitaxially on Cu(100) with 0.83% lattice mismatch. For fcc (fct) Fe, a non-magnetic, high and low spin, or an antiferromagnetic phase can be stable depending upon the lattice constant [3]. The magnetic properties of fcc Fe/Cu(100) have been investigated using the surface magneto-optical Kerr effect (SMOKE) [4,5], spin-polarized photoemission [6], spin-polarized secondary electron spectroscopy [7,8], conversion-Mössbauer spectroscopy [9], inverse photoemission [10] and spin-polarized scanning electron microscopy (SEMPA) [11]. The energy balance between surface anisotropy and shape anisotropy, both strong functions of film thickness, growth and measurement temperature [4,11-13], determine the easy axis of magnetization. Interest in this system is stimulated by rich structural properties present during various phases of film growth [12-18], including bilayer growth during initial phases of epitaxy [15-18], strain-relief at intermediate thicknesses, weak surface reconstructions [12], and fcc to bcc transitions [e.g. 13]. Extensive work has been devoted to correlating film microstructure with magnetic properties [12,13,19] with emphasis on the non-magnetic-to-magnetic transition at 1-2 ML (ML denotes a monolayer, 0.18 nm for fcc Fe(100)) coverages and the polar-to-longitudinal transition in the easy axis of magnetization at 4-8 ML.

EXPERIMENTAL RESULTS

Our magnetic thin film growth and characterization facility is schematically depicted in Fig. 1. The foundation of this system, shown on the far left-hand side of Fig. 1, is a modified Vacuum Generators HB501-S, field-emission scanning transmission electron microscope (STEM) [24,25]. A magnetic parallelizer (P) [26] guarantees nearly 100% collection efficiency at SE energies, and nearly 50% collection efficiencies at intermediate Auger energies (300 eV to 500 eV) [27]. This high collection efficiency and the ability to form subnanometer 100 keV focused electron probes allows for the acquisition of nanometer transverse spatial resolution secondary and Auger electron images [20-23]. A secondary electron detector (SE) located below the sample facilitates in the study of bulk specimens (S). This electron microscope and the attached preparation chamber enables growth and characterization under UHV conditions using high resolution imaging and standard surface science techniques . A 24 hour, 170°C bakeout of the entire microscope and preparation chamber produces base pressures below 5×10^{-11} mbar. The specimen preparation chamber is equipped with a sample heater (H), a Surface Magneto-Optic Kerr Effect (SMOKE)

Mat. Res. Soc.
(in press)

analysis chamber, a Perkin Elmer model 10-155 cylindrical mirror analyzer (CMA) broad-beam Auger analysis system, a scanning ion sputtering gun (Ar^+), a residual gas analyzer (RGA), various Knudsen cell evaporation sources (K1, K2, and K3), and an electron-bombardment Fe evaporator. The combination of in situ SMOKE measurements with nanometer-resolution microstructural characterization techniques makes this observation system ideal for correlating thin film surface microstructure (those structures with features larger than 1 nm) with macroscopic magnetic properties.

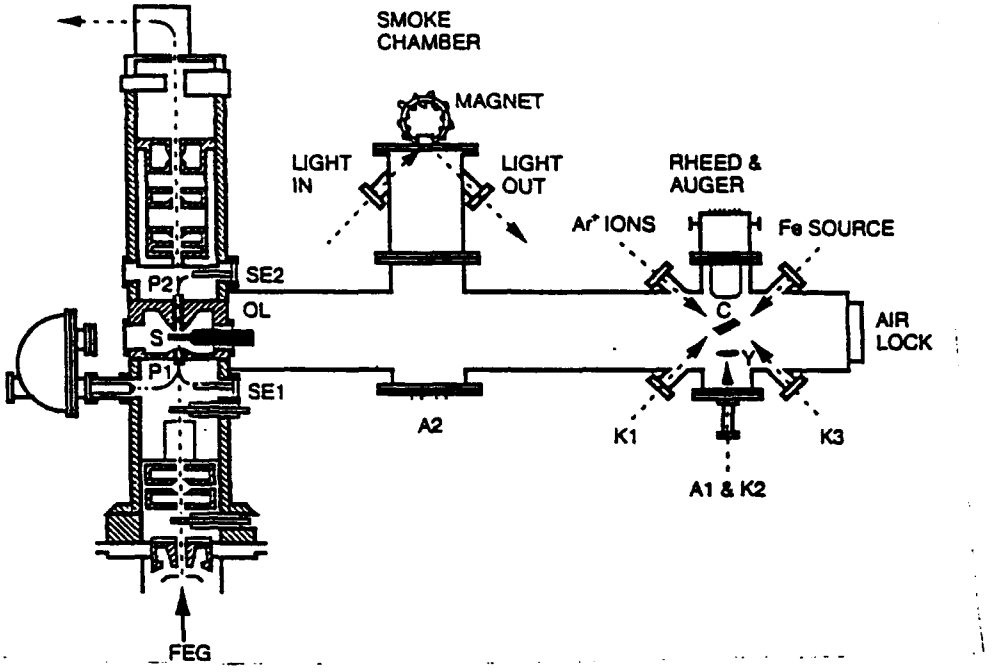

Fig. 1: Modified VG HB501-S thin film growth and characterization facility. The microscope column contains; P2, P1-upper and lower parallelizers, respectively, SE2, SE1-upper and lower secondary electron detectors, respectively, S-sample, OL-objective lens, and a FEG-field emission gun. The specimen preparation chamber consists of a SMOKE chamber for surface magnetism analysis, a CMA-cylindrical mirror analyzer for AES and RHEED, and sample surface preparation tools such as an Ar^+ ion sputtering gun, an Fe evaporator, annealing stages A1 and A2, and Knudsen cell evaporators K1, K2, and K3. Also shown are the Cu crystal, C, the YAG crystal, Y, and the air lock for fast sample entry.

Single crystal Cu(100) substrates were machined into 1 mm thick, 3 mm diameter shouldered disks and commercially electropolished [28]. After attaining pressures below 5×10^{-11} mbar the Cu specimens were sputtered with 600 eV Ar^+ ions at 45° from the surface normal. Typical ion currents were between 200 and 250 nA (current densities of ~10 mA/cm^2) with an operational pressure of 6×10^{-7} mbar. Specifically, the Cu crystals were first sputtered at room temperature for 1 hour. Next, the Cu was heated to ~330°C and hot-sputtered for 4 hours. Following this, the Cu was annealed at ~600°C for 15 minutes to produce a well-ordered surface, as observed with RHEED. Recleaning samples with less than 10 ML (1 ML = 1.805 Å) of Fe on them required a ~330°C sputter period of 1 hour. Any cleaned surface exposed to ambient vacuum conditions for more than several hours or exposed to an electron beam (Auger spectroscopy, RHEED, or electron microscopy) was, prior to Fe deposition, cycled through a ~330°C, 15 minute sputter and a ~600°C, 15 minute anneal. The crystal was allowed to cool for 1.5-2.0 hours after the last anneal such that a temperature below 40°C was obtained prior to Fe deposition.

Following the surface preparation and Fe deposition, surface structural characterization was performed using secondary electron (SE) microscopy. SE microscopy contrast is sensitive to topography [23,29] and local changes in the work function [30]. Several of the cleaned Cu surfaces observed with SE microscopy revealed small contaminant clusters which we believe to be Cu_2O (based upon the most likely copper oxide formed at these temperatures and pressures [31]) islands nucleated over the entire Cu surface. Analysis of these SE images indicates that oxygen coverages ≤0.0011 at.% are well below the sensitivity of the broad-beam AES (typically sensitive to no better than 1 at.%) used in the preparation chamber. In Figs. 2a-f we display corresponding broad-beam Auger spectra and SE images for two identically prepared Cu surfaces. Figs. 2a and 2b are the respective EN(E) and dN(E)/dE spectra acquired for a clean Cu(100) surface. These spectra clearly exhibit five Cu Auger peaks (58, 105, 776, 840, and 920 eV in the derivative mode) while not detecting the O (503 eV) peak (the sensitivity factors at 3 keV indicate that O is about two times more detectable than the 920 eV Cu signal, from which we conclude that the oxygen coverage is ≤2 at.%). The SE image shown in Fig. 2e represents a typical area of the clean Cu(100) crystal surface with less than 1.4×10^9 oxide particles/cm^2, thus yielding an oxygen coverage of 0.016 at.%. The typical terrace width on these Cu(100) surfaces vary from 25 nm to 75 nm, which, based on the uniform growth, is greater than the Fe atom diffusion length for this system. Thus, the effects of a rough and disordered surface on the magnetic properties have been reduced below a detectable level. Insulators and oxides, in general, have higher secondary electron yields than metals [32], and hence appear bright in SE micrographs. In contrast, the Auger spectra in Figs. 2c and 2d also imply a clean Cu surface, but the SE image of Fig. 2f shows larger, more numerous (3.6×10^{10} particles/cm^2 of 10 nm average radius and 3.75 at.%) oxide particles populating the entire Cu surface. In situ electron microscopy, with its high sensitivity for the detection of surface contamination, was used to guarantee the real space chemical and structural integrity of all Cu(100) substrates prior to Fe deposition. In particular, our cleanest Cu(100) surfaces had 1×10^9 particles/cm^2 of 3 nm average radius oxide clusters, implying an oxygen coverage of order ≤0.01 at.%, well below the detectivity of standard surface science techniques.

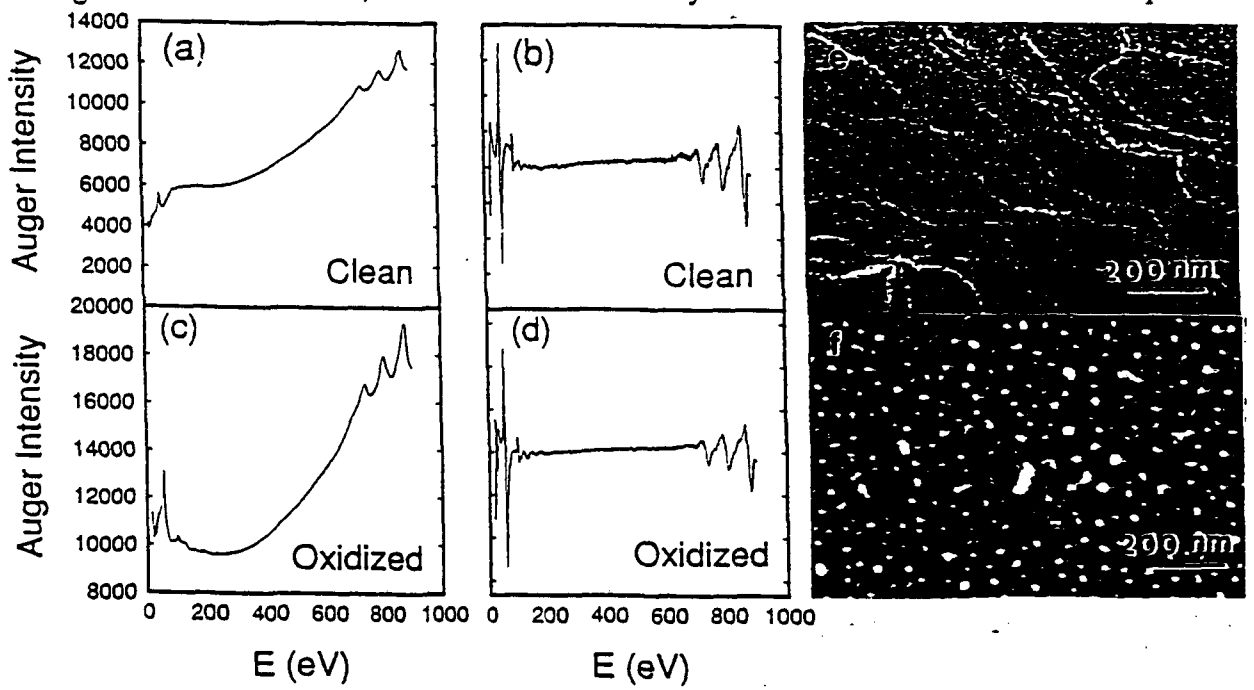

Fig. 2: Auger electron spectroscopy (AES) scans of clean copper in the (a) EN(E) and (b) dN(E)/dE mode with its corresponding (e) secondary electron (SE) image. The white curves are step bands separating terraces. The average terrace width lies within 25 nm and 75 nm. AES scans of oxidized copper in (c) EN(E) and (d) dN(E)/dE mode indicate no contamination while the (f) SE image reveals many oxide.

The thickness dependence of SMOKE hysteresis loops of as-grown fcc Fe/Cu(100) films are shown in Fig. 3. Fe film thicknesses below 2 ML displayed no magnetic response (not shown). Initial magnetic response is observed as a zero-remanence, linear hysteresis loop in the polar direction, with no magnetization in-plane, Figs. 3(a) and 3(b). At intermediate thicknesses, 3.5 ML, remanent polar, Fig. 3(c), and longitudinal, Fig. 3(d), SMOKE loops are observed. While the in-plane loop is square, the tilted polar loop displays the effects of shape anisotropy indicating a canted easy-axis. SMOKE loops from thicker films, 4.7 ML, shown in Figs. 3(e) and 3(f), lose polar remanence, but have square in-plane loops characteristic of an in-plane easy-axis. As-grown in-plane remanence and saturation magnetization both increase nearly linearly with thickness below 5 ML indicating that most of the film (above 2 ML) is magnetically active. Film thicknesses exceeding this range (t -> 10 ML) become non-magnetic, in accordance with prior observations [13]. Films thinner than 10 ML had fcc structure with the transverse lattice constant of the substrate (our RHEED measurements permit an evaluation of the in-plane lattice constant to within ±2%).

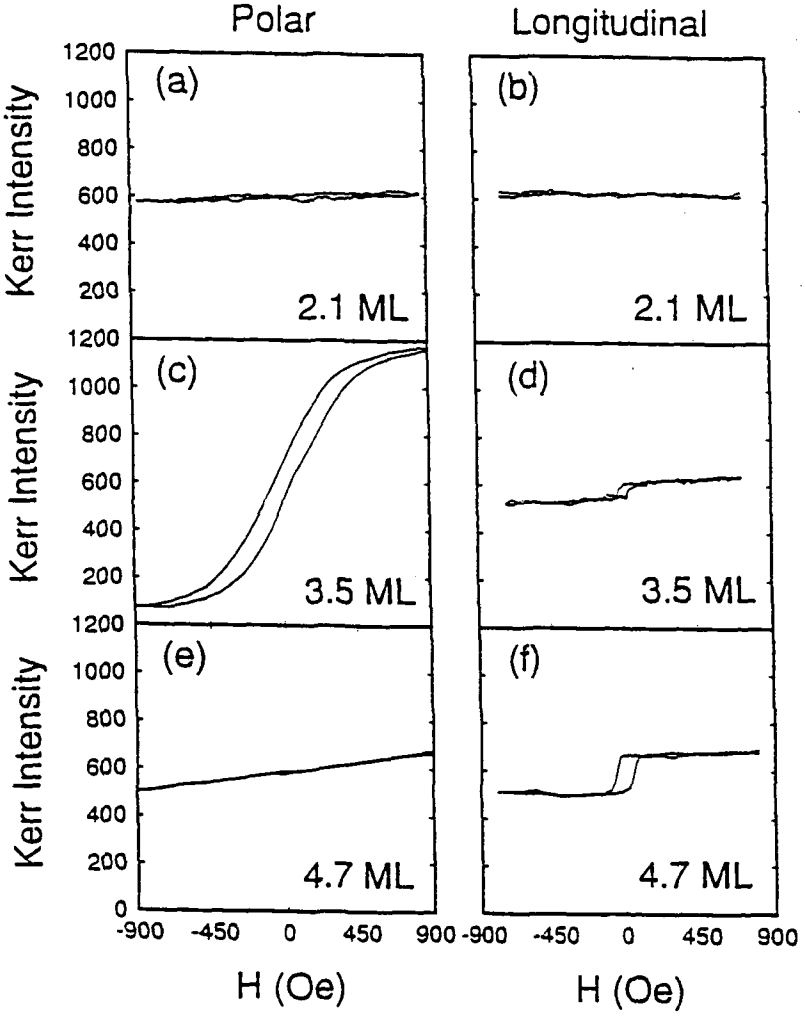

At low film coverages, supersurface island formation can be observed locally by correlating the SE images with the Cu and Fe AE images. One such set of spatially correlated images is displayed in Figure 4 for a 0.33 ML thick Fe film. SE images are sensitive to both the work function and topography of the surface. The SE image in figure 4a illustrates supersurface Fe islands with the corresponding contour plot shown in figure 4b. The large island (~45 nm in diameter) has intensity contours near its upper left quadrant indicating that this island is composed of more than one monolayer of Fe within the bulk of the island. The contrast of the smaller islands is identical to the contrast of the tip of the larger island (within the signal-to-noise limits of these measurements) indicating identical Fe island thicknesses. AE images and contour maps derived from the Cu (Figs. 4c and 4d) and Fe (Figs. 4e and 4f) Auger electron signals can be directly correlated with the SE

Fig. 3: Room temperature grown fcc Fe/Cu(100) polar and longitudinal surface magneto-optical Kerr effect (SMOKE) hysteresis loops. The incident angle is 45° for both longitudinal and polar SMOKE measurements. (a) polar - 2.1 ML, (b) longitudinal - 2.1 ML, (c) polar - 3.5 ML, (d) longitudinal - 3.5 ML, (e) polar - 4.7 ML and (f) longitudinal - 4.7 ML. All measurements made at room temperature.

image of the Fe islands. The AE images are produced by rastering the finely focused 100 keV incident electron beam across the sample surface and collecting most of the Fe (Cu) LMM peak Auger electrons using a spectrometer with a 1.5 eV window which is selected to pass electrons with the respective energy thus generating a two-dimensional surface map . A background map for each Auger map is subsequently acquired by selecting the pass band of the spectrometer to lie 20 eV higher than the Auger peak energy. The images shown in Figs. 4c and 4e result from subtracting the background map from the peak map, such that the intensity within each pixel of the image is proportional to the number of counts within a particular Auger peak, and, therefore, proportional to the number of atoms probed by the incident beam (the sensitivity factors for the Cu and Fe LMM peaks are almost identical). The black areas in Fig. 4c indicate the lack of a Cu signal, while the white areas in Fig. 4e indicate the presence of Fe. It is evident by correlating the contrast in the images and contour maps that the large island and several smaller islands are composed of Fe. Since the signal-to-noise ratio is much better in the SE image, the island density pictured in Fig. 4a likely characterizes the surface.

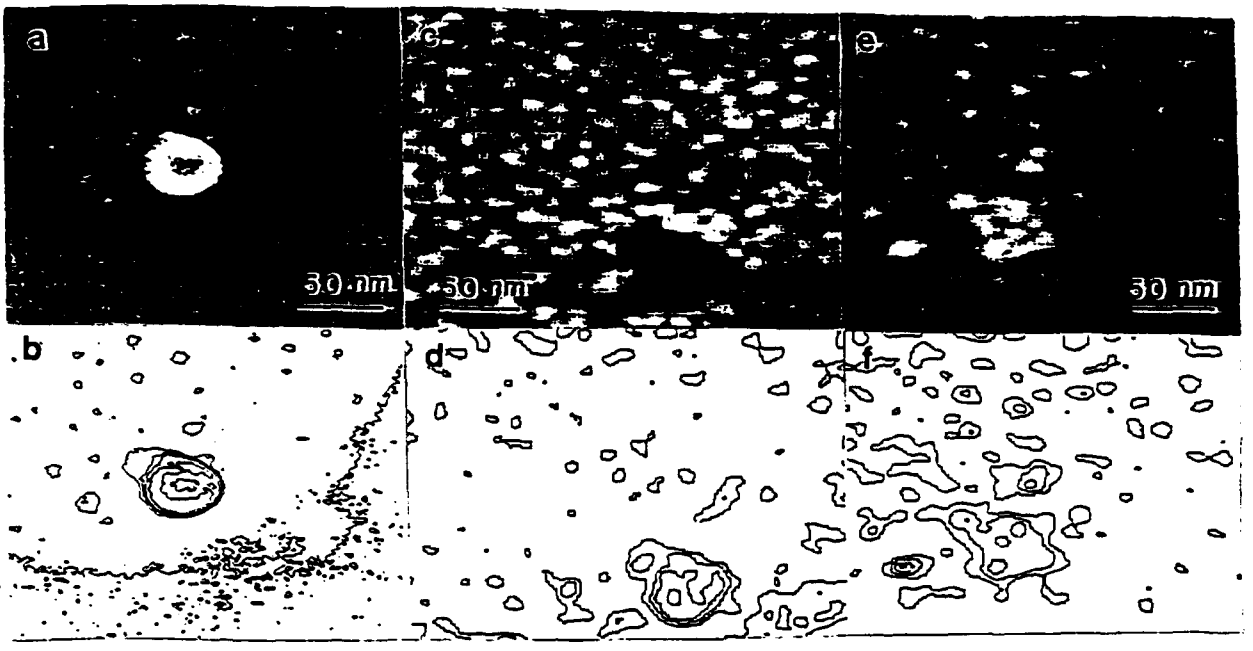

Fig. 4: After deposition of 0.33 ML of Fe at room temperature supersurface islands are observed: (a) secondary electron (SE) image, (b) contour map of SE image indicating island positions, (c) Cu LMM Auger electron (AE) image indicating Cu depletion (black) regions, (d) corresponding contour map of the Cu AE image, (e) Fe LMM AE image indicating Fe (white) islands, and (f) the corresponding contour map of the Fe AE image. The correlation of these three signals indicates that the islands have formed upon the Cu surface. These three images have identical scale factors.

Figure 5a-c displays SE, Cu AE and Fe AE images respectively, all in registry for a Cu substrate with 1.7 ML of Fe deposited at room temperature. The bright regions in the SE image are not correlated with any structure in the Cu (Fig. 5b) or Fe (Fig. 5c) AE images. However, these same Cu and Fe AE images with superimposed contour plots, shown in Figs. 5d and 5e respectively, indicate the regions depleted of Cu are rich in Fe. Since there is no contrast in the SE image, and the SE yield for fcc Fe and Cu are practically identical ($\delta_{Fe}=\delta_{Cu}=0.38$ at 20 keV [33], we conclude that there is no topographic structure on the surface in this region, indicating that the contrast observed in the AE images is a result of two-dimensional subsurface island formation. We have also observed both types of island growth as well as layer-by-layer growth in the same film at different positions along the film. This indicates that these phenomena are controlled by locally varying template surface conditions.

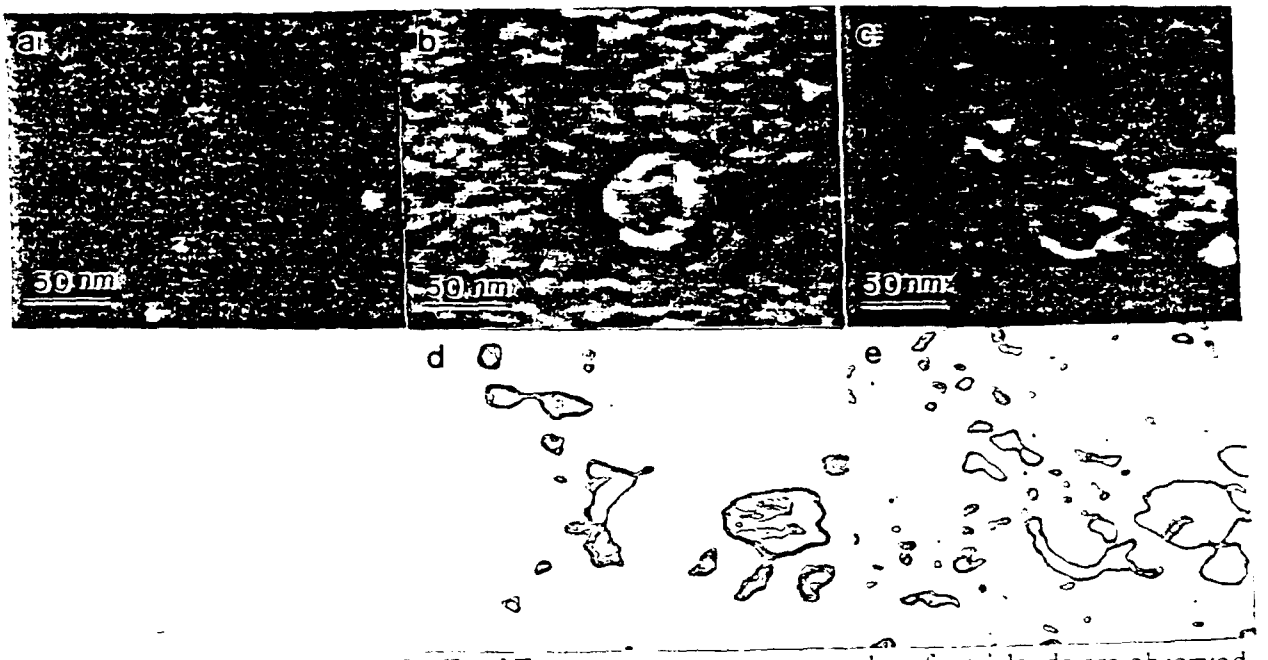

Fig. 5: After deposition of 1.7 ML of Fe at room temperature, subsurface islands are observed. (a) Secondary electron image, (b) Cu LMM Auger electron (AE) image indicating Cu depletion regions (black), and (c) Fe LMM AE image indicating Fe rich regions (white). The correlation of the structure in (b) and (c) and the lack of any contrast in (a) indicates that these islands are within the surface of the substrate. Contour plots for (b) and (c) are shown in (d) and (e) respectively, directly beneath the corresponding image. These three images have identical scale factors.

Our observations suggest that in the regions where subsurface islands occur, a vertical Fe-Cu atomic site exchange occurs. This process continues until the driving force causing the exchange diminishes. We observed this Fe coverage to be thicker than 2 ML, beyond which continuous Fe films grew. The lack of ferromagnetic ordering observed in this sub-2 ML regime is not inconsistent with the observed growth process. In order for the moment of an Fe island to be stable against thermal fluctuations, it must have a minimum size. Assuming a Boltzmann-type probability distribution, it is straight forward to show that most of the Fe islands, which are ~4 nm in diameter, are too small for the moments be unaffected by thermal energy..

We now turn our attension to the growth of Fe on CaF_2. Presently, the majority of solid state devices are fabricated using Si as the semiconducting material due to the existence of its native oxide, SiO_2. The lack of an atomically smooth SiO_2-Si interface does, however, impede the production of three dimensional Si-based devices. Rough interfaces not only decrease the mobility of carriers in devices, but can also destroy the three dimensional epitaxial ordering of subsequent depositions. CaF_2 has been noted as a suitable insulator which may be grown epitaxially and atomically smooth on Si(111) substrates. A small lattice mismatch (0.6% at 298 K) between CaF_2 and Si, a relatively large band gap (12.1 eV) for electronic isolation, and a larger dielectric constant (6.8) than SiO_2 (3.9) for an increased electric field at the insulator-semiconductor device interface are but a few of the many reasons for considering CaF_2 as an obvious replacement for the native SiO_2. In addition, CaF_2 layers may be used as a buffer region such that devices utilizing highly reactive metals such as Fe are not able to form compounds with the Si substrate. The deposition of Fe would enable the fabrication of fully integrated electronic and magnetic devices on a single substrate. Magnetic sensors, high speed microwave waveguides, and non-volatile memories are just three of the many applications which may result from constructing solid state devices using Fe, CaF_2, and Si.

For very slow growth rates the adsorbate topology is expected to approximate structures produced under equilibrium conditions. In this regime, the growth mode is controlled by surface energy imbalances. As Bauer has already set forth [34], a system in equilibrium can be characterized in terms of the surface energy of the adsorbate (γ_a), substrate (γ_s), and the interface between them (γ_i). When $\gamma_a + \gamma_i > \gamma_s$ the deposited material is not expected to spread evenly over the substrate's surface. Fe and CaF_2(111) are known to possess surface energies of 2475 erg/cm^2 [35] and 450-550 erg/cm^2 [36], hence, Fe island formation on CaF_2 is expected. We are interested in the formation of monodisperse transition metal island size distributions because ferromagnetic or paramagnetic granules embedded in a three-dimensional noble metal matrix have been shown to exhibit giant magnetoresistive behavior if the granules are properly spaced and smaller than some critical radius [37]. This leads to the natural extension whereby a two-dimensional array of isolated ferromagnetic particles, such as Fe islands on an insulating CaF_2 substrate, covered by a noble metal is expected to yield two-dimensional giant magnetoresistance (GMR) effects. In addition, since CaF_2 can be chemically altered by electron beam exposure [38], growth modes may be controlled for selected regions of the surface prior to metal deposition by modifying the surface composition with an electron beam. A further increase in electron irradiation and exposure to residual oxygen allows the CaF_2 to be used as an electron beam resist [38], thereby expediting the fabrication of nm-size and low dimensional magnetic devices.

SE microscopy (100 keV and ~10 pA incident beam current), performed before and after (radiatively) annealing the CaF_2/Si(111) substrates at 300 °C for 60 minutes, revealed that areas of obvious surface contamination were not reduced by heating. Broad-beam Auger electron spectroscopy (AES) displayed no statistically significant changes in the chemical composition of the CaF_2 surface after annealing for 60 minutes at temperatures up to 400 °C. Higher annealing temperatures do, however, produce significant changes in the surface morphology. These changes have been observed with SE microscopy. An unannealed CaF_2/Si(111) specimen is shown in Fig. 6a. The saw-toothed step edge visible in Fig. 6a is a typical surface feature of the many samples observed. Fig. 6b indicates that, after a 60 minute, 400 °C anneal, numerous, almost triangularly arranged pits are formed. These morphological changes may have resulted from the relief of stresses present during the growth of the CaF_2 [39]. In order to prevent severe surface modifications (pitting) during cleaning, the substrates were either annealed for 60 minutes at 300 °C or for 24 hours at 170 °C prior to the Fe deposition. Obvious contamination occupied small, localized regions of the total CaF_2 surface area (10-30%), such that Fe island size distributions could be determined from regions between the contaminated areas. Fe was deposited using an electron beam evaporator. The evaporation rate was confirmed by Rutherford backscattering, AES, and quartz-crystal microbalance techniques. The pressure during growth was typically less than 2×10^{-9} mbar with the substrates held at either room temperature or 140 °C.

The initial stage of Fe/CaF_2 growth proceeds by three dimensional islanding. Fig. 6c is an example of a 60 minute Fe deposition at a rate of 0.11 Å/min on a room temperature substrate. The relatively even distribution of 2.0 nm diameter Fe islands on a 100 Å thick CaF_2(111) surface is clearly displayed. Particle size analysis of the SE images revealed no statistical difference between the diameters and spatial distribution of Fe islands grown on 140 °C and room temperature CaF_2/Si(111) substrates. A post-growth anneal of 140 °C on room temperature grown films did not produce a noticeable change in the Fe island size distribution. Statistical analysis performed on a large variety of images yielded the following information for a 60 minute deposition of Fe (0.11 Å/min) on room temperature or 140 °C CaF_2/Si(111) substrates: (1) An average Fe island diameter of 2.0 ± 0.3 nm; (2) A range of Fe island diameters where 85% of the population will lie within 2.0 ± 1.0 nm; (3) An average Fe island separation of 2.0 ± 0.4 nm; (4) A 23% coverage of CaF_2(111) with Fe islands; (5) The number of Fe islands per unit area is 7.4×10^{12} islands/cm^2; (6) The mean distance between Fe island centers is approximately 3.7 ± 0.6 nm; (7) No geometric ordering of the islands was observed based on fast Fourier transform image analysis.

Fig. 6: (a) SE image of an unannealed CaF_2/Si(111) surface. (b) SE image of CaF_2/Si(111) surface that was annealed for 60 minutes at 400 C. Morphological changes are apparent by the many triangularly oriented pits now covering the entire surface. (c) A 60 minute deposition of Fe at a rate of 0.011 nm/min produces a monodisperse island size distribution.

A simple energy calculation indicates that a hemispherically shaped, unstressed, and magnetically ordered Fe particle must contain a single magnetic domain for diameters on the order of a few tens of nanometers. This transition is a result of domain formation becoming energetically unfavorable as the magnetic particle becomes smaller due to the domain boundary energy becoming a large percentage of the total energy. The islands observed in Fig. 6c are smaller than the critical single domain size and separated by less than the mean free path of conduction electrons in metals (near 30 nm at room temperature for Cu [40]). These properties make this system of nm-size Fe islands on an insulator, when covered by a noble metal, an excellent candidate for room temperature GMR studies [41].

CONCLUSIONS

In situ, magnetic and structural characterization of ultrathin films of Fe on Cu(100) was performed using SMOKE, RHEED, broad-beam AES, SE imaging, and AE imaging. Results indicate that room temperature grown films are non-magnetic below 2.1 ML, are ferromagnetic between 2.3 and 5 ML, and are no longer ferromagnetic greater than 5 ML but less than 10 ML. SE and AE images reveal localized alloying and simultaneous multilayered growth for films less than 2 ML and no gross structural changes for films of order 10 ML. AES reconfirms a simultaneous multilayered growth mode due to the lack of breaks in the normalized MVV Cu peak-to-peak height curve as a function of evaporation time. Broad-beam AES was determined to be inadequate for determining the oxide contamination of Cu crystal surfaces because of a lack of detection sensitivity, and may account for the variability in some growth/magnetic properties studies in the fcc Fe/Cu(100) system. Both supersurface islanding and subsurface islanding through vertical atomic site exchange in room temperature grown films of fcc Fe/Cu(100) in the 0-2 ML regime was observed. These observations are not inconsistent with the lack of ferromagnetism observed in room temperature grown sub-2 ML fcc Fe/Cu(100) ultrathin films. A narrow size distribution of 2.0 nm diameter Fe islands was grown on CaF_2/Si(111) surfaces held at or near room temperature. This system, an arrangement of possibly single domain particles separated by less than the mean free path of conduction electrons in metals, is an exciting new candidate for GMR studies.

ACKNOWLEDGEMENTS

The authors wish to acknowledge thoughtful discussions with S. Bader, P. Bennett, M. Hart, D. Loretto, W, Petuskey and J. Venables. We are also indebted to D. Loretto of Lawrence Berkeley Laboratory for supplying the CaF_2/Si(111) samples. This work is supported by the Office of Naval Research under grant No. N00014-93-1-0099 and the National Science Foundation under grant No. DMR 89-14761. The microscopy was performed at the National Science Foundation supported Center for High Resolution Electron Microscopy at Arizona State University, grant No. DMR-91-15680.

REFERENCES

1. N.D. Mermin, H. Wagner, Phys. Rev. Lett. 17, 1133 (1966).
2. L.J. Schwartzendrubber, **Binary Phase Diagrams : vol. 2**, (Publisher, 1990).
3. O.N. Mryasov, A.I. Liechtenstein, L.M. Sandratskii, V.A. Gubanov, J. Phys.: Condens. Matter 3, 7683 (1991); G.L. Krasko, G.B. Olson, Phys. Rev. B40, 11536 (1989); T. Kraft, M. Methfessel, M. van Schilfgaarde, M. Scheffler, Phy. Rev. B47, 9862 (1993); V.L. Moruzzi, P.M. Marcus, K. Schwarz, P. Mohn, Phys. B34, 1784 (1986).
4. C. Liu, E.R. Moog, S.D. Bader, Phys. Rev. Lett. 60, 2422 (1988); C. Liu, E.R. Moog, S.D. Bader, J. Appl. Phys. 64, 5325 (1988); C. Liu, S.D. Bader, J. Vac.Sci. Technol. A8, 2727 (1990); S.D. Bader, Proc. IEEE 78, 909 (1990).
5. W.R. Bennett, W. Schwarzacher, W.F. Egelhoff Jr., Phys. Rev. Lett. 65,3169 (1990).
6. D. Pescia, M. Stampanoni, G.L.Bona, A. Vaterlaus, R.F. Willis, F. Meier, Phys. Rev. Lett. 58, 2126 (1987).
7. D.P. Pappas, K.-P. Kamper, H.Hopster, Phys. Rev. Lett. 64, 3179 (1990).
8. D.P. Pappas, K.-P. Kamper, B.P. Miller, H.Hopster, D.E. Fowler, A.C. Luntz,C.R. Brundle, Z.-X. Shen, J. Appl. Phys. 69, 5209 (1991).
9. W.A.A. Macedo, W. Keune, Phys. Rev. Lett. 61, 475 (1988).
10 F.J. Himpsel, Phys. Rev. Lett. 67, 2363 (1991).
11 R. Allenspach, A. Bishof, Phys. Rev. Lett. 69, 3385 (1992).
12. P. Xhonneux, E. Courtens, Phys. Rev. B46, 5561 (1992).
13. J. Thomassen, F. May, B. Feldmann, M. Wuttig, H. Ibach, Phys. Rev. Lett. 69, 3831 (1992).
14. W.A. Jesser, J.W. Mathews, Phil. Mag. 15, 1097 (1967); Phil. Mag. 17, 461 (1968).
15 S.A. Chambers, T.J. Wagener, J.H. Weaver, Phys. Rev. B36, 8982 (1987).
16 D.A. Steigerwald, W.F. Egelhoff Jr, Surf. Sci. 192, L887 (1987); D.A.Steigerwald, F. Jacob, W.F. Egelhoff Jr., Surf. Sci. 202, 472 (1988).
17. H. Glatzel, Th. Farster, B.M.U. Scherzer, V. Dose, Surf. Sci. 254, 58 (1991).
18. A. Brodde, H. Neddermeyer, Ultramicr. 42-44, 556 (1991).
19 H. Magnan, D. Chandesris, B. Villette, D. Heckmann, J. Lecante, Phys. Rev. Lett. 67, 859 (1991).
20. G. Hembree, J. Drucker, L. Hong, M. Krishnamurthy, and J. A. Venables, Appl. Phys. Lett. **58**, 1991.
21. G. G. Hembree and J. A. Venables, Ultramicroscopy **47**, 109 (1992); J. Liu, G. G. Hembree, G. E. Spinnler, and J. A. Venables, Surface Science Lett. **262**, L111 (1992); J. Liu, G. G. Hembree, G. E. Spinnler, and J. A. Venables, Catalysis Letters **15**, 133 (1992).
22. M. Krishnamurthy, J. Drucker, and J. Venables, J. Appl. Phys. **69**, 6461 (1991).
23. J. Drucker, M. Krishnamurthy, and G. Hembree, Ultramicroscopy **35**, 323 (1991).
24. G. G. Hembree, P. A. Crozier, J. S. Drucker, M. Krishnamurthy, J. A. Venables, and J. M. Cowley, Ultramicroscopy **31**, 111 (1989).
25. J. A. Venables, J. M. Cowley, and H. S. von Harrach, Inst. Phys. Conf. Ser. **90**, 85 (1987).
26. P. Kruit and J. A. Venables, Ultramicroscopy **25**, 183 (1988).
    P. Kruit, Adv. Opt. Electron Microsc. **12**, 93 (1991).
27. M. R. Scheinfein, unpublished.
28. Crystals were custom fabricated by Virgil Straughn, Monocrystals Inc. Cleveland, OH.
20. J. Drucker, J. Appl. Phys. **70**, 2806 (1991).
30. J. A. Venables, D. R. Batchelor, M. Hanbücken, C. J. Harland, and G. W. Jones, Phil. Trans. R. Soc. Lond. A **318**, 243 (1986).
31. F. Grønlund and P. E. H. Nielsen, Surface Science **30**, 388 (1972).
32. G. W. Goetze, A. H. Boerio, an d M. Green, J. Appl. Phys. **35**, 482 (1964); G. W. Goetze, Adv. Electron. Electron Phys. **22**, 219 (1968).
33. L. Reimer, Scanning Electron Microscopy, (Springer-Verlag, Berlin, 1985).
34. E. Bauer, Z. Krist. **110**, 372 (1958).
35. F. R. de Boer, R. Boom, W. C. M. Mattens, A. R. Miedema, and A. K. Niessen, *Cohesion in Metals Transition Metal Alloys* (North-Holland Elsevier Science Publishers,NY, 1988).

36. J. J. Gilman, J. Appl. Phys. **31**, 2208 (1960). G. C. Benson and T. A. Claxton, Can. J.Phys. **41**, 1287 (1963). P. W. Tasker, J. Phys. (Paris) **41**, C6-488 (1980).
37. J. Q. Xiao, J. S. Jiang, and C. L. Chien, Phys. Rev. Lett. **68**, 3749 (1992).
38. T. R. Harrison, P. M. Mankiewich, and A. H. Dayem, Appl. Phys. Lett. **41**, 1102 (1982). P. M. Mankiewich, H. G. Craighead, T. R. Harrison, and A. H. Dayem, Appl. Phys. Lett. **44**, 468 (1984). M. Scheinfein and M. Isaacson, J. Vac. Sci. Technol. **B 4**, 326 (1986).
39. Private communication with D. Loretto: Bright field transmission electron microscopy performed on the CaF_2/Si(111) samples revealed a non uniform distribution of line defects at the CaF_2-Si(111) interface. This is an indication that stress relief occurred during the CaF_2 growth. In comparison, an unrelaxed film will display a parallel array of line defects corresponding to the original steps on the Si(111) surface.
40. C. Kittel, *Introduction to Solid State Physics, fourth edition* (John Wiley & Sons, 1971),page 259.
41. C. L. Chien, J. Appl. Phys. **69**, 5267 (1991). A. E. Berkowitz, J. R. Mitchell, M. J. Carey, A. P. Young, S. Zhang, F. E. Spada, F. T. Parker, A. Hutten, and G. Thomas, Phys. Rev. Lett. **68**, 3745 (1992). A. E. Berkowitz, J. R. Mitchell, M. J. Carey, A. P. Young, D. Rao, A. Starr, S. Zhang, F. E. Spada, F. T. Parker, A. Hutten, and G. Thomas, J. Appl. Phys. **73**, 5320 (1993).